DOE-ER-0313/46
Distribution
Categories
UC-423, -424

FUSION MATERIALS
SEMIANNUAL PROGRESS REPORT
FOR THE PERIOD ENDING

June 30, 2009

Prepared for
DOE Office of Fusion Energy Sciences
(AT 60 20 10 0)

DATE PUBLISHED: September 2009

Prepared by
OAK RIDGE NATIONAL LABORATORY
Oak Ridge, Tennessee 37831
Managed by
UT-Battelle, LLC
For the
U.S. DEPARTMENT OF ENERGY

FOREWORD

This is the forty-sixth in a series of semiannual technical progress reports on fusion materials science activity supported by the Fusion Energy Sciences Program of the U.S. Department of Energy. It covers the period ending June 30, 2009. This report focuses on research addressing the effects on materials properties and performance of exposure to the neutronic, thermal and chemical environments anticipated in the chambers of fusion experiments and energy systems. This research is a major element of the national effort to establish the materials knowledge base for an economically and environmentally attractive fusion energy source. Research activities on issues related to the interaction of materials with plasmas are reported separately.

The results reported are the product of a national effort involving a number of national laboratories and universities. A large fraction of this work, particularly in relation to fission reactor irradiations, is carried out collaboratively with partners in Japan, Russia, and the European Union. The purpose of this series of reports is to provide a working technical record for the use of program participants, and to provide a means of communicating the efforts of fusion materials scientists to the broader fusion community, both nationally and worldwide.

This report has been compiled under the guidance of F. W. (Bill) Wiffen and Renetta Godfrey, Oak Ridge National Laboratory. Their efforts, and the efforts of the many persons who made technical contributions, are gratefully acknowledged.

Barry Sullivan
Research Division
Office of Fusion Energy Sciences

TABLE OF CONTENTS

Nano-dispersion strengthened ferrite alloys (NFA) show great promise for structural applications in severe fusion reactor environments. NFA contain an ultra high density of Y-Ti-O enriched nanofeatures (NF) that, along with fine grains and high dislocation densities, provide high tensile, creep and fatigue strength. The NF are remarkably thermally stable and trap He in fine scale bubbles, thereby suppressing fast fracture embrittlement at lower temperatures, void swelling at intermediate temperatures and degradation of creep rupture properties at high temperatures. However, the precise characteristics of various NF are not yet well understood. They appear to range from coherent solute enriched GP-type zones to near stoichiometric complex oxides, such as Y_2TiO_5 and $Y_2Ti_2O_7$. Here we summarize a recent effort to clarify the characteristics of NF for a reference NFA, MA957, based on the application of several complementary micro-analytical characterization techniques. High-resolution transmission electron microscopy (HRTEM)-Fast Fourier Transform (FFT) power spectra diffraction patterns indicate that the larger features (> 10 nm) are primarily Y_2TiO_5. Limited diffraction data show the smaller features (≈5 nm) are not consistent with known oxide phases. Energy dispersive x-ray (EDX) measurements yield average feature compositions of Y/Ti/O ≈ 27/20/53 for both larger and smaller features. In contrast, atom probe tomography data show average solute compositions of Y/Ti/O = 14/41/45 and Y/Ti/O = 20/32/48 for the smaller and larger features, respectively. The APT data also suggest that even the larger particles contain significant quantities of Fe, and to a lesser extent Cr, which are not observed in the EDX measurements.

4. COPPER ALLOYS

No contributions this period

5. REFRACTORY METALS AND ALLOYS

No contributions this period

6. AUSTENITIC STAINLESS STEELS

No contributions this period

7. FUNCTIONAL MATERIALS – INCLUDING MHD INSULATORS, COATINGS, INSULATING CERAMICS, AND OPTICAL MATERIALS

7.1 COMPATIBILITY OF MATERIALS EXPOSED TO ISOTHERMAL Pb-Li – 28

B. A. Pint (Oak Ridge National Laboratory, USA)

Two sets of capsules experiments exposed for 1000h at 500°-700°C were completed to determine the effect of various factors on the amount of dissolution in Pb-Li. The first set examined the effects of Al-rich coatings and the characterization has been completed. Thin coatings exposed at 700°C showed significant Al loss with different variations: (1) pre-oxidation, (2) O gettering and (3) exposure in pure Pb without Li. Less Al loss was observed after exposure at 600°C. A second series of capsules were recently completed that explored the effect of Fe and Ni impurities on the dissolution rate and dissimilar metal reactions between Fe and SiC at 600°C. Based on only the mass gain data, there is some indication of a dissimilar metal effect in Pb-Li.

8. BREEDING MATERIALS

No contributions this period

9. RADIATION EFFECTS, MECHANISTIC STUDIES, AND EXPERIMENTAL METHODS

9.1 MODELLING THERMODYNAMICS OF ALLOYS FOR FUSION APPLICATION - 35

A. Caro, P. Erhart, M. Serrano de Caro, B. Sadigh (Lawrence Livermore National Laboratory), S.G. Srinivasan (UNT), A. Stukowski (Germany)

This semester has been very productive in the developments of both tools and algorithms.

- With the visit of a A. Stukowsky, a graduate student from Prof. K. Albe (Germany) we implemented the formalism of the composition dependent embedded atom model (CD-EAM) into Lammps, a freely distributed code for molecular dynamics. We also implemented a 'variance constrained' Metropolis Monte Carlo, MMC, algorithm into Lammps.
- We developed a modified version of the CD-EAM, that we call 'one site' CD-EAM that significantly improves the performance of a MMC algorithm without affecting the accuracy of the interatomic potential.
- We developed a ternary FeCr-He potential based on data obtained from Prof. K. Nordlund's group in Finland. We validate this potential against *ab initio* data on He in FeCr obtained from within a collaboration with Chu Chun Fu at CEA-Saclay, France.
- We started simulation of He bubbles in FeCr alloys, determining the pressure versus size relation for the 1He/vacancy ratio

9.2 MODELING OF POINT DEFECT CLUSTER EVOLUTION UNDER PULSED IRRADIATION - S.I. Golubov (Oak Ridge National Laboratory, University of Tennessee), R.E. Stoller (Oak Ridge National Laboratory), A.V. Barashev (The University of Liverpool) **40**

The main results of this work are summarized as follows:

- For the first time point defect (PD) cluster nucleation and growth during different pulsed irradiation regimes has been calculated and compared with that of steady irradiation.
- It is found that PD cluster nucleation is extremely sensitive to the type of irradiation: it is enhanced in the case of pulsed irradiation. The effect increases with decrease of pulse frequency.
- Rate of damage accumulation under pulsed irradiation is larger at small doses and smaller at high doses than that for steady irradiation.
- The calculation results obtained suggest that the pulse structure of MTS and IFMIF may reproduce damage accumulation quite close to that one may expect for steady irradiation whereas it may be very different in the case of SNS irradiation.
- The new method for numerical integration of the Master Equation used provides a valuable tool to link experimental data obtained using different types of irradiations.

9.3 ATOMISTIC STUDIES OF PROPERTIES OF HELIUM IN BCC IRON USING THE NEW HE–FE POTENTIAL—David M. Stewart, Stanislav Golubov (Oak Ridge National Laboratory and the University of Tennessee), Yuri Ostesky, Roger E. Stoller, Tatiana Seletskaia, and Paul Kamenski (Oak Ridge National Laboratory) **52**

In fusion applications, helium caused by transmutation plays an important role in the response of RAFM steels to neutron radiation damage. We have performed atomistic simulations using a new 3-body Fe–He inter-atomic potential combined with the Ackland iron potential. With the ORNL potential, interstitial helium is very mobile and coalesces together to form interstitial clusters. We have investigated the mobility of these clusters. If the He cluster is sufficiently large the cluster can push out an Fe interstitial, creating a Frenkel pair. The resulting helium-vacancy cluster is not mobile. The ejected SIA is mobile, but is weakly trapped by the He–V cluster. If more helium atoms join the He–V cluster, more Fe interstitials can be pushed out, and they combine to form an interstitial dislocation loop. The reverse process is also studied. Multiple helium atoms can be trapped in a single vacancy, and if there are few enough, the vacancy can recombine with an Fe interstitial to create a helium interstitial cluster. These mechanisms are investigated together in larger simulations that examine the nucleation of He defects. Results are compared based on temperature, interatomic potentials used and helium concentration. Helium bubbles of sizes 1-6nm are also studied.

12. IRRADIATION FACILITIES AND TEST MATRICES

ADDITIONAL CHARACTERIZATION OF V-4Cr-4Ti EXPOSED TO FLOWING Li – B. A. Pint (Oak Ridge National Laboratory)

OBJECTIVE

Characterize specimens exposed to flowing Li in a thermal gradient to evaluate the effects on V-4Cr-4Ti and a multi-layer electrically-insulating coating needed to reduce the magneto hydrodynamic (MHD) force in the first wall of a lithium cooled blanket.

SUMMARY

In order to clarify prior results, more Li-exposed V-4Cr-4Ti specimens were evaluated at 500°C in vacuum with a strain rate of $10^{-3}s^{-1}$. These specimens confirmed prior results that exposure in the loop increased strength and slightly decreased ductility. However, while the increase in strength decreased with exposure temperature, the ductility effect was minor and more variable. The specimens exposed at lower temperatures in the loop showed the highest tensile strength, lowest ductility and least dynamic strain aging. More microstructural characterization is needed to complete this study.

PROGRESS AND STATUS

Introduction

The previous report[1] covered 500°C tensile behavior of V-4Cr-4Ti after various exposures including flowing Li in a thermal convection loop with a peak temperature of 700°C for 2,355h.[2] Because of the unusual results from the loop exposed specimens, five additional loop-exposed V-4Cr-4Ti specimens were evaluated at 500°C under the same conditions to provide additional data for evaluation.

Experimental Procedure

Details of the thermal convection loop exposure have been presented previously.[2] The specimens consisted of miniature tensile specimens (type SS-3: 25 x 4 x 0.9mm), tab specimens and specimens with a dual layer MHD coating in a chain held together with V-4Cr-4Ti wire. The tensile specimens were annealed for 1h at 1050°C prior to exposure in Li. The exposure temperature for each specimen is estimated by using a linear extrapolation of the temperatures measured at the top and bottom of the each leg.[2] Tensile testing was conducted at 500°C in a vacuum with a base pressure of 10^{-6}Pa (10^{-8}Torr) and a strain rate of $10^{-3}s^{-1}$. No microstructural characterization of these V-4Cr-4Ti tensile specimens has been conducted at this time.

Results and Discussion

Table I summarizes the results from all of the tensile experiments conducted at 500°C[1] and the mass change that occurred during loop exposure for each of the specimens. The five additional tests are marked with an asterisk. Only the loop specimen near the top of the hot leg showed a mass loss. The other mass gains were attributed to uptake of C and N being greater than the loss of O to the flowing Li. Figure 1 shows the 500°C tensile properties as a function of calculated exposure temperature in the hot and cold legs of the loop. In general, all of the specimens showed an increase in ultimate tensile stress (UTS) compared to the unexposed specimens and some decrease in ductility, Table I. The increase in UTS decreased with exposure temperature while the decrease in ductility generally decreased with temperature but the effect was more scattered. As each specimen is not large enough to perform a chemical analysis, tab and tube specimens were used to measure chemistry changes. The analyses

Table 1. Summary of 500°C tensile data for V-4Cr-4Ti specimens with $10^{-3}s^{-1}$ strain rate.

Location	Mass Gain (mg/cm^2)	Yield Stress (MPa)	Ultimate Stress (MPa)	Uniform Elong. (%)	Total Elong. (%)
As-annealed	N/A	218	384	25.3	25.6
As-annealed	N/A	194	379	23.8	24.9
Top Hot Leg, 627°C	-0.13	185	388	21.0	23.2
*Mid. Hot Leg, 595°C	0.04	211	403	23.3	24.9
*Mid. Hot Leg, 501°C	0.08	293	436	19.0	20.6
Bottom Hot Leg, 459°C	0.02	306	465	18.6	20.6
Top Cold Leg, 562°C	0.06	234	392	22.5	23.5
*Mid. Cold Leg, 539°C	0.07	261	401	20.3	22.1
*Mid. Cold Leg, 516°C	0.06	273	405	20.9	21.8
*Mid. Cold Leg, 470°C	0.07	290	433	21.8	23.1
Bottom Cold Leg, 447°C	0.10	287	441	20.1	21.6
800°C Li capsule	-0.04	178	351	25.3	27.3
800°C Li capsule	-0.01	181	358	26.5	28.2
700°C anneal	0.01	220	371	21.9	23.6

*experiments during this period

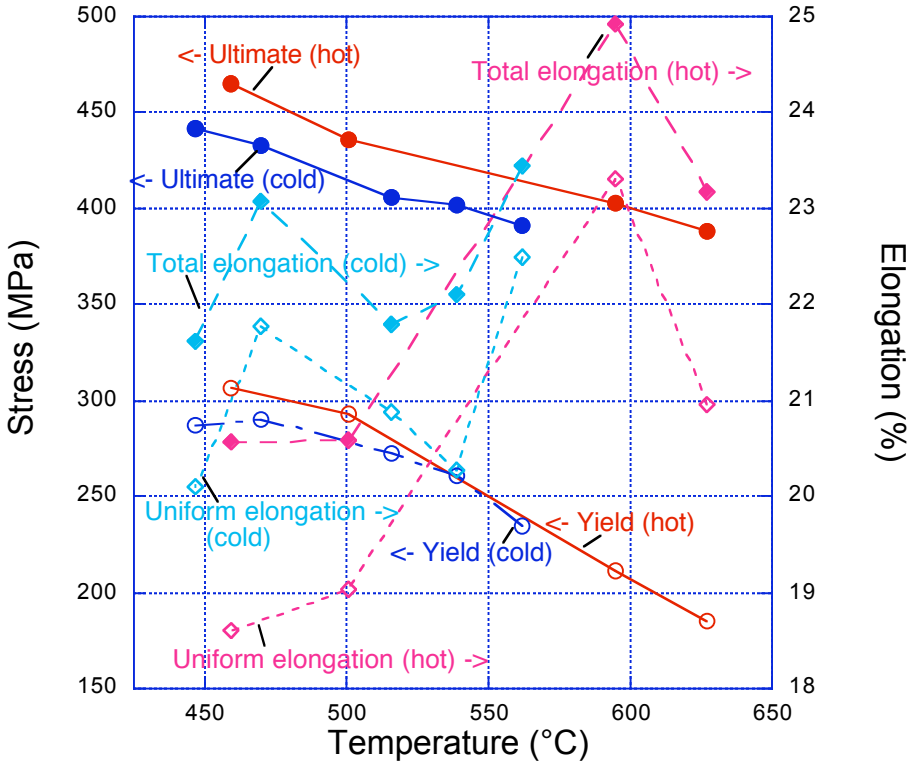

Figure 1. Tensile properties measured at 500°C for the loop-exposed specimens as a function of the calculated average exposure temperature for each specimen.

consistently showed a decrease in the O content and an increase in the C and N contents.[1-4] These changes in interstitial content are expected based on Li thermodynamics of gettering O, but low affinity, compared to vanadium, for C and N. Characterization work is needed to determine how the decrease in O and increase in C and N affected the precipitate composition and distribution.

Prior work with Li exposures at 700° and 800°C conducted in an Ar-filled glove box, nominally allowing some degree of Li contamination during the exposure, showed a much larger decrease in ductility measured at 500°C with exposures as long as 1000h.[5] As a further comparison with this work, Figure 2 shows the effect of loop location on the serrations in the stress-strain curve due to dynamic strain aging (DSA).[6,7] The conventional explanation for DSA is the interaction of dislocations with solute interstitials. Interpreting these results is complicated by the competing reduction in O with the increase in C and N observed in the loop. A complete characterization of the microstructure of these specimens is needed to understand the mechanism.

References

[1] B. A. Pint, DOE/ER-0313/45 (2008) 11.
[2] B. A. Pint, et al., J. Nucl. Mater. 386-388 (2009) 712.
[3] B. A. Pint, et al., DOE/ER-0313/43 (2007) 2.
[4] B. A. Pint, DOE/ER-0313/44 (2008) 10.
[5] M. M. Li, D. T. Hoelzer and M. L. Grossbeck, J. Nucl. Mater. 392 (2009) 364.
[6] T. Nagasaka, T. Muroga, M. M. Li, D. T. Hoelzer, S. J. Zinkle, M. L. Grossbeck and H. Matsui, Fus. Eng. Des., 81 (2006) 307.
[7] A. F. Rowcliffe, S. J. Zinkle and D. T. Hoelzer, J. Nucl. Mater. 283-287 (2000) 508.

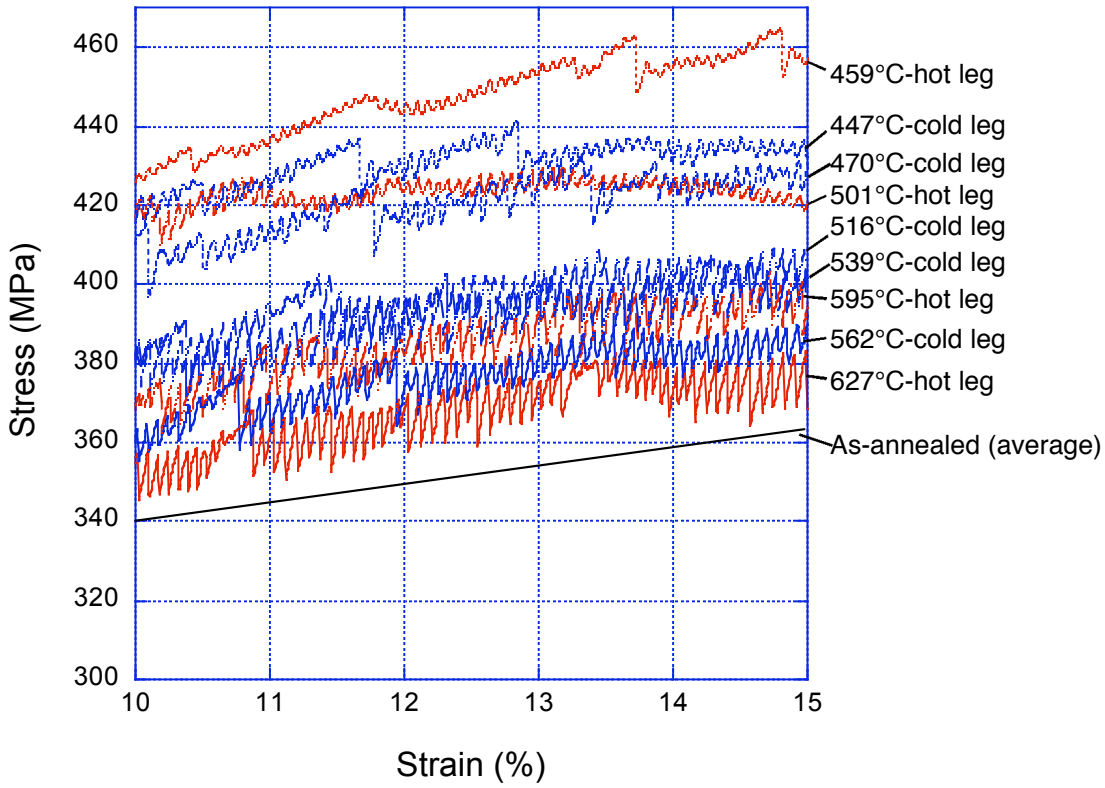

Figure 2. Expanded stress-strain curves of V-4Cr-4Ti specimens evaluated at 500°C in vacuum with a strain rate of $10^{-3}s^{-1}$ to show the dynamic strain aging behavior.

THE EFFECTS OF NEUTRON IRRADIATION ON DIMENSIONAL CHANGE IN ADVANCED SILICON CARBIDE COMPOSITES—K. Ozawa, Y. Katoh, L.L. Snead (Oak Ridge National Laboratory), T. Nozawa (Japan Atomic Energy Agency), T. Hinoki (Kyoto University), and A. Hasegawa (Tohoku University)

OBJECTIVE

The objective of this work is investigation of the neutron irradiation effects on the dimensional change of silicon carbide composites reinforced with advanced silicon carbide fibers.

SUMMARY

The dimensional change and elastic modulus of advanced silicon carbide (SiC) fibers reinforced silicon carbide matrix (SiC/SiC) composites included in the HFIR-18J irradiation experiment were measured and the data collected in the past five years were summarized. The excellent dimensional stability of the advanced SiC/SiC composites was confirmed after neutron irradiation to 7.0×10^{25} n/m^2. The stability is superior to composites reinforced with the earlier generation SiC fibers. The swelling of the advanced composites was measured to be ~0.7% for a dose of ~7.0×10^{25} n/m^2 at 800°C (nominal). This corresponds to the swelling behavior of chemically vapor deposited (CVD) SiC.

PROGRESS AND STATUS

Introduction

Silicon carbide (SiC) -based ceramics and composites are considered for applications in various components in fusion systems, due primarily to their superior irradiation performance and thermo-physical, -chemical, and -mechanical properties [1, 2]. Swelling behavior during irradiation is one of the important issues to be considered. Recently, swelling behavior and microstructural development in monolithic SiC, the main constituent of SiC/SiC composites, have been thoroughly studied after systematic ion and neutron irradiation to high dose and very high temperature [3-8]. In contrast, data on the swelling behavior of advanced SiC/SiC composites are quite limited [9]. There is some data available on one of the composites, but it was reinforced with older generation fibers [10-12]. The main objective of this study is to investigate the neutron irradiation effects on dimensional changes in advanced SiC/SiC composites.

Experimental Procedure

Two types of materials were used in this study. One is monolithic SiC, used to generate statistical data in a flexural strength evaluation with specimen dimensions 1×1×24 or 1×1×25 mm. The specimens are made by chemically vapor deposition (CVD) or nano-infiltration and transient eutectic-phase (NITE) process. The other is SiC/SiC composites reinforced with advanced SiC fibers for flexural or tensile property evaluation with specimen dimensions 2×4×25, 2×4×50, 3×1.5×40 or 2×4×40 mm. The composites were processed by chemically vapor infiltration (CVI) or NITE method and reinforced with Tyranno-SA 3rd or Hi-Nicalon Type-S fibers. Neutron irradiation was conducted at Japan Material Testing Reactor (JMTR), JOYO and High Flux Isotope Reactor (HFIR). The specimens were irradiated to 1.0× 10^{25} n/m^2 (~1 dpa, E > 0.1 MeV; hereafter 1.0×10^{25} n/m^2 =1 dpa is assumed) at ~1000°C (nominal) for JMTR campaign, to 12 dpa at ~750°C (nominal) for JOYO CMIR-6 campaign, and to 7 dpa at 800 and 1300°C (nominal) for HFIR-18J. Information on materials characterization and neutron irradiation conditions is listed in Tables 1-3, along with the property change results. Further details about material characterization, irradiation condition, and mechanical properties before and after irradiation are given elsewhere for JMTR 00M-95U [13-15], and the HFIR-18J [16] campaign. After neutron irradiation, the length of the specimens was measured by a conventional caliper. Volumetric swelling was determined using the following equation $\Delta V/V = (L_{irrad.}/L_{unirrad.})^3$-1, where $\Delta V/V$, $L_{irrad.}$, and $L_{unirrad.}$ are volumetric swelling, length of the specimen before irradiation, and length after irradiation, respectively. This equation was chosen in order to avoid low accuracy in measuring width and thickness, and hence it assumes that the swelling of the advanced SiC/SiC composites is isotropic. In parallel, dynamic elastic modulus was

determined at room temperature using the impulse excitation of vibration method per ASTM Standard C1259-01.

Results and Discussion

Monolithic SiC

The results of dimensional change and elastic modulus for monolithic CVD and NITE-SiC are listed in Table 1. Figure 1 shows the dependence of volumetric swelling on irradiation temperature. The swelling results for CVD-SiC are consistent with the values reported in the literature, as shown in Fig. 1. The swelling of monolithic NITE-SiC is almost the same or slightly higher than CVD-SiC. Elastic modulus of both CVD- and NITE-SiC was decreased slightly by neutron irradiation to 7dpa at 800 and 1300°C.

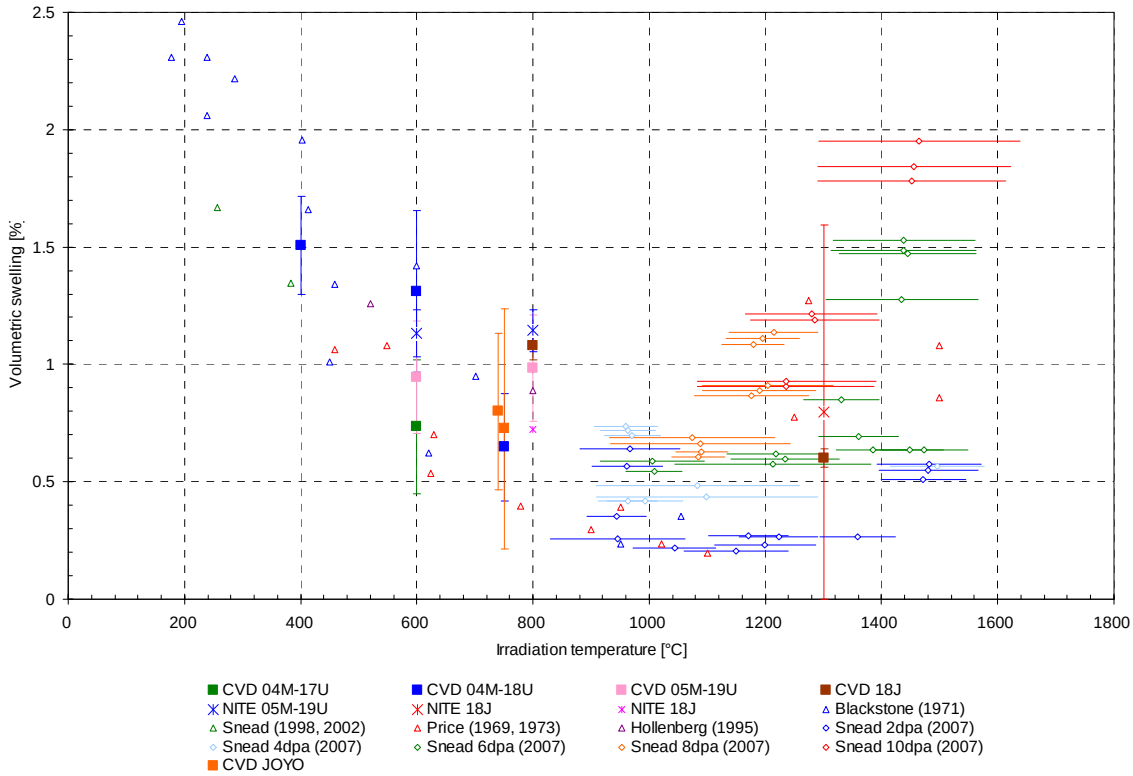

Fig. 1: Temperature dependence of volumetric swelling of monolithic CVD and NITE SiC. The data are from the reports by Blackstone et al. [17], Snead et al. [11, 18], Price [19, 20], Hollenberg et al. [10], Snead et al. [3, 4] , and Katoh et al. [21].

SiC/SiC Composites

Individual results for advanced SiC/SiC composites are listed in Table 1. Average results for each condition are also listed in Table 2. Figures 1, 2 show the volumetric swelling of advanced SiC/SiC composites dependence on dose and irradiation temperature. This confirms the excellent dimensional stability of the advanced SiC/SiC composites during neutron irradiation, compared to the composites reinforced with older generation SiC fibers. For CVI-SiC/SiC composites, 0.2-0.5% swelling after neutron irradiation 1 dpa at 1000°C for JMTR 00M-95U, and ~0.7% swelling after 7 dpa at 800 and 1300°C for HFIR-18J were measured, as shown in Fig. 1. There was no significant difference in swelling detected arising from the difference of fibers used or interphase structure. The swelling of the advanced SiC/SiC

composites irradiated to 7dpa at 800°C (~0.7%) is almost the same as reported by Newsome et al. [9]. The advanced SiC/SiC composites showed similar swelling values as β-SiC after irradiation, as shown in Figs. 2 and 3. This is primarily because both fibers and matrix of advanced SiC/SiC composites are composed of highly crystalline β-SiC. In the intermediate temperature regime, β-SiC swells due to point defect clustering, and the swelling is saturated at a few dpa. This saturation swelling in SiC is significant at irradiation temperatures below ~1000ºC with the volume expansion negatively correlated with temperature (~1.4% at 300ºC, ~0.7% at 800ºC, ~0.3% at 1000°C), as shown in Fig. 1.

A slight decrease (~4%) of elastic modulus was measured in the composites reinforced with Tyranno-SA 3rd fiber, while ~13% decrease was obtained in the Hi-Nicalon Type-S composites.

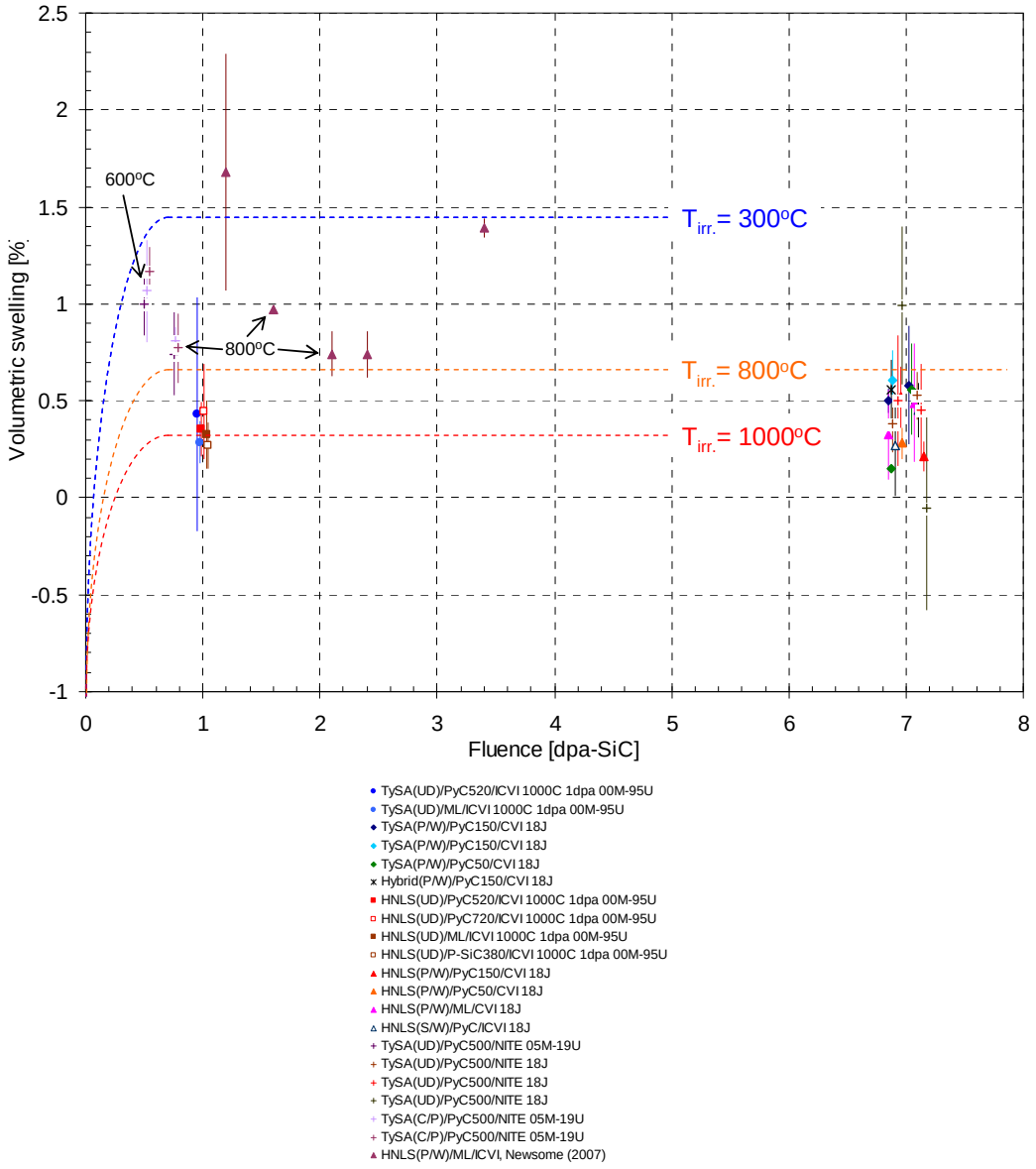

Fig. 2: Dose dependence of swelling of neutron irradiated advanced SiC/SiC composites. The data have been shifted slightly on the Fluence axis for clarity. For comparison, the values in ref. [9] were also plotted.

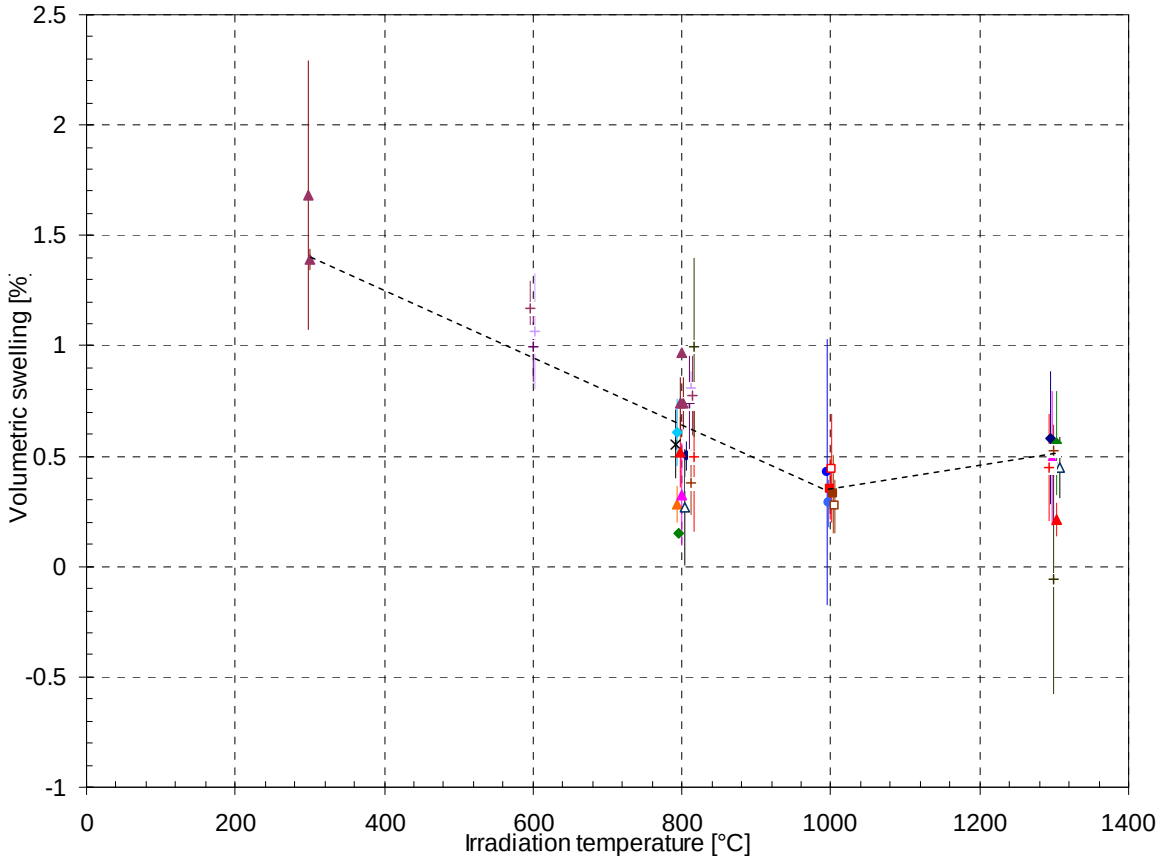

Fig. 3: Temperature dependence of swelling of advanced SiC/SiC composites. The data have been shifted slightly on the Irradiation temperature axis for clarity. For comparison, the values in ref. [9] were also plotted. The legend symbols are the same as used in Fig. 1.

Table 1: Average values of volumetric swelling and dynamic modulus (E) of monolithic SiC after neutron irradiation.

Reactor	Capsule ID	Specimen ID	Irradiation Temperature [°C]	Fluence [dpa]	Material	# of Tests	Length Before Irrad. [mm]	Length After Irrad. [mm]	Length Change [%]	Vol. Swelling [%]	Std. dev. [%]	Sonic E Before Irrad. [GPa]	Sonic E After Irrad. [GPa]	% Change In E
JMTR	04M-17U	-	600	0.52	CVD	20	23.98	24.04	0.24	0.73	0.29	-	-	-
JMTR	04M-18U	-	400	0.77	CVD	20	23.98	24.10	0.50	1.51	0.21	-	-	-
JMTR	04M-18U	-	600	0.52	CVD	20	23.98	24.09	0.44	1.31	0.35	-	-	-
JMTR	04M-18U	-	750	0.77	CVD	20	23.98	24.04	0.22	0.65	0.23	-	-	-
JMTR	05M-19U	-	600	0.52	CVD	20	23.99	24.06	0.31	0.95	0.24	-	-	-
JMTR	05M-19U	-	800	0.77	CVD	20	23.99	24.06	0.33	0.99	0.23	-	-	-
JMTR	05M-19U	-	600	0.52	NITE	20	24.98	25.08	0.38	1.13	0.10	-	-	-
JMTR	05M-19U	-	800	0.77	NITE	20	24.99	25.08	0.38	1.14	0.09	-	-	-
JOYO	CMIR-6 JNC-54	-	750	12	CVD	18	22.02	22.08	0.24	0.73	0.51			
JOYO	CMIR-6 JNC-61	-	740	3.1	CVD	19	22.02	22.08	0.27	0.80	0.33			
HFIR	18J	R001-R030	800	7	CVD	5	24.86	24.95	0.36	1.08	0.06	-	-	-
HFIR	18J	R061-R090	1300	7	CVD	28	24.86	24.91	0.20	0.60	0.04	-	-	-
HFIR	18J	L061-L090	1300	7	NITE	21	24.98	25.05	0.26	0.80	0.80	-	-	-
HFIR	18J	R1	800	7	CVD	1	25.40	25.42	0.09	0.28	-	448.31	433.73	-3.25
HFIR	18J	R7	800	7	CVD	1	25.41	25.43	0.08	0.24	-	450.06	436.38	-3.04
HFIR	18J	R5	1300	7	CVD	1	-	-	-	-	-	449.35	441.36	-1.78
HFIR	18J	R6	1300	7	CVD	1	-	-	-	-	-	446.20	436.88	-2.09
HFIR	18J	L1	800	7	NITE	1	24.93	24.99	0.24	0.72	-	352.81	336.70	-4.57
HFIR	18J	L3	1300	7	NITE	1	-	-	-	-	-	337.69	319.56	-5.37

Table 2: Length change, volumetric swelling and dynamic modulus of individual advanced SiC/SiC specimens before and after neutron irradiation. Temperatures shown are nominal values. E; elastic modulus, Hybrid; combination of Tyranno-SA 3rd SiC fiber and P-120 carbon fiber ,UD; uni-directional, P/W; plain-woven, S/W; satin-woven, 3D; 3D orthogonal, PyC; pyrolytic carbon, ML; multi-layered, P-SiC; porous SiC, ICVI; isothermal chemically vapor infiltration.

Reactor	Capsule ID	Temp. [°C]	Fluence [x10^25 n/m^2]	Specimen ID	Fiber	Archi-tecture	Inter-phase	Thick-ness [nm]	Matrix	Length Before Irrad. [mm]	Length After Irrad. [mm]	Length Change [%]	Vol. Swelling [%]	Sonic E Before Irrad. [GPa]	Sonic E After Irrad. [GPa]	% Change In E
JMTR	00M-95U	1000	1	TP23-1	Tyranno-SA 1st	UD	PyC	520	ICVI	24.85	24.98	0.54	1.62	-	-	-
JMTR	00M-95U	1000	1	TP23-2	Tyranno-SA 1st	UD	PyC	520	ICVI	24.99	25.00	0.04	0.12	-	-	-
JMTR	00M-95U	1000	1	TM24-1	Tyranno-SA 1st	UD	ML		ICVI	25.22	25.24	0.09	0.28	-	-	-
JMTR	00M-95U	1000	1	TM24-2	Tyranno-SA 1st	UD	ML		ICVI	24.59	24.61	0.07	0.20	-	-	-
JMTR	00M-95U	1000	1	ST41-2	Hi-Nicalon Type-S	UD	PyC	720	ICVI	25.01	25.04	0.13	0.40	-	-	-
JMTR	00M-95U	1000	1	SM25-2	Hi-Nicalon Type-S	UD	ML		ICVI	25.01	25.02	0.03	0.08	-	-	-
JMTR	00M-95U	1000	1	SS26-1	Hi-Nicalon Type-S	UD	P-SiC	380	ICVI	24.64	24.66	0.08	0.24	-	-	-
JMTR	00M-95U	1000	1	SS26-2	Hi-Nicalon Type-S	UD	P-SiC	380	ICVI	25.10	25.12	0.09	0.28	-	-	-
JMTR	00M-95U	1000	1	TP17	Tyranno-SA 1st	UD	PyC	520	ICVI	50.06	50.08	0.05	0.14	-	-	-
JMTR	00M-95U	1000	1	TP18	Tyranno-SA 1st	UD	PyC	520	ICVI	50.07	50.15	0.16	0.48	-	-	-
JMTR	00M-95U	1000	1	TP19	Tyranno-SA 1st	UD	PyC	520	ICVI	50.08	50.11	0.07	0.20	-	-	-
JMTR	00M-95U	1000	1	TP20	Tyranno-SA 1st	UD	PyC	520	ICVI	50.10	50.10	0.01	0.02	-	-	-
JMTR	00M-95U	1000	1	TM17	Tyranno-SA 1st	UD	ML		ICVI	50.07	50.11	0.07	0.22	-	-	-
JMTR	00M-95U	1000	1	TM18	Tyranno-SA 1st	UD	ML		ICVI	50.07	50.10	0.06	0.18	-	-	-
JMTR	00M-95U	1000	1	TM19	Tyranno-SA 1st	UD	ML		ICVI	50.08	50.15	0.14	0.42	-	-	-
JMTR	00M-95U	1000	1	TM22	Tyranno-SA 1st	UD	ML		ICVI	50.08	50.15	0.14	0.42	-	-	-
JMTR	00M-95U	1000	1	SP20	Hi-Nicalon Type-S	UD	PyC	520	ICVI	50.05	50.13	0.15	0.45	-	-	-
JMTR	00M-95U	1000	1	SP21	Hi-Nicalon Type-S	UD	PyC	520	ICVI	50.07	50.15	0.16	0.48	-	-	-
JMTR	00M-95U	1000	1	SP23	Hi-Nicalon Type-S	UD	PyC	520	ICVI	50.05	50.10	0.10	0.30	-	-	-
JMTR	00M-95U	1000	1	SP25	Hi-Nicalon Type-S	UD	PyC	520	ICVI	50.11	50.14	0.06	0.18	-	-	-
JMTR	00M-95U	1000	1	ST36	Hi-Nicalon Type-S	UD	PyC	720	ICVI	50.09	50.18	0.19	0.56	-	-	-
JMTR	00M-95U	1000	1	ST37	Hi-Nicalon Type-S	UD	PyC	720	ICVI	50.10	50.12	0.04	0.12	-	-	-
JMTR	00M-95U	1000	1	ST38	Hi-Nicalon Type-S	UD	PyC	720	ICVI	50.09	50.15	0.12	0.36	-	-	-
JMTR	00M-95U	1000	1	ST39	Hi-Nicalon Type-S	UD	PyC	720	ICVI	50.07	50.20	0.26	0.78	-	-	-
JMTR	00M-95U	1000	1	SM21	Hi-Nicalon Type-S	UD	ML		ICVI	50.07	50.14	0.14	0.42	-	-	-
JMTR	00M-95U	1000	1	SM22	Hi-Nicalon Type-S	UD	ML		ICVI	50.07	50.11	0.07	0.22	-	-	-
JMTR	00M-95U	1000	1	SM23	Hi-Nicalon Type-S	UD	ML		ICVI	50.05	50.12	0.13	0.40	-	-	-

Table 2: (Cont'd)

Reactor	Capsule ID	Temp. [°C]	Fluence [x10^25 n/m^2]	Specimen ID	Fiber	Archi-tecture	Inter-phase	Thick-ness [nm]	Matrix	Length Before Irrad. [mm]	Length After Irrad. [mm]	Length Change [%]	Vol. Swelling [%]	Sonic E Before Irrad. [GPa]	Sonic E After Irrad. [GPa]	% Change In E
JMTR	00M-95U	1000	1	SM24	Hi-Nicalon Type-S	UD	ML		ICVI	50.02	50.11	0.17	0.52	-	-	-
JMTR	00M-95U	1000	1	SS22	Hi-Nicalon Type-S	UD	P-SiC	380	ICVI	50.07	50.10	0.06	0.18	-	-	-
JMTR	00M-95U	1000	1	SS23	Hi-Nicalon Type-S	UD	P-SiC	380	ICVI	50.04	50.10	0.12	0.36	-	-	-
JMTR	00M-95U	1000	1	SS24	Hi-Nicalon Type-S	UD	P-SiC	380	ICVI	50.10	50.18	0.15	0.45	-	-	-
JMTR	00M-95U	1000	1	SS25	Hi-Nicalon Type-S	UD	P-SiC	380	ICVI	50.08	50.10	0.04	0.12	-	-	-
HFIR	18J	800	7	T01	Tyranno-SA 3rd	P/W	PyC	150	CVI	39.98	40.04	0.16	0.48	251.01	242.16	-3.53
HFIR	18J	800	7	T02	Tyranno-SA 3rd	P/W	PyC	150	CVI	39.98	40.06	0.20	0.60	273.94	264.40	-3.48
HFIR	18J	800	7	T03	Tyranno-SA 3rd	P/W	PyC	150	CVI	39.98	40.04	0.16	0.48	226.87	218.34	-3.76
HFIR	18J	800	7	T05	Tyranno-SA 3rd	P/W	PyC	150	CVI	39.97	40.04	0.18	0.53	234.73	227.64	-3.02
HFIR	18J	800	7	T06	Tyranno-SA 3rd	P/W	PyC	150	CVI	39.94	40.00	0.14	0.43	268.00	261.20	-2.54
HFIR	18J	1300	7	T15	Tyranno-SA 3rd	P/W	PyC	150	CVI	39.99	40.10	0.27	0.80	259.17	252.87	-2.43
HFIR	18J	1300	7	T16	Tyranno-SA 3rd	P/W	PyC	150	CVI	40.00	40.14	0.35	1.05	250.55	245.42	-2.05
HFIR	18J	1300	7	T27	Tyranno-SA 3rd	P/W	PyC	150	CVI	40.00	40.05	0.13	0.40	244.77	238.07	-2.74
HFIR	18J	1300	7	T28	Tyranno-SA 3rd	P/W	PyC	150	CVI	39.95	40.02	0.17	0.50	256.13	251.46	-1.82
HFIR	18J	1300	7	T29	Tyranno-SA 3rd	P/W	PyC	150	CVI	40.00	40.09	0.23	0.68	266.38	260.15	-2.34
HFIR	18J	1300	7	T30	Tyranno-SA 3rd	P/W	PyC	150	CVI	39.96	40.00	0.09	0.28	243.91	238.29	-2.31
HFIR	18J	800	7	X14	Tyranno-SA 3rd	P/W	PyC	50	CVI	39.99	40.01	0.05	0.15	274.68	272.84	-0.67
HFIR	18J	1300	7	X01	Tyranno-SA 3rd	P/W	PyC	50	CVI	39.97	40.03	0.15	0.45	246.18	242.49	-1.50
HFIR	18J	1300	7	X02	Tyranno-SA 3rd	P/W	PyC	50	CVI	39.95	40.04	0.22	0.65	270.21	266.15	-1.50
HFIR	18J	1300	7	X13	Tyranno-SA 3rd	P/W	PyC	50	CVI	39.94	40.03	0.23	0.68	275.52	270.24	-1.92
HFIR	18J	1300	7	X14	Tyranno-SA 3rd	P/W	PyC	50	CVI	39.99	40.01	0.05	0.15	274.68	272.84	-0.67
HFIR	18J	1300	7	X15	Tyranno-SA 3rd	P/W	PyC	50	CVI	39.94	40.05	0.28	0.83	284.32	281.33	-1.05
HFIR	18J	1300	7	X16	Tyranno-SA 3rd	P/W	PyC	50	CVI	39.98	40.06	0.20	0.60	277.47	273.09	-1.58
HFIR	18J	800	7	F01	Tyranno-SA 3rd	P/W	PyC	150	CVI	39.96	40.02	0.15	0.45	251.57	245.25	-2.51
HFIR	18J	800	7	F02	Tyranno-SA 3rd	P/W	PyC	150	CVI	39.96	40.06	0.25	0.75	253.31	246.84	-2.55
HFIR	18J	800	7	F03	Tyranno-SA 3rd	P/W	PyC	150	CVI	39.97	40.07	0.25	0.75	263.97	254.47	-3.60
HFIR	18J	800	7	F04	Tyranno-SA 3rd	P/W	PyC	150	CVI	39.97	40.05	0.21	0.63	237.00	230.80	-2.61
HFIR	18J	800	7	F05	Tyranno-SA 3rd	P/W	PyC	150	CVI	39.96	40.02	0.15	0.45	226.64	218.35	-3.66
HFIR	18J	800	7	M01	Hi-Nicalon Type-S	P/W	ML		CVI	39.96	40.06	0.24	0.73	241.18	235.82	-2.22

Table 2: (Cont'd)

Reactor	Capsule ID	Temp. [°C]	Fluence [x10^25 n/m^2]	Specimen ID	Fiber	Archi-tecture	Inter-phase	Thick-ness [nm]	Matrix	Length Before Irrad. [mm]	Length After Irrad. [mm]	Length Change [%]	Vol. Swelling [%]	Sonic E Before Irrad. [GPa]	Sonic E After Irrad. [GPa]	% Change In E
HFIR	18J	800	7	M02	Hi-Nicalon Type-S	P/W	ML		CVI	39.99	39.99	0.01	0.03	212.55	205.41	-3.36
HFIR	18J	800	7	M03	Hi-Nicalon Type-S	P/W	ML		CVI	39.98	40.01	0.08	0.25	204.26	197.48	-3.32
HFIR	18J	800	7	M04	Hi-Nicalon Type-S	P/W	ML		CVI	39.98	40.03	0.13	0.40	208.33	202.46	-2.82
HFIR	18J	800	7	M05	Hi-Nicalon Type-S	P/W	ML		CVI	39.96	39.99	0.08	0.23	200.15	194.34	-2.91
HFIR	18J	800	7	M06	Hi-Nicalon Type-S	P/W	ML		CVI	39.97	40.01	0.11	0.33	208.13	201.63	-3.12
HFIR	18J	1300	7	M13	Hi-Nicalon Type-S	P/W	ML		CVI	40.00	40.03	0.08	0.25	219.42	215.02	-2.01
HFIR	18J	1300	7	M14	Hi-Nicalon Type-S	P/W	ML		CVI	39.99	40.03	0.10	0.30	214.70	208.91	-2.69
HFIR	18J	1300	7	M15	Hi-Nicalon Type-S	P/W	ML		CVI	40.00	40.03	0.08	0.25	227.69	224.60	-1.36
HFIR	18J	1300	7	M16	Hi-Nicalon Type-S	P/W	ML		CVI	39.95	40.00	0.13	0.38	202.65	200.85	-0.89
HFIR	18J	1300	7	M17	Hi-Nicalon Type-S	P/W	ML		CVI	39.96	40.07	0.28	0.85	206.48	202.27	-2.04
HFIR	18J	1300	7	M18	Hi-Nicalon Type-S	P/W	ML		CVI	39.97	40.09	0.30	0.90	203.09	197.65	-2.68
HFIR	18J	800	7	H01	Hybrid	3D	PyC	150	CVI	39.98	40.06	0.21	0.63	146.72	143.43	-2.24
HFIR	18J	800	7	H02	Hybrid	3D	PyC	150	CVI	40.00	40.05	0.12	0.35	117.02	104.95	-10.31
HFIR	18J	800	7	H03	Hybrid	3D	PyC	150	CVI	40.00	40.07	0.18	0.53	117.41	105.56	-10.09
HFIR	18J	800	7	H04	Hybrid	3D	PyC	150	CVI	40.01	40.07	0.15	0.45	96.77	94.16	-2.70
HFIR	18J	800	7	H05	Hybrid	3D	PyC	150	CVI	39.96	40.07	0.27	0.80	99.75	94.94	-4.82
HFIR	18J	800	7	H06	Hybrid	3D	PyC	150	CVI	39.97	40.05	0.19	0.58	127.12	126.36	-0.60
HFIR	18J	800	7	N01	Tyranno-SA 3rd	UD	PyC	500	NITE	40.02	40.08	0.15	0.45	325.23	323.92	-0.40
HFIR	18J	800	7	N02	Tyranno-SA 3rd	UD	PyC	500	NITE	40.03	40.11	0.19	0.58	336.08	324.58	-3.42
HFIR	18J	800	7	N03	Tyranno-SA 3rd	UD	PyC	500	NITE	40.02	40.05	0.07	0.23	334.54	336.35	0.54
HFIR	18J	800	7	N04	Tyranno-SA 3rd	UD	PyC	500	NITE	40.04	40.07	0.07	0.20	323.58	320.56	-0.93
HFIR	18J	800	7	N05	Tyranno-SA 3rd	UD	PyC	500	NITE	40.02	40.07	0.12	0.38	332.38	337.48	1.53
HFIR	18J	800	7	N06	Tyranno-SA 3rd	UD	PyC	500	NITE	40.02	40.08	0.15	0.45	335.34	340.44	1.52
HFIR	18J	800	7	N15	Tyranno-SA 3rd	UD	PyC	500	NITE	40.04	40.09	0.13	0.40	329.41	326.55	-0.87
HFIR	18J	1300	7	N13	Tyranno-SA 3rd	UD	PyC	500	NITE	40.03	40.09	0.15	0.45	345.83	347.03	0.35
HFIR	18J	1300	7	N14	Tyranno-SA 3rd	UD	PyC	500	NITE	40.02	40.11	0.22	0.65	350.86	350.30	-0.16
HFIR	18J	1300	7	N16	Tyranno-SA 3rd	UD	PyC	500	NITE	40.02	40.10	0.20	0.60	333.34	336.23	0.87
HFIR	18J	800	7	S1	Hi-Nicalon Type-S	S/W	PyC		ICVI	39.95	40.00	0.14	0.41	-	217.41	-
HFIR	18J	800	7	S2	Hi-Nicalon Type-S	S/W	PyC		ICVI	39.99	40.03	0.10	0.30	-	232.62	-

Table 2: (Cont'd)

Reactor	Capsule ID	Temp. [°C]	Fluence [x10^25 n/m^2]	Specimen ID	Fiber	Archi-tecture	Inter-phase	Thick-ness [nm]	Matrix	Length Before Irrad. [mm]	Length After Irrad. [mm]	Length Change [%]	Vol. Swelling [%]	Sonic E Before Irrad. [GPa]	Sonic E After Irrad. [GPa]	% Change In E
HFIR	18J	800	7	S3	Hi-Nicalon Type-S	S/W	PyC		ICVI	39.99	40.00	0.04	0.11	-	219.91	-
HFIR	18J	800	7	S4	Hi-Nicalon Type-S	S/W	PyC		ICVI	39.98	40.07	0.22	0.67	-	224.72	-
HFIR	18J	800	7	S5	Hi-Nicalon Type-S	S/W	PyC		ICVI	40.00	39.99	-0.03	-0.10	-	230.65	-
HFIR	18J	800	7	S6	Hi-Nicalon Type-S	S/W	PyC		ICVI	40.00	40.03	0.08	0.23	-	224.03	-
HFIR	18J	1300	7	S19	Hi-Nicalon Type-S	S/W	PyC		ICVI	39.97	40.04	0.18	0.53	-	291.45	-
HFIR	18J	1300	7	S20	Hi-Nicalon Type-S	S/W	PyC		ICVI	39.89	39.96	0.17	0.51	-	291.02	-
HFIR	18J	1300	7	S21	Hi-Nicalon Type-S	S/W	PyC		ICVI	39.96	39.99	0.08	0.24	-	281.93	-
HFIR	18J	1300	7	S22	Hi-Nicalon Type-S	S/W	PyC		ICVI	40.00	40.07	0.17	0.52	-	268.55	-
HFIR	18J	800	7	A01	Hi-Nicalon Type-S	P/W	PyC	150	CVI	39.99	40.03	0.09	0.28	228.29	205.52	-9.97
HFIR	18J	800	7	A02	Hi-Nicalon Type-S	P/W	PyC	150	CVI	39.97	40.03	0.15	0.45	202.18	182.76	-9.60
HFIR	18J	800	7	A03	Hi-Nicalon Type-S	P/W	PyC	150	CVI	39.96	40.03	0.17	0.50	229.21	206.02	-10.12
HFIR	18J	800	7	A04	Hi-Nicalon Type-S	P/W	PyC	150	CVI	39.94	40.04	0.24	0.73	230.11	207.37	-9.89
HFIR	18J	800	7	A05	Hi-Nicalon Type-S	P/W	PyC	150	CVI	39.96	40.03	0.18	0.53	239.78	220.57	-8.01
HFIR	18J	800	7	A06	Hi-Nicalon Type-S	P/W	PyC	150	CVI	40.00	40.05	0.12	0.38	219.02	193.18	-11.80
HFIR	18J	800	7	A07	Hi-Nicalon Type-S	P/W	PyC	150	CVI	39.98	40.06	0.19	0.58	207.68	188.66	-9.16
HFIR	18J	800	7	A08	Hi-Nicalon Type-S	P/W	PyC	150	CVI	39.93	40.03	0.24	0.73	233.81	209.37	-10.45
HFIR	18J	1300	7	A13	Hi-Nicalon Type-S	P/W	PyC	150	CVI	39.99	40.00	0.03	0.10	210.55	185.44	-11.92
HFIR	18J	1300	7	A14	Hi-Nicalon Type-S	P/W	PyC	150	CVI	39.94	39.98	0.09	0.28	210.90	187.70	-11.00
HFIR	18J	1300	7	A15	Hi-Nicalon Type-S	P/W	PyC	150	CVI	39.95	39.98	0.08	0.23	229.53	203.24	-11.45
HFIR	18J	1300	7	A16	Hi-Nicalon Type-S	P/W	PyC	150	CVI	39.98	40.01	0.08	0.25	218.14	190.48	-12.68
HFIR	18J	800	7	E01	Hi-Nicalon Type-S	P/W	PyC	50	CVI	40.01	40.04	0.08	0.25	236.23	221.27	-6.33
HFIR	18J	800	7	E02	Hi-Nicalon Type-S	P/W	PyC	50	CVI	39.95	39.98	0.08	0.23	226.30	210.55	-6.96
HFIR	18J	800	7	E03	Hi-Nicalon Type-S	P/W	PyC	50	CVI	39.97	40.01	0.10	0.30	188.68	181.35	-3.88
HFIR	18J	800	7	E04	Hi-Nicalon Type-S	P/W	PyC	50	CVI	40.00	40.04	0.10	0.30	237.96	217.90	-8.43
HFIR	18J	800	7	E05	Hi-Nicalon Type-S	P/W	PyC	50	CVI	39.95	39.99	0.10	0.30	-	-	-
HFIR	18J	800	7	E06	Hi-Nicalon Type-S	P/W	PyC	50	CVI	40.01	40.03	0.06	0.18	214.71	203.85	-5.06
HFIR	18J	800	7	E07	Hi-Nicalon Type-S	P/W	PyC	50	CVI	39.95	40.01	0.15	0.45	222.35	209.52	-5.77
HFIR	18J	800	7	E08	Hi-Nicalon Type-S	P/W	PyC	50	CVI	40.01	40.04	0.08	0.25	226.26	209.42	-7.44

Table 3: Average values of volumetric swelling and dynamic modulus after neutron irradiation. Temperatures shown are nominal values. E; elastic modulus, Hybrid; combination of Tyranno-SA 3rd SiC fiber and P-120 carbon fiber, UD; uni-directional, P/W; plain-woven, S/W; satin-woven, 3D; 3D orthogonal, PyC; pyrolytic carbon, ML; multi-layered, P-SiC; porous SiC, ICVI; isothermal chemically vapor infiltration.

Reactor	Capsule ID	Temp. [°C]	Fluence [x10^25 n/m^2]	Specimen ID	Fiber	Archi-tecture	Inter-phase	Thick-ness [nm]	Matrix	Vol. Swelling [%]	Standard dev. [%]	Retention of E [%]	Standard dev.	# of tests
JMTR	00M-95U	1000	1	TP	Tyranno-SA 1st	UD	PyC	520	ICVI	0.43	0.60	-	-	6
JMTR	00M-95U	1000	1	TM	Tyranno-SA 1st	UD	ML		ICVI	0.29	0.11	-	-	6
JMTR	00M-95U	1000	1	SP	Hi-Nicalon Type-S	UD	PyC	520	ICVI	0.35	0.14	-	-	4
JMTR	00M-95U	1000	1	ST	Hi-Nicalon Type-S	UD	PyC	720	ICVI	0.44	0.25	-	-	5
JMTR	00M-95U	1000	1	SM	Hi-Nicalon Type-S	UD	ML		ICVI	0.33	0.18	-	-	5
JMTR	00M-95U	1000	1	SS	Hi-Nicalon Type-S	UD	P-SiC	380	ICVI	0.27	0.12	-	-	6
JMTR	05M-19U	600	0.52	TS06-UD	Tyranno-SA 3rd	UD	PyC	500	NITE	1.00	0.16	-	-	5
JMTR	05M-19U	800	0.77	TS06-UD	Tyranno-SA 3rd	UD	PyC	500	NITE	0.74	0.21	-	-	2
JMTR	05M-19U	600	0.52	TS06-XP	Tyranno-SA 3rd	C/P	PyC	500	NITE	1.07	0.26	-	-	5
JMTR	05M-19U	800	0.77	TS06-XP	Tyranno-SA 3rd	C/P	PyC	500	NITE	0.81	0.07	-	-	4
JMTR	05M-19U	600	0.52	TS06-AN	Tyranno-SA 3rd	C/P	PyC	500	NITE	1.17	0.12	-	-	5
JMTR	05M-19U	800	0.77	TS06-AN	Tyranno-SA 3rd	C/P	PyC	500	NITE	0.77	0.18	-	-	5
HFIR	18J	800	7	T	Tyranno-SA 3rd	P/W	PyC	150	CVI	0.50	0.07	96.73	0.49	5
HFIR	18J	1300	7	T	Tyranno-SA 3rd	P/W	PyC	150	CVI	0.58	0.30	97.75	0.34	5
HFIR	18J	800	7	X	Tyranno-SA 3rd	P/W	PyC	50	CVI	0.15	-	99.33	-	1
HFIR	18J	1300	7	X	Tyranno-SA 3rd	P/W	PyC	50	CVI	0.56	0.23	98.63	0.44	6
HFIR	18J	800	7	F	Tyranno-SA 3rd	P/W	PyC	150	CVI	0.61	0.15	97.01	0.59	5
HFIR	18J	800	7	M	Hi-Nicalon Type-S	P/W	ML		CVI	0.33	0.23	97.04	0.42	6
HFIR	18J	1300	7	M	Hi-Nicalon Type-S	P/W	ML		CVI	0.49	0.31	98.06	0.72	6
HFIR	18J	800	7	H	Hybrid	3D	PyC	150	CVI	0.56	0.16	94.87	4.16	6
HFIR	18J	800	7	N	Tyranno-SA 3rd	UD	PyC	500	NITE	0.38	0.14	99.81	1.87	6
HFIR	18J	1300	7	N	Tyranno-SA 3rd	UD	PyC	500	NITE	0.53	0.12	100.05	0.74	4
HFIR	18J	800	7	S	Hi-Nicalon Type-S	S/W	PyC		ICVI	0.27	0.26	-	-	6
HFIR	18J	1300	7	S	Hi-Nicalon Type-S	S/W	PyC		ICVI	0.45	0.14	-	-	4
HFIR	18J	800	7	N601-3	Tyranno-SA 3rd	UD	PyC	500	NITE	0.50	0.34	98.60	3.28	3
HFIR	18J	1300	7	N604-6	Tyranno-SA 3rd	UD	PyC	500	NITE	0.45	0.24	100.65	1.01	3
HFIR	18J	800	7	A	Hi-Nicalon Type-S	P/W	PyC	150	CVI	0.52	0.16	90.13	1.08	8

Table 3: (Cont'd)

Reactor	Capsule ID	Temp. [°C]	Fluence [x10^25 n/m^2]	Specimen ID	Fiber	Archi-tecture	Inter-phase	Thick-ness [nm]	Matrix	Vol. Swelling [%]	Standard dev. [%]	Retention of E [%]	Standard dev.	# of tests
HFIR	18J	1300	7	A	Hi-Nicalon Type-S	P/W	PyC	150	CVI	0.21	0.08	88.24	0.72	4
HFIR	18J	800	7	E	Hi-Nicalon Type-S	P/W	PyC	50	CVI	0.28	0.08	93.73	1.52	8
HFIR	18J	800	7	K601-4	Tyranno-SA 3rd	UD	PyC	500	NITE	0.99	0.41	98.78	1.80	4
HFIR	18J	1300	7	K611-4	Tyranno-SA 3rd	UD	PyC	500	NITE	-0.06	0.52	100.40	3.35	4

References

[1] Y. Katoh, L.L. Snead, C.H. Henager Jr, A. Hasegawa, A. Kohyama, B. Riccardi, H. Hegeman, Journal of Nuclear Materials 367-370 (2007) 659.

[2] T. Nozawa, T. Hinoki, A. Hasegawa, A. Kohyama, Y. Katoh, L.L. Snead, C.H. Henager Jr, J.B.J. Hegeman, Journal of Nuclear Materials 386-388 (2009) 622.

[3] L.L. Snead, Y. Katoh, S. Connery, Journal of Nuclear Materials 367-370 (2007) 677.

[4] L.L. Snead, T. Nozawa, Y. Katoh, T.-S. Byun, S. Kondo, D.A. Petti, Journal of Nuclear Materials 371 (2007) 329.

[5] Y. Katoh, N. Hashimoto, S. Kondo, L.L. Snead, A. Kohyama, Journal of Nuclear Materials 351 (2006) 228.

[6] Y. Katoh, H. Kishimoto, A. Kohyama, Journal of Nuclear Materials 307-311 (2002) 1221.

[7] S. Kondo, Y. Katoh, L.L. Snead, Journal of Nuclear Materials 386-388 (2009) 222.

[8] S. Kondo, Y. Katoh, L.L. Snead, Journal of Nuclear Materials 382 (2008) 160.

[9] G. Newsome, L.L. Snead, T. Hinoki, Y. Katoh, D. Peters, Journal of Nuclear Materials 371 (2007) 76.

[10] G.W. Hollenberg, C.H. Henager, G.E. Youngblood, D.J. Trimble, S.A. Simonson, G.A. Newsome, E. Lewis, Journal of Nuclear Materials 219 (1995) 70.

[11] L.L. Snead, M.C. Osborne, R.A. Lowden, J. Strizak, R.J. Shinavski, K.L. More, W.S. Eatherly, J. Bailey, A.M. Williams, Journal of Nuclear Materials 253 (1998) 20.

[12] J.B.J. Hegeman, J.G. van der Laan, M. van Kranenburg, M. Jong, D. d'Hulst, P. ten Pierick, Fusion Engineering and Design 75-79 (2005) 789.

[13] T. Hinoki, L.L. Snead, E. Lara-Curzio, Y. Katoh, A. Kohyama, Fusion Materials Semiannual Progress Report DOE/ER-0313/29 (2000) 74.

[14] T. Nozawa, K. Ozawa, S. Kondo, T. Hinoki, Y. Katoh, L.L. Snead, A. Kohyama, Journal of ASTM International 2 (2005) 12884.

[15] K. Ozawa, T. Hinoki, T. Nozawa, Y. Katoh, Y. Maki, S. Kondo, S. Ikeda, A. Kohyama, Materials Transactions 47 (2006) 207.

[16] Y. Katoh, K. Ozawa, L.L. Snead, Y.B. Choi, T. Hinoki, A. Hasegawa, Fusion Materials Semiannual Progress Report DOE/ER-0313/45 (2008) 21.

[17] R. Blackstone, E.H. Voice, Journal of Nuclear Materials 39 (1971) 319.

[18] L.L. Snead, S.J. Zinkle, Nuclear Instruments and Methods in Physics Research Section B: Beam Interactions with Materials and Atoms 191 (2002) 497.

[19] R.J. Price, Journal of Nuclear Materials 33 (1969) 17.

[20] R.J. Price, Journal of Nuclear Materials 48 (1973) 47.

[21] Y. Katoh, L.L. Snead, Fusion Science and Technology 56 (2009) 1045.

A REVIEW OF RECENT WORK ON FATIGUE RESPONSE IN FERRITIC/MARTENSITIC STEELS –
D. S. Gelles (Pacific Northwest National Laboratory)*

OBJECTIVE

The objective of this effort is to summarize recent work on fatigue and creep-fatigue response in ferritic/martensitic steels in order to identify those areas where further work would be fruitful.

SUMMARY

The recent literature on fatigue and creep-fatigue response of ferritic/martensitic steels has been reviewed with particular emphasis on that of interest to the fusion materials community. A range of alloys has been studied including low activation martensitic steels developed in Japan and Europe as well as some work on ODS steels of interest. The results show that all these martensitic steels behave similarly, that ODS steels provide improvement, that irradiation tends to reduce fatigue lifetimes, and that simultaneous helium and hydrogen injection can be very deleterious. Work done on 9Cr-1Mo in support of Gen VI demonstrates that creep-fatigue lifetimes will be controlled by cracking of surface oxides. It may be necessary to test in a fusion environment in order to accurately predict ferritic/martensitic steel fatigue response for a fusion machine.

PROGRESS AND STATUS

Review of the literature

This effort is intended to review recent work in the field of fatigue and fatigue-creep interaction for ferritic-martensitic steels of interest to the fusion materials development community in order to indentify those areas where future efforts might be directed effectively.

Since the introduction of a ferritic steel option to the USDOE Fusion Reactor Materials mission in 1979, it has been apparent that the fatigue response in this class of materials would be of considerable interest, due to both thermal and stress cycling. As a result, a number of such studies have been made around the world in support of a fusion energy system. This report will attempt to review the last five or so years of such efforts.

At the 21st American Society for Testing and Materials (ASTM) symposium on Effects of Radiation on Materials, Li and Stubbins [1] reviewed the US and European literature in order to provide comparison with a predictive model based on tensile behavior. The ferritic alloy data they chose to analyze were for MANET (DIN 1.4914), of composition Fe-10.6Cr-0.87Ni-0.82Mn-0.77Mo-0.37Si-0.22V-0.12C-.02N and HT9, Fe-11.5Cr-1Mo-0.55Mn-0.5W-0.4Si-0.3V-0.2C, both before and after irradiation. That review included a plot of fatigue lives for ferritic/martensitic steels MANET and HT9, reproduced in Figure 1. From this work they concluded that pre- and post-irradiation fatigue behavior in ferritic/martensitic is more complex than can be predicted quantitatively from simple tensile test results, (at least in part because fatigue-softening occurred), and that a microstructural-level understanding of the flow mechanisms is necessary to provide guidance about fatigue performance.

The effort to understand fatigue response of ferritic/martensitic steels in Asia has centered on work in Japan based on low activation steels (F82H, Fe-8Cr-2W [2-4] and JLF-1, Fe-9Cr-2W [5-9]), but 9Cr-1Mo [10-11], 12Cr-2W [12] and oxide dispersion strengthened (ODS) alloys [13] were also studied.

The effort on F82H, a low activation martensitic steel developed in Japan and distributed by JAERI to interested researchers was included in Japanese low dose irradiation experiments taken to 0.02 dpa at

* Pacific Northwest National Laboratory (PNNL) is operated for the U.S. Department of Energy by Battelle Memorial Institute under contract DE-AC06-76RLO-1830.

temperatures of 100, 150 and 200ºC [2,4]. Results were similar to those given by Li and Stubbins in Figure 1, about intermediate between HT9 and MANET for unirradiated conditions and similarly reduced following irradiation. A study examining surface finish on fatigue response demonstrated a degradation of ~2 in fatigue life with surface roughness and showed that cracks initiate preferentially on scratches remaining from machining [3].

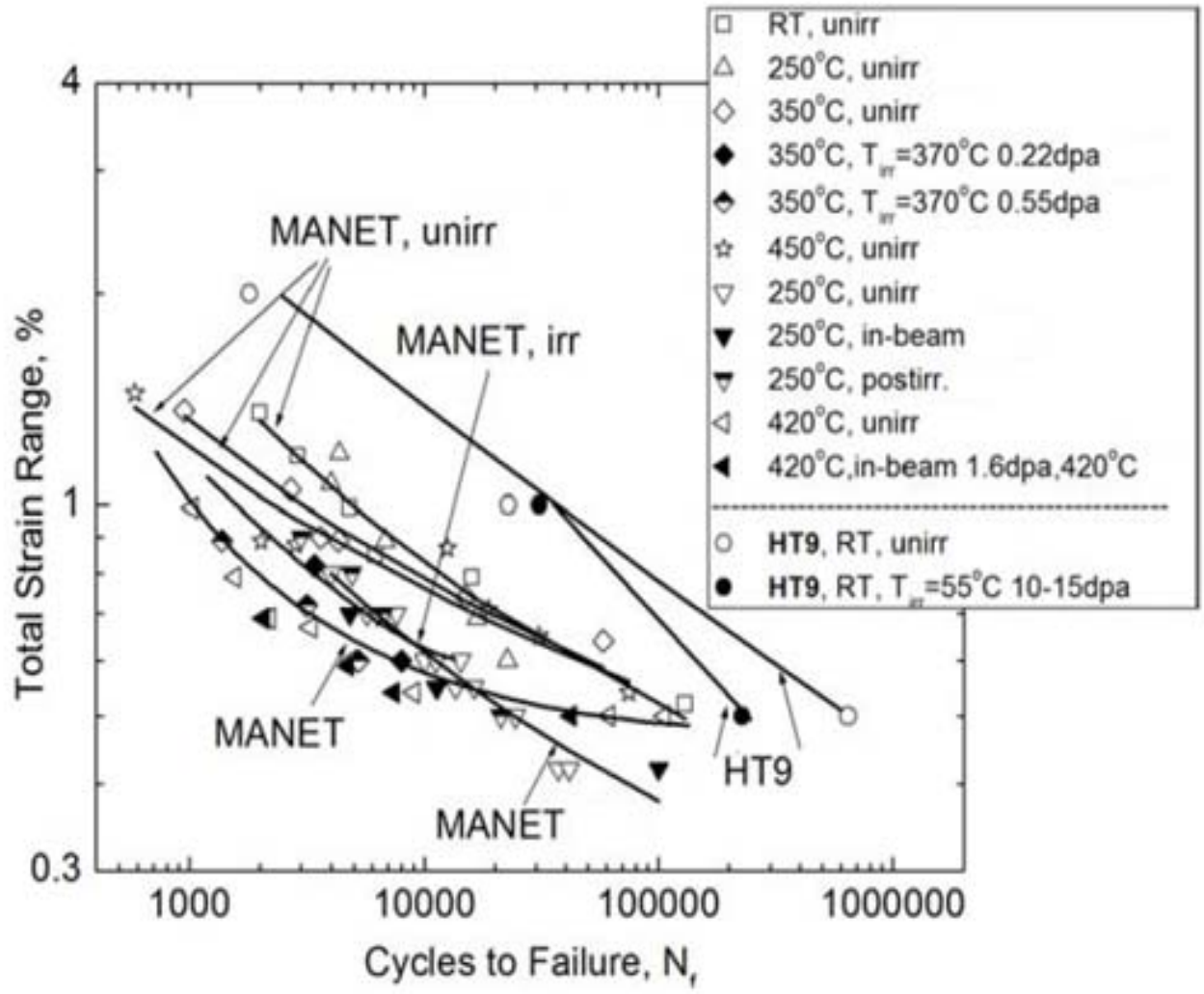

Figure 1. Comparison of the fatigue lives for ferritic/martensitic steels MANET and HT9 in unirradiated and irradiated conditions as a function of temperature, taken from [1].

The JLF low activation martensitic steels were developed by the Japanese University fusion community, and initial experiments were intended to reduce specimen size in order to optimize irradiation experiments [5-7]. Approximately quarter-sized specimens resulted in no significant change in lifetimes at stress amplitudes of ~500 MPa but with a small decrease in slope with stress amplitude. Later experiments demonstrated cyclic softening and reduced lifetimes in TIG weldmetal conditions [6,7]. The JLF steel was also used to provide microstructural analysis of the consequences of fatigue deformation [8-9]. Cyclic softening was found to be caused by reduction of the dislocation density and increase in lath width with no apparent change in carbide size. It was also noted that fatigue life was independent of temperature when plotted against total strain but not against plastic strain (as used by the Coffin model).

There were various efforts on modified 9Cr-1Mo and a 12Cr-2W pipe steel. The first characterized the microstructure during creep-fatigue and showed that the ultrasonic velocity was dependent on the microstructural changes. This was attributed to first a loss in dislocation density and then to a decrease in solute atoms in solution resulting from MX precipitation [10]. As a consequence, non-destructive ultrasonic evaluations can be used to monitor creep-fatigue response. A second effort evaluated a sodium environment on low-cycle fatigue properties and found that the evolution of cyclic stress response was similar to that in air, but lifetimes were significantly increased. This was attributed to the lack of oxidation in the sodium environment and a resulting delay in crack initiation, an effect expected to be more pronounced at lower strain ranges.

Finally, results were provided for low-cycle fatigue properties of ODS ferritic/martensitic steels at high temperatures. Both 9Cr and 12Cr steels were tested with compositions at 2%W, ~0.2%Ti and ~0.3%Y_2O_3, the former containing 0.14%C and therefore martensitic. Both ODS steels were found to have similar fatigue properties but showed superior fatigue life and negligible cyclic softening compared to conventional ferritic/martensitic steels. These differences were attributed to the higher yield strengths for ODS alloys which leads to lower fractions of plastic strain under strain-controlled fatigue conditions.

European efforts were largely centered on low activation steel Eurofer 97, Fe-9Cr-1W-0.2V-0.15Ta-0.1C-0.02N [14-19] but one study included a range of low activation steels [20], as well as 9Cr-1Mo [21-25] and a steel similar to HT9, X12CrMoWVNbN10-1-1 but actually containing ~10Cr-1Mo-1W-0.1C [26]. A modeling effort on the influence of irradiation was also produced [27].

Eurofer 97 was a low activation martensitic alloy prepared for European experimentation. It was found to undergo significant irradiation hardening following low temperature irradiation, as severe as HT9, but provides material comparable to F82H and JLF-1 for fatigue studies. Comparison with Figure 1 reveals that Eurofer 97 has fatigue properties similar to but below those of MANET by about a factor of 2 in lifetime [18]. Early tests in air indicated that oxide formation probably enhanced crack propagation indicating the need for testing in a fusion environment [14]. This issue was then addressed for the case of in-situ testing using 590 MeV protons in a cooling gas, so that H and He were injected during irradiation and fatigue testing [15]. It was found that irradiation strongly reduced cyclic life, concurrent with radiation induced hardening. However, this in-beam damage could be readily recovered by further cyclic deformation with the beam off so that lifetimes were then on the order of tests without irradiation. The influence of hydrogen embrittlement was examined using cathodic charging and testing at room temperature [16]. Both base metal and joints of Eurofer 97 were indeed found to be susceptible to hydrogen embrittlement, but it was noted that such problems might be mitigated by proper microstructural control. A low cycle fatigue study of Eurofer 97 concluded that Eurofer 97 behaved similarly to F82H and MANET at room temperature and showed no significant effect of temperature from 150 to 550ºC on fatigue life [18]. Hold times of 500s were also applied, and at high imposed strains, no strong differences were found even at 550ºC, whereas for low imposed strains there was a strong life reduction and significant softening was noted. Concurrent microstructural studies showed that the major changes during fatigue were a decrease in dislocation density and decomposition of the lath structure into submicron equiaxed subgrains. Multiaxial fatigue behavior has also been studied showing further reduction in lifetime [17,19], and it was demonstrated that fatigue design curves based on uniaxial tests are not sufficiently conservative. Finally, Eurofer 97 was compared to F82H and an ODS Eurofer variant following irradiation at 330ºC up to ~30 dpa [20]. It was found that all alloys showed improved fatigue life following irradiation for low values of total strain range, but Eurofer 97 response was significantly degraded compared to unirradated material at higher values of total strain range.

Fatigue studies outside the fusion community (and in support of accelerator systems or Gen-IV nuclear reactors) were largely based on 9Cr-1Mo compositions. The addition of a FeCrAlY surface modification was determined to result in similar fatigue response at 550ºC for both tests in air and in $Pb_{55}Bi_{45}$ [21]. A series of papers considered creep-fatigue-oxidation interactions and included tensile and compressive hold periods and a lifetime prediction [22-24]. Creep-fatigue tests were found to be more deleterious than equivalent relaxation-fatigue tests and compressive hold periods were worse than tensile ones. Both the mean stress effect and environmentally-assisted crack initiation may be responsible. Note that for

compressive creep-fatigue hold periods, the oxide layer is mainly subjected to tensile stresses (and conversely for tensile hold periods) resulting in enhance oxide scale cracking. Based on an understanding of the controlling physical mechanisms gained from these studies, two scenarios were proposed for the interaction between fatigue, creep and oxidation damage, and a model for creep-fatigue lifetime was developed that accurately predicts pure fatigue lifetimes for $\Delta\epsilon_{fat} \geq 0.4\%$ [24]. This work was further summarized in a later paper and the two cracking scenarios were diagrammed [25]. Studies on Fe-10Cr-Mo-1W-0.1C steels gave cyclic softening results similar to other studies and correlated it with significant subgrain coarsening. Also, cyclic deformation was shown to affect the subsequent minimum creep rate by a factor of 6.

Finally, modeling of fatigue response is being attempted on several fronts. European fusion materials work considers consequences of irradiation damage mechanisms and develops a model to predict behavior in Eurofer 97 [27]. A conference on residual stress and its effect on fatigue and fracture considered low alloy steel behavior but was mainly concerned with assessment of defects [28]. Discrete dislocation dynamics modeling is being used to understand dislocation-crack interactions during fatigue and showed that even during compression with the crack tip closed and the specimen behaving like an uncracked specimen, the dislocation structure can result in lower yield stresses than one would obtain where no cross-slip were allowed [29].

Discussion

Studies of fatigue response for several ferritic/martensitic steels have been performed around the world. Alloying variations resulted in only minor differences in behavior, and irradiation degraded response. Several researchers concluded that behavior was controlled by a breakdown of the martensite lath dislocation substructure and reconfiguration into a coarser subgrain structure, as opposed to carbide coarsening or refinement.

The fatigue response of martensitic steels can be understood based on these reported microstructure changes, as follows. The microstructure of air-cooled martensitic steels is a result of a martensite reaction that leaves a thin layer of carbon-rich retained austenite at lath boundaries [30]. This is because there is sufficient diffusion of carbon to allow the carbon to stay ahead of growing martensite laths. During tempering or normalization, the retained austenite provides sites for carbide precipitation and the high density dislocation structure generated by the martensite reaction relaxes into a substructure pinned by the carbide obstacles. The resultant lath- or subgrain-structure is much finer than that which would result during high temperature creep or fatigue testing, and therefore, the creep and fatigue response are initially reduced by this controlling substructure. However, as fatigue and high temperature creep proceed, this artificially induced dislocation substructure breaks down to one more characteristic of the applied stresses, and the material softens. Reduced fatigue response due to irradiation without simultaneous gas injection is most probably a result of enhanced embrittlement found in these steels.

The fatigue lifetime is dependent on initiation and growth of a crack. These critical cracks generally initiate at specimen surfaces, and therefore surface condition, whether it be from machining artifacts or surface oxide irregularities, will control response. In irradiation experiments where gas was injected during irradiation [15], fatigue lifetimes decreased markedly. Apparently, internal cracking was enhanced by gas injection to the point where critical internal cracks could be developed. However, when irradiation and concurrent gas injection were stopped and the fatigue testing was continued, failure was a result of a critical surface crack.

Opportunities therefore exist in modeling fatigue behavior based on this microstructural description, both for the influence of effective subgrain size on fatigue response and the consequence of injected gas on internal critical crack initiation. Future work could therefore include validating the above description with further microstructural studies and modeling it. Dislocation dynamics modeling of similar behavior has been successful.

However, from this review, it is apparent that the irradiation environment will likely play a critical role in determining fatigue and fatigue-creep response in a fusion machine. We may therefore have to wait until such an environment can be created before fusion relevant tests can be made.

Conclusions

The recent literature on fatigue and creep-fatigue response of ferritic/martensitic steels has been reviewed with particular emphasis on work of interest to the fusion materials community. A range of alloys has been studied including low activation martensitic steels developed in Japan and Europe as well as some work on ODS steels of interest. The results show that all these martensitic steels behave similarly, that ODS steels provide improvement, that irradiation tends to reduce fatigue lifetimes, and that simultaneous helium and hydrogen injection can be very deleterious. The response appears to be a consequence of microstructural changes rather than strength variations. However, creep-fatigue lifetimes in air appear to be controlled by cracking of surface oxides. A fusion environment may be needed in order to accurately predict fatigue response in a fusion machine.

References

[1] M. L. Li and J. F Stubbins, J. ASTM Intl., 1 (2004) paper JA11334 or Effects of Radiation on Materials, ASTM STP 1447, (2004) 502.
[2] T. Hirose, H. Tanagawa, M. Ando, A. Kohyama, Y. Katoh and M. Narui, J. Nucl. Mater., 303-311 (2002) 304.
[3] S. W. Kim, H. Tanigawa, T. Hirose, K. Shiba and A. Kohyama, J. Nucl. Mater., 367-370 (2007) 568.
[4] S. W. Kim, H. Tanigawa, T. Hirose and A. Kohyama, J. Nucl. Mater., 386-388 (2009) 529.
[5] T. Hirose, H. Sakasegawa, A. Kohyama, Y. Katoh and H. Tanigawa, J. Nucl. Mater., 283-287 (2000) 1018.
[6] T. Hirose, H. Sakasegawa, A. Kohyama, Y. Katoh and H. Tanigawa, in Effects of Radiation on Materials, ASTM STP 1405, (2001) 535.
[7] S. W. Kim, H. K. Yoon, W. J. Park and A. Kohyama, J. Nucl. Mater., 329-333 (2004) 248.
[8] H. Li, A. Nishimura, T. Muroga and T. Nagasaka, J. Nucl. Mater., 367-370 (2007) 147.
[9] H. Li, A. Nishimura, T. Muroga and T. Nagasaka, J. Nucl. Mater., 386-388 (2009) 433.
[10] C. S. Kim, S. I. Kwun and I. K. Park, J. Nucl. Mater., 377 (2008) 496.
[11] R. Kannan, R, Sandhya, V. Ganesan, M. Valsan and K. B. S. Rao, J. Nucl. Mater., 384 (2009) 286.
[12] M. Kimura, K. Yamaguchi, M. Hayakawa, K. Kobayashi, K. Kanazawa, Intl. J. Fatigue, 28 (2006) 300.
[13] S. Ukai and S. Ohtsuka, J. Nucl. Mater., 367-370 (2007) 234.
[14] J. Aktaa and M. Lerch, J. Nucl. Mater., 353 (2006) 101.
[15] P. Marmy, J. Nucl. Mater., 367-370 (2007) 86.
[16] M-F. Maday and L. Pilloni, J. Nucl. Mater., 367-370 (2007) 516.
[17] M. Weick and J. Aktaa, J. Nucl. Mater., 367-370 (2007) 633.
[18] P. Marmy and T. Kruml, J. Nucl. Mater., 377 (2008) 52.
[19] J. Aktaa, M. Weick and C. Petersen, J. Nucl. Mater., 386-388 (2009) 911.
[20] C. Petersen, A. Povstryanko, V. Prokhorov, S. Fedoseev, O. Makarov and M. Walter, J. Nucl. Mater., 386-388 (2009) 299.
[21] A. Weisenburger, A. Heinzel, C. Gazio, G. Müller, V. G. Markow, and A. D. Kastanov, J. Nucl. Mater., 377 (2008) 261.
[22] B. Fournier, M, Sauzay, C. Caës, M. Noblecourt, M. Mottot, A. Bougault, V. Rabeau and A. Pineau, Intl. J. Fatigue, 30 (2008) 649.
[23] B. Fournier, M, Sauzay, C. Caës, M. Noblecourt, M. Mottot, A. Bougault, V. Rabeau and A. Pineau, Intl. J. Fatigue, 30 (2008) 663.
[24] B. Fournier, M, Sauzay, C. Caës, M. Noblecourt, M. Mottot, A. Bougault, V. Rabeau, J. Man, O. Gillia, P. Lemoine and A. Pineau, Intl. J. Fatigue, 30 (2008) 1797.
[25] B. Fournie, M, Sauzay, C. Caës, M. Noblecourt, V. Rabeau, A. Bougault, and A. Pineau, J. Nucl. Mater., 386-388 (2009) 418.

[26] J. S. Dubey, H. Chilukuru, J. K. Chakravartty, M. Schwienheer, A. Scholz and W. Blum, Matl. Sci. Eng. A 406 (2005) 152.
[27] J. Aktaa and C. Petersen, J. Nucl. Mater., 389 (2009) 432.
[28] Residual stress and its effect on fatigue and fracture, A. G. Youtsos, editor, (Springer, Dordrecht, The Netherland, 2006)
[29] I. N. Mastorakos and H. M. Zbib, J. ASTM Intl., 4 (2007) Paper ID JAI100705 or Effects of Radiation on Materials, ASTM STP 1492, (2008) 197.
[30] T. A. Lichtenberg, DOE/ER-0045/5 (10-12, 1980) 143.

Characterization of the Composition and Structure of Y-Ti-O Rich Precipitates in Nanostructured Ferritic Alloy MA957 by Transmission Electron Microscopy and Atom Probe Tomography -

N. J. Cunningham, Y. Wu, E. Haney and G. R. Odette (University of California Santa Barbara)

SUMMARY

Nano-dispersion strengthened ferrite alloys (NFA) show great promise for structural applications in severe fusion reactor environments. NFA contain an ultra high density of Y-Ti-O enriched nanofeatures (NF) that, along with fine grains and high dislocation densities, provide high tensile, creep and fatigue strength. The NF are remarkably thermally stable and trap He in fine scale bubbles, thereby suppressing fast fracture embrittlement at lower temperatures, void swelling at intermediate temperatures and degradation of creep rupture properties at high temperatures. However, the precise characteristics of various NF are not yet well understood. They appear to range from coherent solute enriched GP-type zones to near stoichiometric complex oxides, such as Y_2TiO_5 and $Y_2Ti_2O_7$. Here we summarize a recent effort to clarify the characteristics of NF for a reference NFA, MA957, based on the application of several complementary micro-analytical characterization techniques. High-resolution transmission electron microscopy (HRTEM)-Fast Fourier Transform (FFT) power spectra diffraction patterns indicate that the larger features (> 10 nm) are primarily Y_2TiO_5. Limited diffraction data show the smaller features (≈5 nm) are not consistent with known oxide phases. Energy dispersive x-ray (EDX) measurements yield average feature compositions of Y/Ti/O ≈ 27/20/53 for both larger and smaller features. In contrast, atom probe tomography data show average solute compositions of Y/Ti/O = 14/41/45 and Y/Ti/O = 20/32/48 for the smaller and larger features, respectively. The APT data also suggest that even the larger particles contain significant quantities of Fe, and to a lesser extent Cr, which are not observed in the EDX measurements.

Introduction and Background

Different micro-analytical characterization techniques yield different conclusions regarding the compositions and structures of the NF in NFA. For example, atom probe tomography (APT) studies show that NF have complex structures composed of Y-Ti-O enriched cores surrounded by Ti-O rich shells, possibly further surrounded by a more diffuse distribution of higher O concentration [1,2]. APT data also indicates that the non-stoichiometric NF have high Ti/Y ratios (typically about 2-4/1) as well as high (Y+Ti)/O ratios greater than 1 (typically 1.25-1.5/1) [1-8]. The APT data, derived from normal reconstruction methods, also generally suggest that the NF contain large quantities of Fe (30-70%). In contrast, most transmission electron microscopy (TEM) studies have typically found complex oxides (Y_2TiO_5 and $Y_2Ti_2O_7$) at feature sizes in the range of about 5 nm and above, nominally with near stoichiometric Ti/Y = 0.5 to 1 and (Y+Ti)/O = 0.57 to 0.6 [9-11].

These differences may be partly due to the fact that there is a range of different NF in NFA. Notably, however, APT data also show that even at sizes greater than 10 nm, the Y-Ti-O features are non-stoichiometric, manifesting a significant O and Y deficits and large Fe excesses. The compositions of the larger features are broadly similar to those found in the smaller NF [12]. Further, the SANS magnetic to nuclear scattering (M/N) ratio measurements of the NF that form at typical extrusion conditions of 1150°C are broadly consistent with a mix of oxides [13]. However, SANS data are not consistent with the very high Ti contents found by APT. Note SANS measurements also suggest that the NF that form during the slow ramp-up of consolidation temperatures contain an even smaller fraction of Ti.

Another confounding factor in interpreting these apparently discordant observations about the NF and larger precipitate phases is that the various characterization studies typically involved different NFA. In order to address this issue, we have organized an informal round robin study of a single NFA, MA957, involving different characterization methods and participating institutions. The techniques include TEM, APT, SANS, x-ray absorption fine structure spectroscopy (XAFS) and positron annihilation spectroscopy (PAS). The institutions include UC Santa Barbara (including SANS studies at the National Institute of Standards and Technology), Oxford University, Los Alamos National Laboratory, Leoben University (Austria), UC Berkeley and Illinois Institute of Technology (working at the Argonne National Laboratory Advanced Photon Source). Here we provide only a brief summary of the status of this ongoing collaboration and details will be presented in a future publication. Here we will focus a comparison of APT and TEM studies at UCSB.

Summary of the Status of the MA 957 Round Robin Collaboration

SANS and TEM studies are being carried out at UCSB and the APT measurements at UCSB, Oxford (E. A. Marquis) and Leoben University (E. Stergar and P. Hosemann) [13]. All the techniques are in relatively good agreement regarding the nominal size (d), number density (N) and volume fraction (f) of the NF. Again details will be provided elsewhere, but all the techniques are consistent with nominal average NF parameters of d ≈ 2.6 nm, N ≈ $7x10^{23}/m^3$ and f ≈ 0.7%. Note individual measurements of the NF characteristics varied by up to a factor of 2 or more, and TEM and APT showed that some regions contained few or no NF.

The APT measurements of the average Y, Ti and O solute composition of the small NF less than 5 nm with average Y/Ti/O ≈ 14/41/45 are also very consistent with each other. Measurements of larger features in the range of 5-15 nm are also consistent for the three institutions with average values of Y/Ti/O = 20/32/48. Initial SANS measurements of a French heat of MA957 were consistent with a mix of about 71% $Y_2Ti_2O_7$ and 29% Y_2TiO_5 (or an average Y/Ti/O = 20/17/63) [13] and our more recent unpublished measurements for a US heat of MA957 are consistent with about 55% $YTiO_3$ and 45% Y_2TiO_5 (or an average Y/Ti/O = 22/15/63). The SANS data can only be used to check for the M/N consistency with known phases, and these evaluations are subject to considerable uncertainty, due to factors like use of a Y free alloy as a control and possible incomplete magnetic saturation of the Fe-Cr matrix. Nevertheless, the SANS estimates of Y/Ti > 1 are clearly inconsistent with the much lower values of about 0.34 to 0.63 found in APT studies. The APT, TEM and SANS studies also show the presence of larger oxide and oxynitride features in MA957, like TiO_2 and oxides containing Al, Ti and N, often in complex associated-attached clusters of different phases. As noted previously, the APT generally also suggests that the NF and larger features contain large quantities of Fe and, to a lesser extent, Cr.

Comparison of UCSB APT and TEM Observations

TEM studies in the literature have generally found complex oxides in other NFA that are near stoichiometric compositions, most frequently the pyrochlore phase $Y_2Ti_2O_7$ [9-11]. However, one recent TEM study of MA957 suggested a ratio of Y/Ti < 1 at small NF sizes less than about 10 nm. In order to clarify the structure and composition of the NF and larger features and to make a direct comparison between TEM and APT observations, we have carried out a series of HRTEM lattice imaging observations combined with FFT transform power spectra diffraction patterns to index various features in MA957. We also carried out EDX measurements on these particles. Both bright field and high angle annular dark field (HAADF) where also used to observe the features in MA957 and to characterize their morphology and size distributions. In all cases the particles were extracted from the NFA matrix on thin C replica foils using techniques that will be detailed elsewhere. The TEM was carried out on LaB6 FEA T20 Technai and Titan instruments. The EDX measurements were verified by calibration to bulk oxide phases. Further, HAADF showed that the NF and particles could be extracted down to very small sizes (< 2 nm) and at larger sizes the relatively sharp and sometimes polyhedral particle interfaces indicated that the partial dissolution of any potentially diffuse outer regions of the extracted phases did not occur.

Representative results for a larger particle are illustrated in Figure 1. Figure 1a shows a HRTEM lattice image for a large 30 nm particle and diffraction pattern along with a very similar diffraction pattern from a Crystalkit simulation of orthorhombic Y_2TiO_5. Calculated and measured d-spacings and the corresponding angle between the planes are shown in Table 1. These values are also consistent with Y_2TiO_5, but not with either $Y_2Ti_2O_7$ or $YTiO_3$. A total of 14 particles with sizes greater than 10 nm were indexed in this fashion; a large majority of them were found to be structurally consistent with Y_2TiO_5 oxide. Figure 1b shows another 35 nm particle along with the corresponding EDX spectra yielding a composition of Y/Ti/O = 0.25/0.12/0.63, also consistent with Y_2TiO_5. The particle Y/Ti ratios ranged from ≈ 0.9 to 2.2 (see below), Figure 1c shows a Titan STEM line profile of a ≈ 20 nm particle. Clearly there is no indication of a core-shell type structure, as found in APT studies.

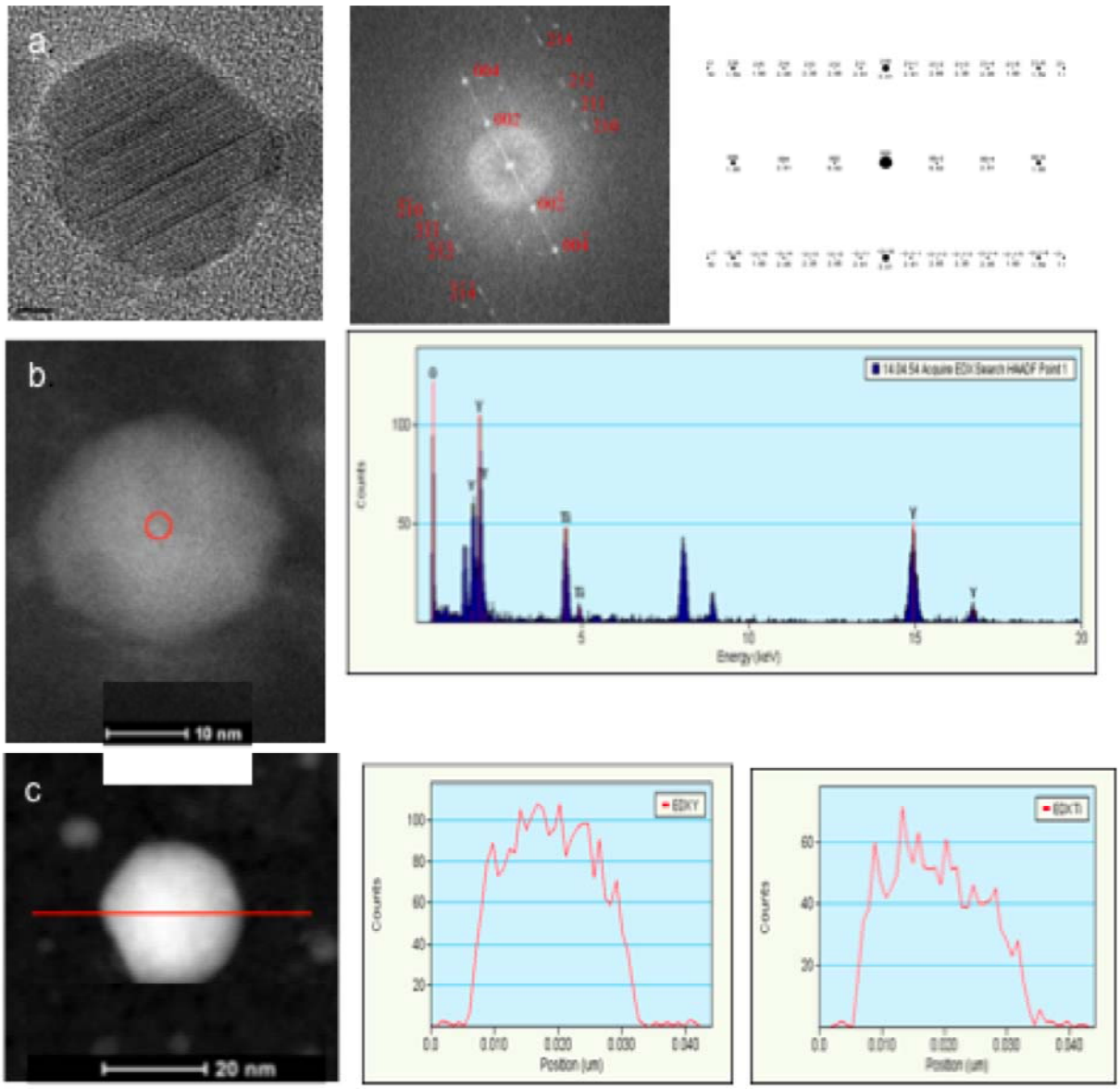

Figure 1 a) A HRTEM image of a large feature and the corresponding derived and simulated diffraction patterns that are consistent with orthorhombic Y2TiO5; b) EDX spectra from a large feature indicating a compositions of Y/Ti/O = 25/12/63 consistent with Y_2TiO_5; c) STEM Ti and Y composition profiles for a large feature that do not show Ti enrichment in an outer shell.

Table 1 Measured and nominal Y_2TiO_5 d-spacings and the corresponding inter-planar angles for the large particle indexed in Figure 1

System	d1 (002)	d2 (210)	interplanar angle
Measured	5.52	3.15	89.8 °
Nominal Y_2TiO_5	5.625	3.21	90.0°

Figure 2a shows the corresponding FFT power spectra for a smaller ≈ 5nm particle that index two d spacings of 3.1Å and 3.0Å with an inter-planar angle of about 73.5°. These values are not consistent with cubic $Y_2Ti_2O_7$, orthorhombic $YTiO_3$ or either hexagonal or orthorhombic Y_2TiO_5. However, indexing was usually more difficult in the smaller feature size range, and it was generally not possible to extract two d-spacings and an inter-planar-angle for low index particle orientations. Figure 2b shows the EDX spectrum for a smaller ≈ 5 nm particle yielding Y/Ti/O = 14/15/71. Figure 2c shows the measured Y/Ti ratios are scattered, ranging from less than 1 to more than 2 and averaging ≈ 1.5. The Y/Ti ratio is not strongly affected by the particle size.

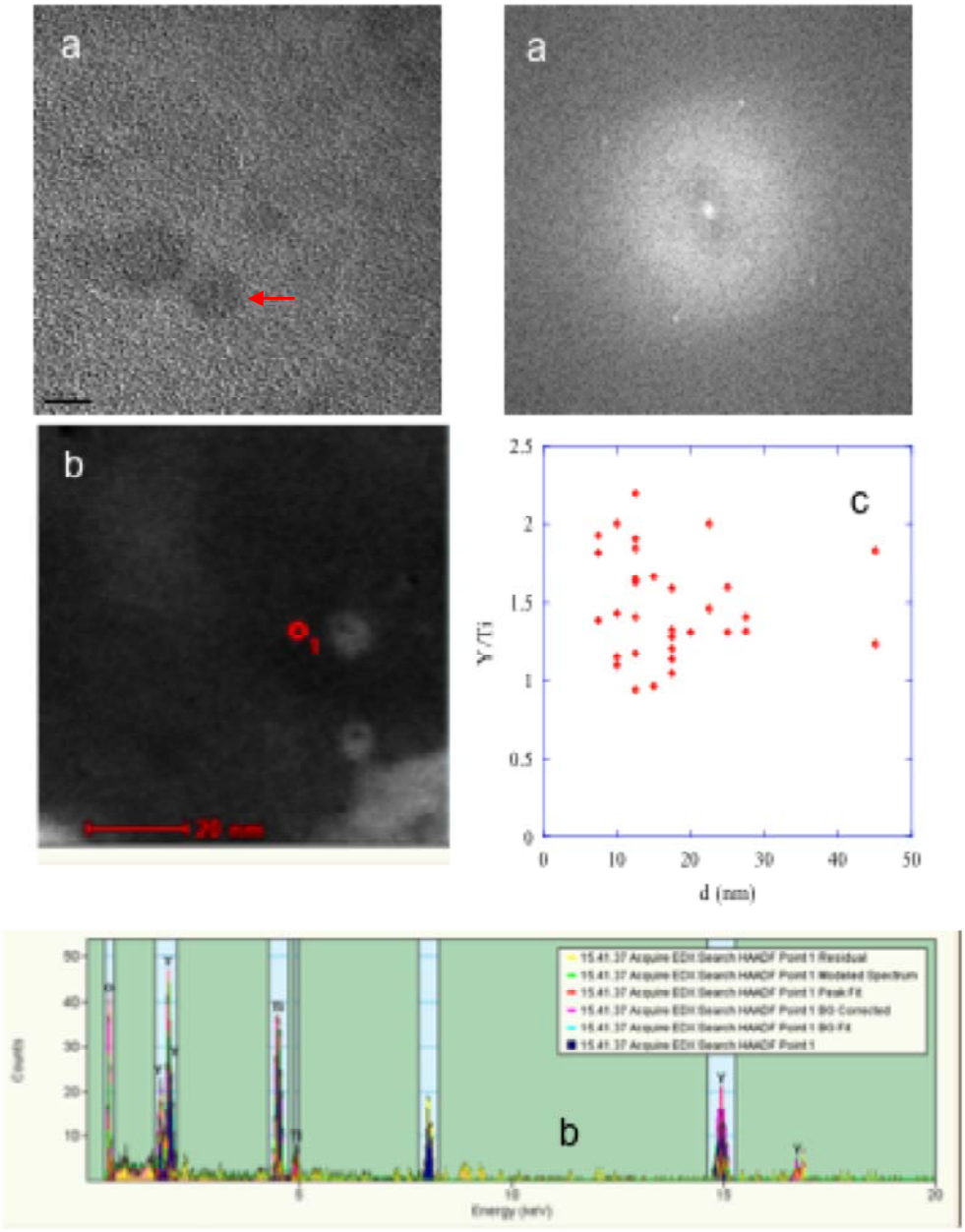

Figure 2 a) A HRTEM lattice image of a small feature and corresponding diffraction pattern; b) the EDX spectrum for a small feature with Y/Ti/O = 14/15/71; c) the observed Y/Ti ratio as a function of average ±2.5 nm binned feature sizes.

Figure 3a summarizes the average composition estimates derived from the various techniques along with the oxide compositions. There is reasonable overall agreement but the APT Y/Ti are not consistent with the results of the other techniques, or the known complex oxide phases. Figure 3b shows a representative HAADF micrograph of the NF and larger features along with the corresponding size distribution. This figure emphasizes that the observation of oxides that are primarily Y_2TiO_5 phases was for features larger than 10 nm and that the oxide-like but typically non-stoichiometric Y/Ti ratio, averaging 1.4, was observed for features generally larger than 5 nm. However, the NF at sizes less than 5 nm have only been probed by SANS and APT techniques with differences that remain to be resolved.

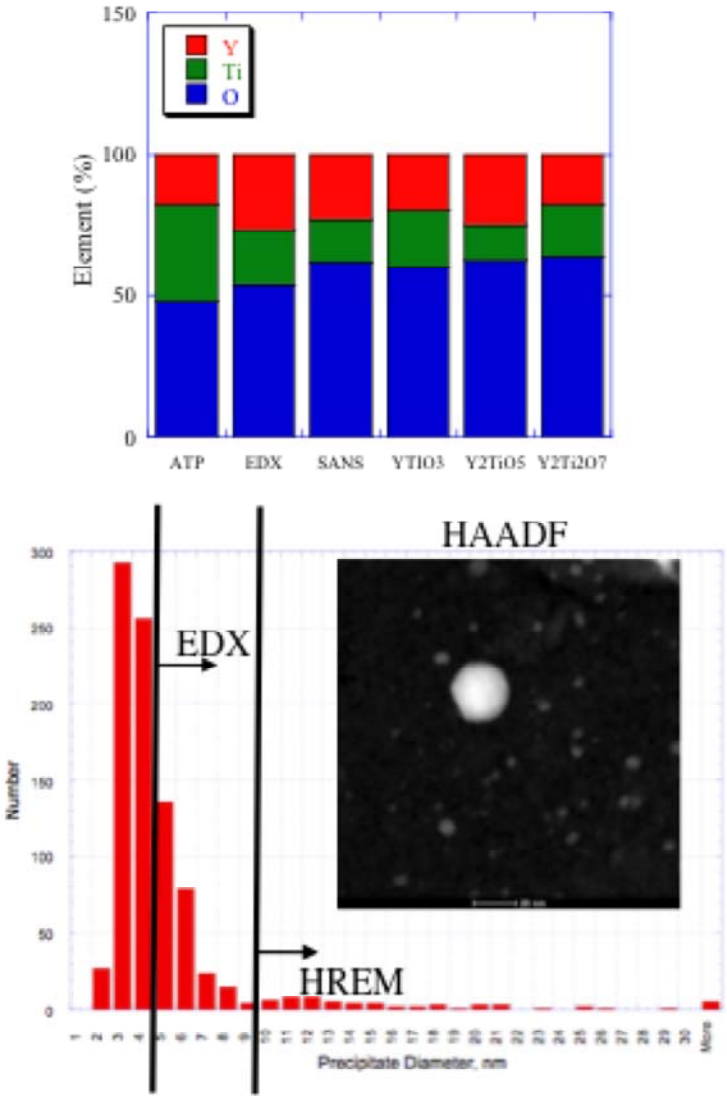

Figure 3 a) Summary of the small feature (NF) composition measured by different techniques compared to those for complex oxides; b) a typical HAADF image of the NF and a larger feature and the corresponding size distribution.

Discussion and Conclusions

First we note that our results are not consistent with the findings of a similar study by Sakasegawa et al [14]. These researchers reported pyrochlore $Y_2Ti_2O_7$ oxides, rather than Y_2TiO_5, and found that the Y/Ti ratio is 0.5 or

less for small NF below about 10 nm. The corresponding compositions measured at larger sizes were 1 to 1.5, slightly below that found in this study.

A major objective of this work was to *directly* compare compositions measured by TEM EDX and APT in larger features. We believe these results clearly show that APT compositions reflect some significant artifacts. First the large quantities of Fe, and to a lesser extent Cr, observed by APT are not supported by the EDX measurements. This conclusion can be qualitatively understood in terms of ion trajectory aberrations in the APT field evaporation process that mixes surrounding matrix atoms with the solutes that are actually in the features [15]. The low Y/Ti and O/(Ti + Y) ratios in APT are also anomalous. Presumably this is also the case for the smaller NF as well. Possible reasons for these APT anomalies are under investigation.

Future Work

The APT, work described above is preliminary and represents ongoing research, including the round robin collaboration on MA957. Current work on MA957 at UCSB includes: a) X-ray diffraction measurements on bulk extractions; b) indexing of the interfaces of both extracted and embedded particles; c) use of energy filtered TEM (EFTEM) to image and characterize the compositions of extracted particles; d) additional PAS and XAFS studies. It is also hoped that TEM energy electron loss spectroscopy (EELS) and anomalous small angle X-ray scattering measurements at the APS will be carried out in the future.

References

1. G. R. Odette, M. J. Alinger, B. D. Wirth, “Recent Developments in Radiation Damage Resistant Steels, Ann. Rev. Mater. Res. 38, (2008) 471.
2. E. A. Marquis, "Core/shell Structures of Oxygen-Rich Nanofeatures in Oxide-Dispersion Strengthened Fe-Cr alloys", Appl. Phys. Lets 93-18 Article Number: 181904 (2008)
3. D.J. Larson, P.J. Maziasz, I-S. Kim and K. Miyahara, “Three-Dimensional Atom Probe Observation of Nanoscale Titanium-Oxygen Clustering in an Oxide-Dispersion-Strengthened Fe-12Cr-3W-0.4Ti + Y_2O_3 Ferritic Alloy”, Scripta Mater. 44 (2001)
4. M. K. Miller, E. A. Kenik, K. F. Russell, L. Heatherly, D. T. Hoelzer and P. J. Maziasz, “Atom Probe Tomography of Nanoscale Particles in ODS Ferritic Alloys”, Mater. Sci. Eng. A 353(2003) 140.
5. M. K. Miller, D. T. Hoelzer, E. A. Kenik, K. F. Russell, " Nanometer scale precipitation in ferritic MA/ODS alloy MA957", J. Nucl. Mat. 329-333 (2004) 338.
6. M. K. Miller, D. T. Hoelzer, E. A. Kenik and K. F. Russell, “Stability of Ferritic MA/ODS Alloys at High Temperatures”, Intermetallics, 133-4(2005) 387.
7. M. K. Miller, K. F. Russell and D. T. Hoelzer, “Characterization of Precipitates in MA/ODS Ferritic Alloys”, J. Nucl, Mat. 351(2006) 261.
8. D. T. Hoelzer, J. Bentley, M. A. Sokolov, et al., "Influence of Particle Dispersions on ohe High-Temperature Strength of Ferritic Alloys", J. Nuc. Mat. 367 (2007) 166
9. S. Yamashita, S. Ohtsuka, N. Akasaka, S.Ukai, and S. Ohnukiy, “Formation of Nanoscale Complex Oxide Particles in Mechanically Alloyed Ferritic Steel”, Phil. Mag. Lett., 84-8 (2004) 525.
10. M. Klimiankou, R. Lindau, A. Moslang. "Energy-Filtered TEM Imaging and EELS Study of ODS Particles and Argon-Filled Cavities in Ferritic-Martensitic Steels", Micron 36-1 (2005) 819.
11. S. Ukai and S. Ohtsuka, "Nano-mesoscopic structure control in 9Cr-ODS ferritic steels", Energy Materials 2 (2007) 26.
12. G. R. Odette, E. A. Marquis, E. Stregar and P. Hosemann, unpublished research
13. M. J. Alinger, G. R. Odette, and D. T. Hoelzer, “On the Role of Alloy Composition and Processing Parameters in Nanocluster Formation and Dispersion Strengthening in Nanostuctured Ferritic Alloys”, Acta Mater. 57 (2009) 392.
14. H. Sasasegawa, L. Chaffron, F. Legendre, et al., " Correlation Between Cemical Composition and Size of Very Small Oxide Particles on MA 957 ODS Ferritic Alloy, J. Nucl, Mat.384 (2009) 115.
15. E. A. Marquis and F. Vurpillot, "Chromatic Aberrations in the Field Evaporation Behavior of Small Precipitates", Microscopy and Microanalysis, 14-6 (2008) 561.

COMPATIBILITY OF MATERIALS EXPOSED TO ISOTHERMAL Pb-Li – B. A. Pint (Oak Ridge National Laboratory, USA)

OBJECTIVE

One proposed U.S. test blanket module (TBM) for ITER uses ferritic-martensitic alloys with both eutectic Pb-Li and He coolants at ~475°C. In order for this blanket concept to operate at higher temperatures (~700°C) for a DEMO-type reactor, several Pb-Li compatibility issues need to be addressed. Some of the issues being currently investigated are the use of corrosion resistant alloys and coatings, the transformation of alumina exposed to PbLi and the effect of impurities on dissolution of these materials.

SUMMARY

Two sets of capsules experiments exposed for 1000h at 500°-700°C were completed to determine the effect of various factors on the amount of dissolution in Pb-Li. The first set examined the effects of Al-rich coatings and the characterization has been completed. Thin coatings exposed at 700°C showed significant Al loss with different variations: (1) pre-oxidation, (2) O gettering and (3) exposure in pure Pb without Li. Less Al loss was observed after exposure at 600°C. A second series of capsules were recently completed that explored the effect of Fe and Ni impurities on the dissolution rate and dissimilar metal reactions between Fe and SiC at 600°C. Based on only the mass gain data, there is some indication of a dissimilar metal effect in Pb-Li.

PROGRESS AND STATUS

Introduction

The current focus of the U.S.fusion energy materials program is to address issues associated with the dual coolant Pb-Li (DCLL) blanket concept[1] for a test blanket module (TBM) for ITER and enhanced concepts for a DEMO-type fusion reactor. A DCLL blanket has both He and eutectic Pb-Li coolants and uses ferritic steel as the structural material with a SiC/SiC composite flow channel insert (FCI). Thus, recent U.S. compatibility research has examined compatibility issues with Pb-Li.[2-6] Unlike Li, where many materials (especially oxides) are dissolved or degraded,[7] a wider range of materials are compatible with Pb-Li because of the low Li activity in eutectic Pb-Li.[8] For example, SiC is readily dissolved by Li[9] but not Pb-Li.[3,4] However, because of higher solubilities, Pb-Li readily dissolves many conventional alloys above 500°C. This is not a concern for a DCLL TBM operating at <500°C, however, a DCLL blanket for a commercial reactor would be more attractive with a higher maximum operating temperature, perhaps >600°C if oxide dispersion strengthened (ODS) ferritic steels[10] were used. Even at 550°C, a recent study of Eurofer 97 (Fe-Cr-W) showed a very high mass transfer rate in flowing Pb-Li.[11] Therefore, preliminary Pb-Li compatibility experiments are being conducted at 500°-800°C in order to investigate several concepts before flowing tests are conducted. Two sets of capsule experiments have been completed to investigate (1) the effectiveness of Al-rich coatings to inhibit dissolution, (2) the effect of Fe and Ni impurities on the amount of dissolution and (3) potential dissimilar material effects between Fe and SiC. Characterization has been completed from the first set but only mass change data is available for the second set of capsules.

Experimental Procedure

Static capsule tests were performed using Mo inner capsules and type 304 stainless steel outer capsules to protect the inner capsule from oxidation. Specimens were held inside the Mo capsule by a Mo wire. For the dissimilar material experiments, the Mo inner capsule was replaced by a carbon steel capsule or

Table 1. Chemical composition using inductively coupled plasma and combustion analysis of the starting Pb and commercial Pb-Li ingots (in ppma except for Li in atomic%).

	Li	Fe	Cr	Ni	Mn	Si	Al	Mo	C	O	N	S
Pb	n.d.	<4	<4	<4	<4	<40	<8	<2	<170	1270	<40	<50
PbLi (UCLA)	14.3%	<30	<70	<30	<30	<120	<60	<40	750	4820	180	<50
PbLi (Atlantic)	19.8%	21	<3	<3	<3	18	<6	<2	2510	4730	<12	<100
PbLi (Atlantic)	21.0%	165	<3	<3	<3	17	<6	<2	2760	14460	<12	<100

a CVD SiC container was included inside the Mo capsule. The specimens were ~1.5 mm thick and 4-5 cm^2 in surface area with a 0.3 μm surface finish. Specimens were aluminized in a laboratory scale chemical vapor deposition (CVD) reactor for 6h at 900°C. Chemical and microstructural details of the coating formed under these conditions are given elsewhere.[12] Pre-oxidations were conducted in dry flowing O_2 for 2h at 800° or 1000°C. The Mo and Fe capsules were loaded with 125g of commercial purity Pb-Li in an argon-filled glove box. The Pb-Li used in these experiments was from a different batch (from Atlantic Metals) than the previous batch (received from UCLA) and the chemistry from two different locations is shown in Table I. There was a distinctly higher Li content in the new batch of Pb-Li. In one capsule, only high purity Pb was added, composition in Table I. Additions to the Pb-Li were made as metal powder during loading. After exposure, residual Pb-Li on the specimen surface was removed by soaking in a 1:1:1 mixture of acetic acid, hydrogen peroxide and ethanol for up to 72 h. Post-test surfaces were initially examined using x-ray diffraction (XRD) and secondary electron microscopy (SEM). The specimens that formed a surface oxide were then coated with copper to protect that layer, sectioned and metallographically polished for analysis by electron microprobe analysis (EPMA).

Results and Discussion

Table 2 summarizes the mass change data from the first series of capsules. Several prior runs are included for comparison noting that a different Pb-Li batch was used for those experiments. Figure 1 summarizes the effect of Al (either as a coating or alloy addition) on the mass loss as a function of capsule temperature from this study and prior work[3-6]. Clearly the presence of Al retards dissolution. However, one concern about the relatively thin CVD coatings is the limited Al reservoir in the coating and the significant Al loss from the coating after only 1kh at 700°C.[13] The four capsule exposures of aluminized T92 specimens were conducted to investigate this loss of Al. Figure 2 shows the specimen exposed at

Table 2. Mass change of specimens after 1000h exposures with a Mo capsule.

Specimen	Pre-oxidation	Temperature	Environment	Mass Change (mg/cm^2)
T92	none	600°C	Pb-Li (Atlantic)	- 1.27
T92 + CVD Al	none	600°C	Pb-Li (Atlantic)	- 0.04
*T92	none	700°C	Pb-Li (UCLA)	- 3.47
*T92 + CVD Al	none	700°C	Pb-Li (UCLA)	- 0.09
T92 + CVD Al	2h at 800°C	700°C	Pb-Li (Atlantic)	0.00
T92 + CVD Al	none	700°C	Pb-Li + 0.18%Zr	0.53
T92 + CVD Al	none	700°C	Pb	0.00
ODS FeCrAl	2h at 1000°C	500°C	Pb-Li (Atlantic)	- 0.11
*ODS FeCrAl	2h at 1000°C	700°C	Pb-Li (UCLA)	- 0.06

* Prior work with different Pb-Li chemistry

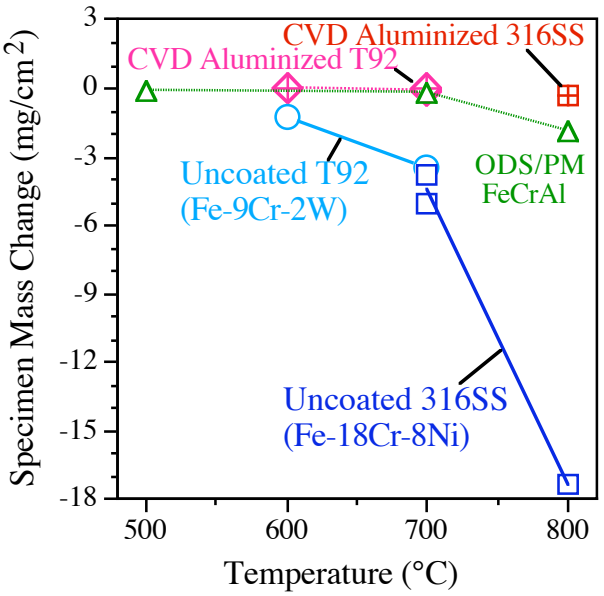

Figure 1. Specimen mass loss as a function of exposure temperature in Pb-Li for 1kh in Mo capsules. Alumina-forming alloys or coatings have much lower mass gains than conventional Fe-base alloys.

600°C. A relatively uniform oxide product was formed. Using XRD, the layer was identified as $LiAlO_2$. Based on the Al profiles in Figure 2b, very little Al was lost during this exposure, likely due to the lower temperature and limited interdiffusion at this temperature.[14]

Figures 3-5 show aluminized T92 specimens under various conditions at 700°C. One hypothesis about the Al loss was that the bare coating rapidly lost Al to the liquid metal before a protective oxide layer was

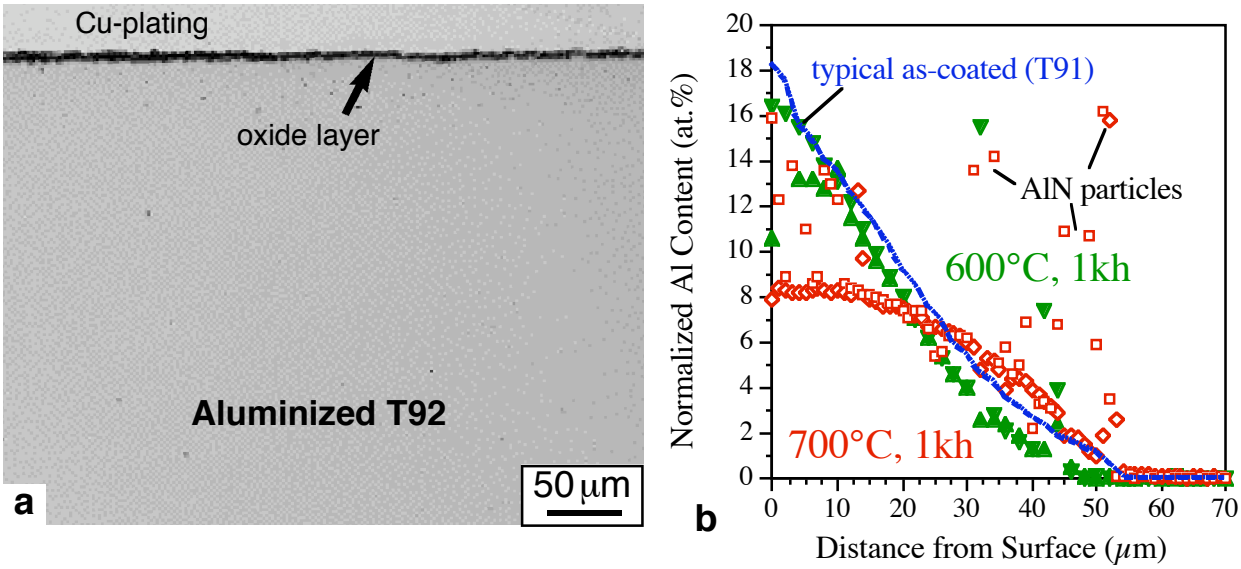

Figure 2. (a) Light microscopy of aluminized T92 polished cross-section after 1kh at 600°C in commercial Pb-Li (b) EPMA composition profiles comparing a typical as-coated Al profile to the Al profile after exposure at 700°C and 600°C.

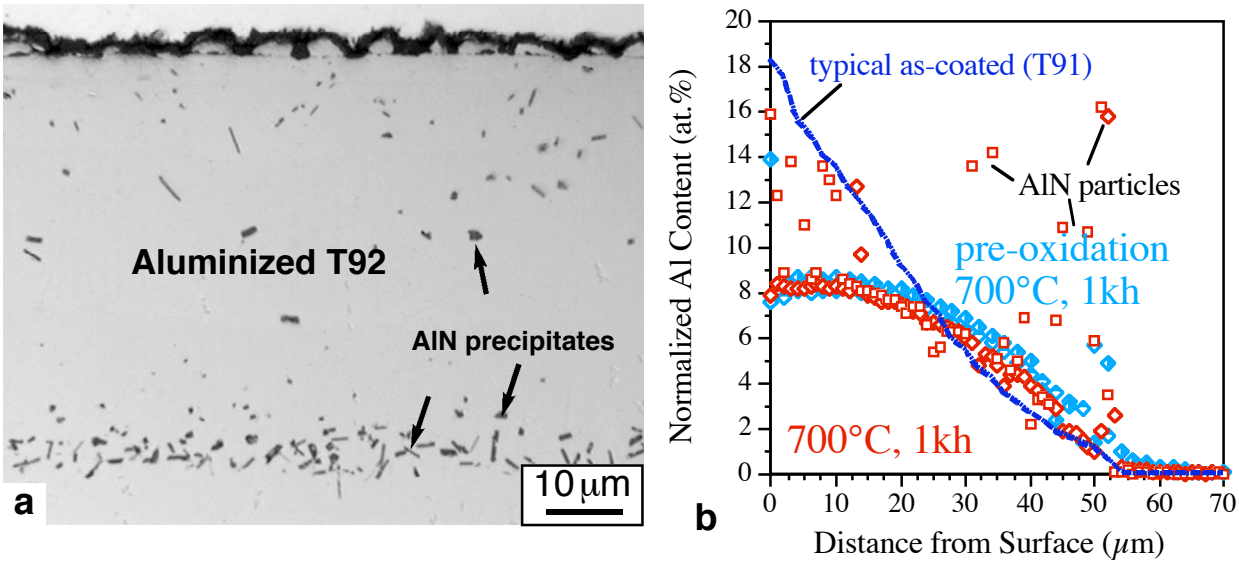

Figure 3. (a) Light microscopy of aluminized and pre-oxidized T92 polished cross-section after 1kh at 700°C in commercial Pb-Li (b) EPMA composition profiles comparing a typical as-coated Al profile to the Al profile after exposure at 700°C with and without pre-oxidation.

formed. Figure 3 shows results for the aluminized T92 specimen that was pre-oxidized for 2h at 800°C prior to exposure. The oxide was also identified by very distinct $LiAlO_2$ XRD peaks, consistent with prior results for pre-oxidized ODS FeCrAl at 700° and 800°C.[5,6] No penetrations of the coating were observed and no mass loss was detected, Table 2, suggesting the pre-oxidized coating was more protective. However, a similar Al depletion was observed as occurred without pre-oxidation, Figure 3b. Some Al was consumed during pre-oxidation but the amount of loss is higher than would be expected from

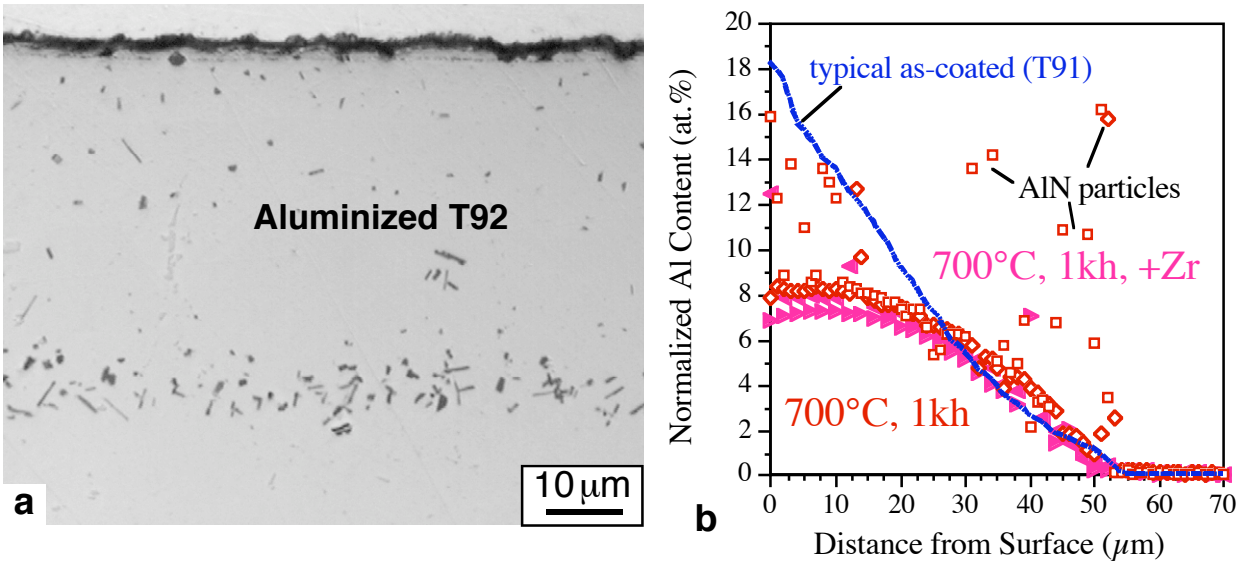

Figure 4. (a) Light microscopy of aluminized T92 polished cross-section after 1kh at 700°C in commercial Pb-Li + Zr (b) EPMA composition profiles comparing a typical as-coated Al profile to the Al profile after exposure at 700°C with and without a Zr addition.

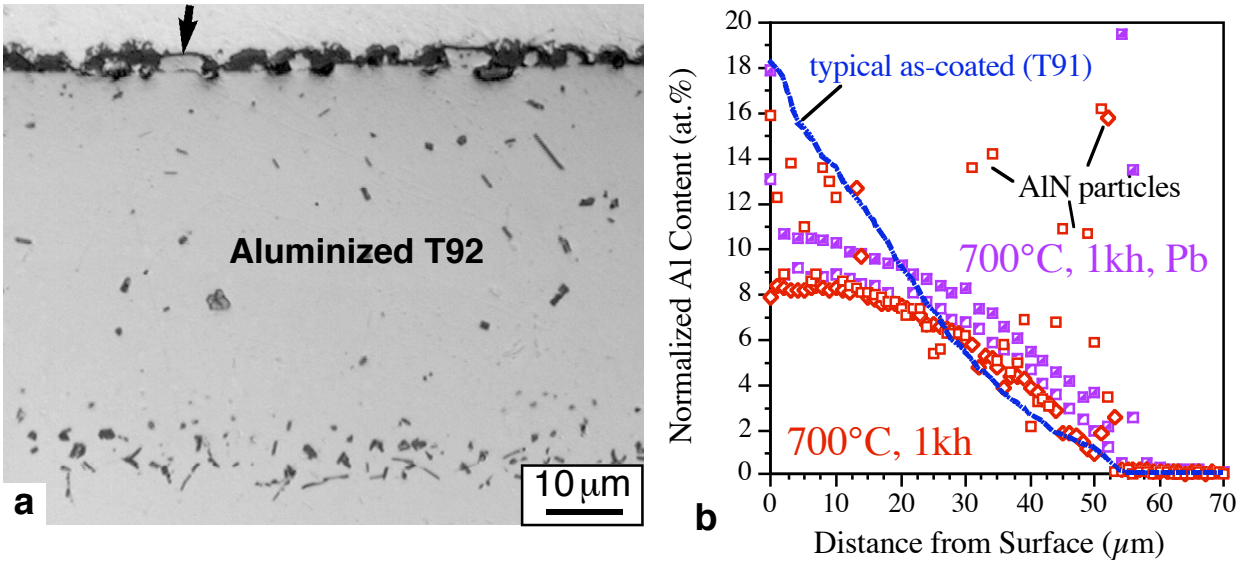

Figure 5. (a) Light microscopy of aluminized T92 polished cross-section after 1kh at 700°C in high purity Pb (b) EPMA composition profiles comparing a typical as-coated Al profile to the Al profile after exposure to Pb and Pb-Li at 700°C. Arrow in (a) shows thin oxide where spallation may have occurred.

the pre-oxidation step. Figure 4 shows the results from the capsule test where 1g of Zr was added to getter O in the Pb-Li. Gettering O could potentially increase the time to form a protective oxide layer. The cross-section appears very similar as Figure 3, the oxide formed was $LiAlO_2$ and the Al loss was slightly higher than the profile without Zr. Finally, Figure 5 shows the aluminized T92 specimen exposed to high purity Pb. The polished corss-section appears similar to the others. However, the outer layer appears rougher and some oxide spallation was evident in SEM examination of the specimen in plan view. The arrow in Figure 5a indicates an area where the oxide is thinner and may have spalled. Without Li present, the oxide was not $LiAlO_2$ but also was not clearly α-Al_2O_3 by XRD. Further characterization is needed of the mixed oxide from this specimen.

The final specimen from this series was pre-oxidized ODS FeCrAl exposed at 500°C. Prior work had shown that the α-Al_2O_3 layer formed after 2h at 1000°C transformed to $LiAlO_2$ after exposure to Pb-Li at 700° or 800°C.[5,6] However, after 1kh at 500°C, $LiAlO_2$ peaks were not evident. Figure 6 shows the uniform oxide product. Additional TEM characterization is needed to identify the oxide phases and microstructure after this exposure.

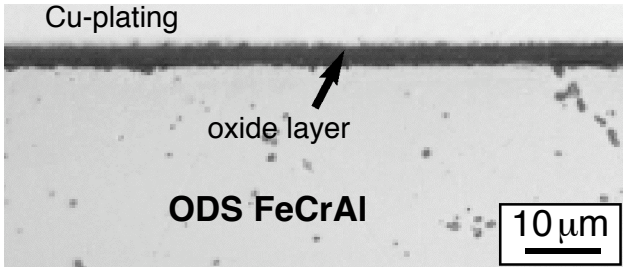

Figure 6. Light microscopy of pre-oxidized ODS FeCrAl (PM2000) polished cross-section after 1kh at 500°C in commercial Pb-Li.

Table 3. Mass change of specimens in second series after 1000h exposures in Pb-17Li

Specimen	Capsule	Temperature	Addition	Mass Change (mg/cm^2)
*316SS	Mo	700°C	none (UCLA)	- 5.06
316SS	Mo	700°C	1000ppma Fe	-11.89
316SS	Mo	700°C	1000ppma Ni	- 9.60
*T92	Mo	700°C	Pb-Li (UCLA)	- 3.47
T92	Mo	700°C	1000ppma Fe	- 6.02
T92	Mo	700°C	1000ppma Ni	- 6.41
CVD SiC	Fe	600°C	none (Atlantic)	- 0.04
Fe	SiC	600°C	none (Atlantic)	- 0.18
Fe	Mo	600°C	none (Atlantic)	- 0.47

* Prior work with different Pb-Li chemistry

A second series of capsules were recently completed and the mass change data after exposure is shown in Table 3. Additions of Fe and Ni were added to simulate Pb-Li contaminated by Fe from dissolution or Ni from stainless steel. The effect of Ni on T92 was investigated for the case of the stainless steel loop described in Ref. 11 which plugged at 550°C. Unfortunately, the change in Pb-Li source (Table 1) appears to have had a significant effect on the mass loss so the baseline Pb-Li exposures for T92 and 316SS without the Fe or Ni addition at 700°C is not a reliable baseline for comparison. Figure 7a summarizes the mass loss data for these exposures. In each case, the dissolution was higher for 316SS compared to T92. Compared to the Fe addition, the Ni addition reduced the mass loss for 316SS, which is expected since Ni is selectively removed from 316SS. By increasing Ni in the Pb-Li, the liquid is closer to saturation which should decrease the amount of mass loss. In contrast, the Ni addition had little effect on the mass loss for T92. Figure 7b summarizes the dissimilar material experiments conducted at 600°C. The 0.04mg/cm^2 mass loss for SiC was higher than observed at 1000°-1200°C using SiC capsules.[3,4] Further

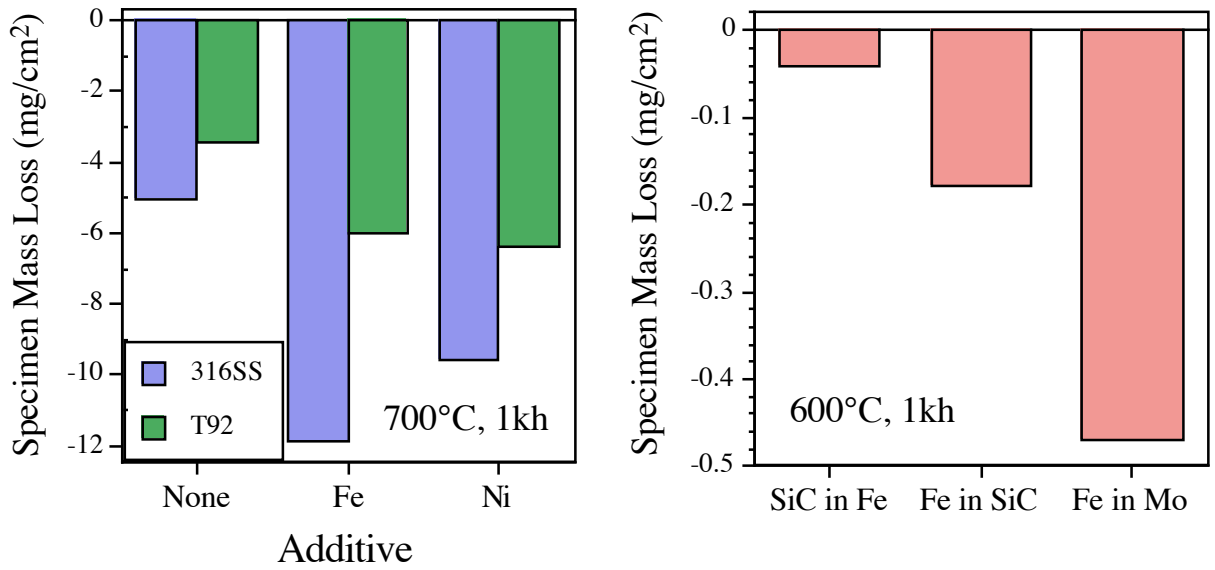

Figure 7. Mass loss results from the second series of capsule experiments exposed for 1kh in Pb-Li, (a) the effect of Fe and Ni additions on the mass loss of 316SS and T92 at 700°C and (b) the dissimilar material effect between Fe and SiC at 600°C.

characterization is needed to determine the extent and uniformity of attack. The mass loss also could be due to the new Pb-Li source, perhaps due to the higher Li content of this Pb-Li, Table 1. For the Fe specimens, the mass loss was lower in the SiC capsule compared to the Mo capsule. A potential C transfer could have occurred in both Fe/SiC capsules because of the higher stability of Fe carbides compared to SiC. Characterization of the Fe specimen should determine if any C transfer occurred.

References

[1] M. Abdou, D. Sze, C. Wong, M. Sawan, A. Ying, N. B. Morley and S. Malang, Fus. Sci. Tech., 47 (2005) 475.
[2] B. A. Pint J. L. Moser and P. F. Tortorelli, Fus. Eng. Des. 81 (2006) 901.
[3] B. A. Pint, J. L. Moser and P. F. Tortorelli, J. Nucl. Mater. 367-370 (2007) 1150.
[4] B. A. Pint, Fus. Sci. Tech. 52 (2007) 829.
[5] B. A. Pint and K. L. More, J. Nucl. Mater. 376 (2008) 108.
[6] B. A. Pint, Mater. Sci. Forum, 595-598 (2008) 549.
[7] J. E. Battles, Intern. Mater. Rev. 34 (1989) 1.
[8] P. Hubberstey, J. Nucl. Mater. 247 (1997) 208.
[9] T. Yoneoka, S. Tanaka and T. Terai, Mater. Trans. 42 (2001) 1019.
[10] S. Ukai and M. Fujiwara, J. Nucl. Mater. 307 (2002) 749.
[11] J. Konys, W. Krauss, J. Novotny, H. Steiner, Z. Voss and O. Wedemeyer, J. Nucl. Mater. 386-88 (2009) 678.
[12] Y. Zhang, B. A. Pint, K. M. Cooley and J. A. Haynes, Surf. Coat. Tech. 202 (2008) 3839.
[13] B. A. Pint, DOE/ER-0313/45 (2008) 61.
[14] Y. Zhang, A. P. Liu and B. A. Pint, Mater. Corr. 58 (2007) 751.

MODELLING THERMODYNAMICS OF ALLOYS FOR FUSION APPLICATION - A. Caro, P. Erhart, M. Serrano de Caro, B. Sadigh (Lawrence Livermore National Laboratory), S.G. Srinivasan (UNT), A. Stukowski (Germany).

OBJECTIVE

This research has two main objectives:

- The development of computational tools to evaluate alloy properties, using the information contained in thermodynamic functions. We aim at improving the ability of classical potentials to account for complex alloy behavior, and
- The application of these tools to predict properties of alloys under irradiation, in particular the FeCr system.

SUMMARY

This semester has been very productive in the developments of both tools and algorithms.

- With the visit of a A. Stukowsky, a graduate student from Prof. K. Albe (Germany) we implemented the formalism of the composition dependent embedded atom model (CD-EAM) into Lammps, a freely distributed code for molecular dynamics. We also implemented a 'variance constrained' Metropolis Monte Carlo, MMC, algorithm into Lammps.
- We developed a modified version of the CD-EAM, that we call 'one site' CD-EAM that significantly improves the performance of a MMC algorithm without affecting the accuracy of the interatomic potential.
- We developed a ternary FeCr-He potential based on data obtained from Prof. K. Nordlund's group in Finland. We validate this potential against *ab initio* data on He in FeCr obtained from within a collaboration with Chu Chun Fu at CEA-Saclay, France.
- We started simulation of He bubbles in FeCr alloys, determining the pressure versus size relation for the 1He/vacancy ratio

BACKGROUND

Our work aims at developing theoretical and numerical methodologies that are directly applicable to multi-scale modeling addressing the specific issues related to multi-component, multi-phase systems in non-equilibrium states, such as solid-solution hardening, point defect-solute interactions, stoichometry effects, static and dynamic strain aging, dislocation-solute interactions, and in general the aspects of microstructure evolution that are affected by irradiation. At its present stage of development, we have been able to predict numerous thermodynamic properties of FeCr mainly related to ordering and precipitation; we have found new intermetallic phases and suggested the existence of a dependence of the solubility limit on the degree of order of the alloy. At present, we are studying dislocation mobility in the solid solution and the heterogeneous phase, and we are developing a new algorithm to perform Monte Carlo simulations inside the miscibility gap, a technique that will allow us to study interfacial energies and nucleation sizes.

We develop a strategy to model radiation damage in FeCr alloys, system in which magnetism introduces an anomaly in the heat of formation of the solid solution that is at the basis of its unique behavior. Magnetism has implications for the precipitation of excess Cr in the *a*' phase in the presence of heterogeneities. These complexities pose many challenges for atomistic (empirical) methods. To address such issues we develop a modified, many-body potential by rigorously fitting thermodynamic properties, including free energy. Multi-million atom displacement Monte Carlo simulations in the transmutation ensemble, using both our new potential and our new MC code, are able to predict properties of non equilibrium processes like heterogeneous precipitation, and dislocation – precipitate interactions, enabling the study of hardening and embrittlement under irradiation.

PROGRESS AND STATUS

In the period covered by this report, we developed a first version of a ternary empirical potential that adds He to the binary FeCr potential we developed a few years ago. We also developed the numerical codes that solve this model both in molecular dynamics and in Metropolis Monte Carlo.

Multicomponent alloy potentials can be build in different ways, depending on the particular scheme adopted for the interactions. Our FeCr binary potential in based on a standard EAM embedding part plus a pair potential that has an extra many body contribution in the form of a polynomial that depends on local composition. This methodology, which is similar to the CALPHAD strategy for binary and multicomponent alloys, is readily generalized to multicomponent systems. For a ternary, what needs to be done is to develop the composition dependent polynomials corresponding to the two new binaries generated when a third element is added to FeCr, namely FeHe and CrHe. These polynomials are closely related to the heats of formation of these new binaries.

Fortunately for us, He is a chemically inert noble gas that does not form alloys or compounds with any other element; its low solubility is a consequence of elastic interactions not compensated by any chemical attraction. As a result, He solubility is very small in both metals, leading to precipitation of He in the form of bubbles. From the modeling perspective then the only parameter that needs to be fitted is the heat of solution of a single impurity, in both host metals, i. e. the equivalent to the derivative of the heat of formation of FeHe and CrHe at vanishing He compositions.

The strategy we followed was to take advantage of a recent development of FeHe and CrHe binary potentials developed by our colleague at Helsinki University, Prof. K. Nordlund, who made these developments available to us before publication.

The properties that are used as target are summarized in Table 1.

Fe-He	Subs.	Octa.	Tetr.
DFT Seletskaia	4.08	4.60	4.37
Fu	4.22	4.57	4.39
This potential:	4.10	4.51	4.39
Cr-He	Subs	Oct.	Tetr.
DFT Norlund:	5.00	5.37	5.20
This potential:	5.01	5.34	5.25

Table 1: Selected properties of substitutional He as obtained form ab initio calculations and by the classical potential

An empirical ternary potential is in fact a collection of six potentials: Fe, Cr, He, FeCr, FeHe, and CrHe. In the process of constructing the ternary potential, we re-fitted the Fe potential from the Mendelev-2003 to the newest version Ackland-2004, which has better self-interstitials and dislocation core properties. In this way, the ternary potential is based on what is considered today the most accurate Fe and Cr potentials.

The potential was also fitted to configurations of relaxed He_N (a-c) and He_NV_1 (d-f) clusters in pure Fe used to fit the potential, as shown in Figure 1. [From K. Nordlund, FI]. The potential has not yet been published, as many more tests are needed to certify its accuracy.

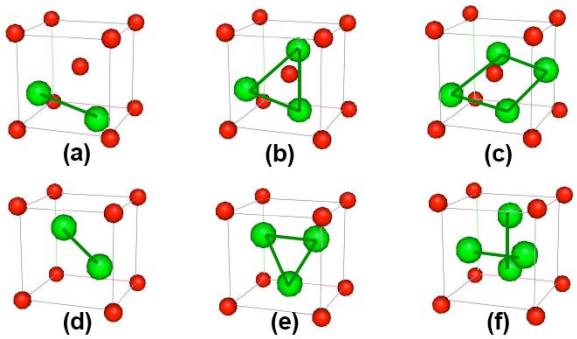

Figure 1: Configurations of relaxed HeN (a-c) and HeNV1 (d-f) clusters in pure Fe

This new ternary potential needs special codes to run. With the visit of A. Stukowski from Darmstadt, Germany, Ph D student of K. Albe, we first incorporated our CD-EAM for FeCr (composition dependent embedded atom model) into Lammps, a free MD code developed at Sandia. We then developed the routines for the ternary alloy. We formulated an improved version of this potential model that is more efficient for large-scale Monte-Carlo and molecular dynamics simulations, while retaining the complexity implicit in its three-body interactions. The paper describing code and this improvement is in press, and it is available upon request to the authors. This code enables the simulation of large alloy systems for which the CD-EAM is the optimal choice. Its performance is reported in Figure 2.

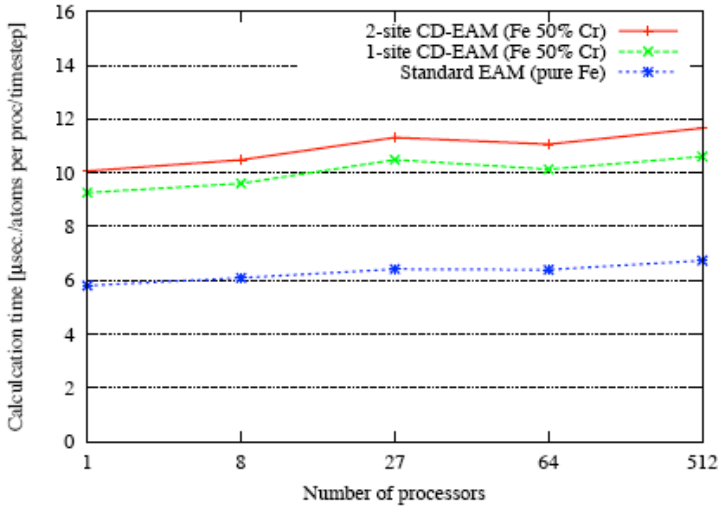

Figure 2: Comparison of the computation times for the CD-EAM models and the standard EAM model in a parallel molecular dynamics simulation. The benchmark simulation consists of a bcc crystal at 300K with 16,000 atoms per processor.

To study precipitation of He into bubbles in single crystals as well as in the presence of heterogeneities such as grain boundaries, free surfaces or dislocations, we also developed a Metropolis Monte Carlo code based on the backbone of LAMMPS. Its first test runs indicate that it is ready to be used.

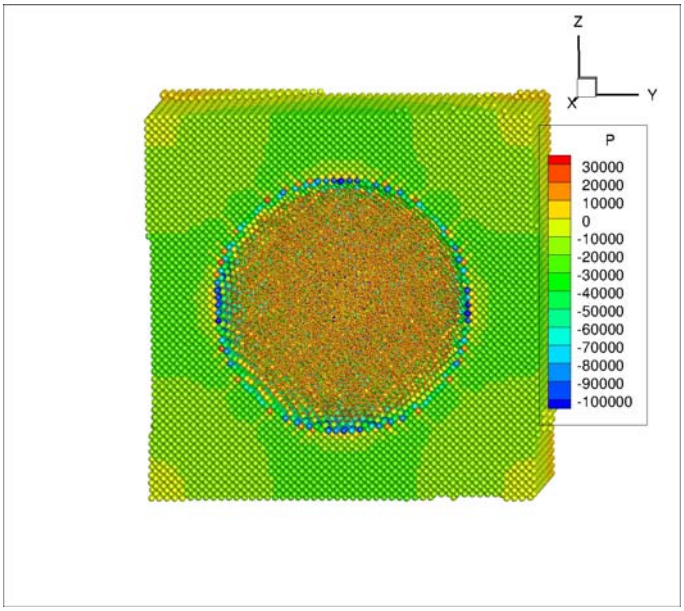

Figure 3: A 4.5 nm He bubble in Fe. The He/vacancy ration is 1. At this density, He is a fluid under compression. Results obtained with the new Md-MC code Lammps and the new FeCr-He interatomic potential.

With the ternary potential and the MD and MC codes, we are starting the study of thermodynamics and kinetic properties of He in FeCr alloys. Figure 3 shows a 4.5 nm radius He bubble in Fe in a pressure color code. He is a fluid under a ~ 2GPa of pressure, while the surrounding matrix shows levels of stress from -10GPa in tension to 3 GPa in compression.

Conclusions

We derived the analytic force expression for the concentration-dependent embedded atom method (CD-EAM) potential and showed that the forces for this advanced many- body model can be calculated in a computationally efficient manner, at a cost which is only slightly larger than for standard EAM potentials. This facilitates the application of the CD-EAM model in large-scale molecular dynamics simulations of concentrated alloys.
The CD-EAM model in its original form is not suitable for Monte-Carlo simulations since its effective pair interaction range is twice as large as the cutoff radius of the potential. By introducing a slight modification of the analytic form of the CD-EAM model it is, however, possible to reduce the effective interaction radius to be equal to the cutoff radius. This renders massively-parallel Monte-Carlo simulation based on the new CD-EAM model possible while preserving all of the qualities of the original CD-EAM model. Energy and force calculation routines for the two-site and the new one-site CD-EAM model have been implemented in the massively-parallel molecular dynamics code LAMMPS [10] and are available upon request from the authors.

Publications

B. Sadigh, P. Erhart, A. Caro, “Heterogeneous nucleation in alloys using MCCask, a parallel Monte Carlo code in the transmutation ensemble with displacements”, in preparation.

A. Caro, D. Farkas, E. M. Bringa, G. Gilmer, and L. A. Zepeda-Ruiz, “Mobility and mechanical response of dirty interfaces in nanocrystalline Cu”, in press.

Alexander Stukowski, Babak Sadigh, Paul Erhart and Alfredo Caro. “Application of the concentration-dependent embedded atom method to large-scale molecular dynamics and Monte-Carlo simulations”, in press.

Vo, NQ; Averback, RS; Bellon, P, and A. Caro. “Yield strength in nanocrystalline Cu during high strain rate deformation”, SCRIPTA MATERIALIA 61, 76 (2009).

Bonny, G; Pasianot, RC; Malerba, L, and A. Caro. “Numerical prediction of thermodynamic properties of iron-chromium alloys using semi-empirical cohesive models: The state of the art”, JOURNAL OF NUCLEAR MATERIALS 385, 268 (2009).

Bonny, G.; Erhart, P.; Caro, A. “The influence of short range order on the thermodynamics of Fe-Cr alloys”. Modelling and Simulation in Materials Science and Engineering 17, 025006 (2009).

MODELING OF POINT DEFECT CLUSTER EVOLUTION UNDER PULSED IRRADIATION

- S.I. Golubov (Oak Ridge National Laboratory, University of Tennessee), R.E. Stoller (Oak Ridge National Laboratory), A.V. Barashev (The University of Liverpool)

OBJECTIVE

Most of the theoretical investigations of damage accumulation in irradiated materials have focused on steady irradiation with little attention paid to pulsed irradiation conditions. However, the problem of pulsed irradiation is quite important when one considers that pulsing is an inherent aspect of current and proposed irradiation facilities such as the MTS (LANL), SNS (ORNL), IFMIF, and ITER. Some theoretical work along this line that has been done in the past predicted essential differences between pulsed and steady irradiations. However exact calculations of damage accumulation under pulsed irradiation have never been done. This work intends to fill this gap.

SUMMARY

The main results of this work are summarized as follows:

- For the first time point defect (PD) cluster nucleation and growth during different pulsed irradiation regimes has been calculated and compared with that of steady irradiation.
- It is found that PD cluster nucleation is extremely sensitive to the type of irradiation: it is enhanced in the case of pulsed irradiation. The effect increases with decrease of pulse frequency.
- Rate of damage accumulation under pulsed irradiation is larger at small doses and smaller at high doses than that for steady irradiation.
- The calculation results obtained suggest that the pulse structure of MTS and IFMIF may reproduce damage accumulation quite close to that one may expect for steady irradiation whereas it may be very different in the case of SNS irradiation.
- The new method for numerical integration of the Master Equation used provides a valuable tool to link experimental data obtained using different types of irradiations.

PROGRESS AND STATUS

I. Introduction

Nucleation, growth and coarsening of point defect clusters or secondary phase precipitates are responsible for numerous changes that occur in the physical and mechanical properties of materials during irradiation. Thus, it is important to develop a fundamental understanding of material behaviour under pulsed irradiation conditions, and the differences between this and the steady irradiation characteristic of fission reactors in which a substantial amount of irradiation data has been obtained. It is also important to evaluate the influence of pulsed irradiation vis-à-vis steady irradiation to determine the validity of data obtained from pulsed sources.

Computational modelling can provide the required critical evaluation. In the late seventies and early eighties work was done to elucidate the impact of pulsed irradiation on microstructure evolution in comparison to that of steady irradiation [1-4]. It was shown that there is quite a large difference in

microstructure evolution between the two types of irradiation, however the calculations were only done for very low doses. In this work we report the results for modelling of nucleation and growth of voids in the dose range up to 0.1 dpa.

A detailed cluster dynamics model based on the mean field rate theory has been employed to investigate the influence of pulsed irradiation on void evolution. The material response to pulsed and continuous irradiation conditions has been characterized using a new numerical method for solving the kinetic equations describing point defect cluster dynamics.

II. Model description

In this work we consider a particular case, namely void formation from vacancies in a pure metal under irradiation with the following assumptions.

1. Primary damage is produced in the form of Frenkel pairs, which are single vacancies and self-interstitial atoms (SIAs).
2. The point defects execute a three-dimensional random walk.
3. The nucleation of vacancy clusters (voids) proceeds via a homogeneous mechanism that is due to vacancy + vacancy reactions.
4. The vacancy clusters are immobile.

These assumptions, however, are only used for simplification and do not lead to any restrictions in the applicability of the analysis presented below.

Within the framework described above, we can write the following Master Equation (ME) for the size distribution of voids (SDF), *f(x,t)* where x is the number of vacancies in a void

$$\frac{\partial f(x,t)}{\partial t} = J(x-1,t) - J(x,t) \tag{1}$$

In Eq. (1) *J (x,t)* is the flux of clusters in space of cluster size:

$$J(x,t) = P(x,t)f(x,t) - Q(x+1,t)f(x+1,t), \tag{2}$$

where *P(x,t)* is the rate of vacancy absorption by a cluster of size x and *Q(x,t)* is the sum of corresponding rates of SIA absorption and vacancy emission from the void. These rates depend on the concentration of the cluster and diffusion properties of the mobile defects. For three-dimensional diffusing point defects they take the following form:

$$\begin{aligned} P(x) &= wx^{1/3} D_v C_v(t), \\ Q(x) &= wx^{1/3}\left[D_i C_i + D_v \exp\left(-E_v^b(x)/kT\right)\right] = Q^i(x) + Q^v(x), \end{aligned} \tag{3}$$

where, $w = (48\pi^2/\Omega^2)^{1/3}$, $C_v(t), C_i(t)$ and $D_v, C_v(t), C_i(t) D_i$ are the concentrations and diffusion coefficients of vacancies (subscript v) and SIAs (subscript i), respectively; $E_v^b(x)$ is the binding energy of a vacancy with a void of size x, k_B is the Boltzmann constant, T is the absolute temperature and Ω is the atomic volume.

In order to complete the system of equations describing void evolution, we must add equations for the evolution of the point-defect concentrations, C_v and C_i, which are given by (see e.g. [5])

$$\begin{aligned}\frac{dC_v(t)}{dt} &= G(t) - \mu_R D_i C_i(t) C_v(t) - D_v(C_v - C_{v0}) Z_v k_v^2 - 2P(1) f(1,t) \\ &\quad +2Q_v(2) f(2,t) + Q_i(2) f(2,t) \\ &\quad -\sum_{x=1}^{x=\infty} \left(P(x) f(x,t) - Q_v(x+1) f(x+1,t) \right), \\ \frac{dC_i(t)}{dt} &= G(t) - \mu_R D_i C_i(t) C_v(t) - D_i C_i Z_i k_i^2 - \sum_{x=1}^{x=\infty} Q_i(x) f(x,t),\end{aligned} \tag{4}$$

where G(t) is the point defect generation rate, μ_R is the recombination constant, and k_v^2 and k_i^2 are the sink strengths of crystal defects (excluding that of voids) for vacancies and SIAs, respectively. Note that the terms containing *P(x)* and *Q(x)* in Eqs. (4) are consistent with those in Eqs. (2) and (3).

The initial and boundary conditions are taken to have the following form:

$$\begin{aligned} &f(x, t=0) = C_{v0}\delta(x-1), \\ &C_v(t=0) = C_{v0}, \\ &C_i(t=0) = 0, \\ \\ &f(x=1,t) = C_v(t), \\ &f(x=\infty,t) = 0. \end{aligned} \tag{5}$$

where C_{v0} is the thermal equilibrium vacancy concentration. Eqs. (1) - (4) are a set of coupled nonlinear equations and, in the general case, can be solved using numerical methods only.

The main problem in such calculations arises due to the large number of equations to be solved since ME (1) represents a set of equations describing evolution of each size void. To overcome the problem several methods on numerical integration of the above equations have been suggested. A grouping method, first suggested by Kiritani, provided an idea as to how the number of equations may be substantially reduced. A grouping developed by Golubov et al. [6], which provides the most accurate grouping method, is employed here. The method is based on an approximation of the SDF by a linear function within a group of sizes

$$f_i(x) = L_0^i \left(x - \langle x \rangle_i \right) + L_1^i. \tag{6}$$

The clusters are grouped within of a group of widths $\Delta x_i = x_i - x_{i-1}$ which include the clusters of the sizes

$$x = x_{i-1} + k, \ \left(k = 1, .., \Delta x_i \right), \tag{7}$$

where the subscript i indicates the number of a group. Thus each group consists of $n_i = \Delta x_i$ numbers of different sizes. It can be shown that the mean sizes of clusters within an *i* group, $< x >_i$, are equal to

$$< x >_i = x_i - \frac{1}{2} \left(\Delta x_i - 1 \right). \tag{8}$$

Note that in a case when $\Delta x_i = 1$ the mean size is equal to $< x_i >= x_i$. It was shown [5] that the equations for the coefficients L_0^i and L_1^i has the following form

$$\frac{dL_0^i}{dt} = \frac{1}{\Delta x_i}\left[J(x_{i-1}) - J_x(x_i)\right],$$
$$\frac{dL_1^i}{dt} = -\left(\frac{\Delta x_i - 1}{2\sigma_i^2 \Delta x_i}\right)\left\{ J_x(x_{i-1}) + J(x_i) - 2J(< x_i > -\frac{1}{2}) \right\}. \quad (9)$$

where σ_i^2 is dispersions of cluster sizes in the group, which are given by

$$\sigma_i^2 = \frac{1}{\Delta x_i}\left[\sum_{\alpha=x_{i-1}+1}^{x_i} \alpha^2 - \frac{1}{\Delta x_i}\left(\sum_{\alpha=x_{i-1}+1}^{x_i} \alpha \right)^2 \right] \quad (10)$$

Note that the grouping procedure is usually applied for large clusters (i.e. x >>1) when it becomes more practical to replace, with adequate accuracy, the sums in equation (10) by corresponding integrals. In this case, equation (10) is reduced to $\sigma_i^2 = \left(\Delta x_i\right)^2 / 12$.

Eqs. (9) describe the evolution of the SDF with the group approximation. These equations satisfy the conservation laws for the number of voids and the number of vacancies in voids. Note that Eqs. (9) are identical to equation (1) in the limiting case when $\Delta x_i = 1$. Because of this there is no problem in describing the SDF in the region between the ungrouped and grouped clusters.

III. Pulse structure and irradiation and material parameters.

Pulsed irradiation used for the analysis is taken in a form schematically presented in Fig. 1.

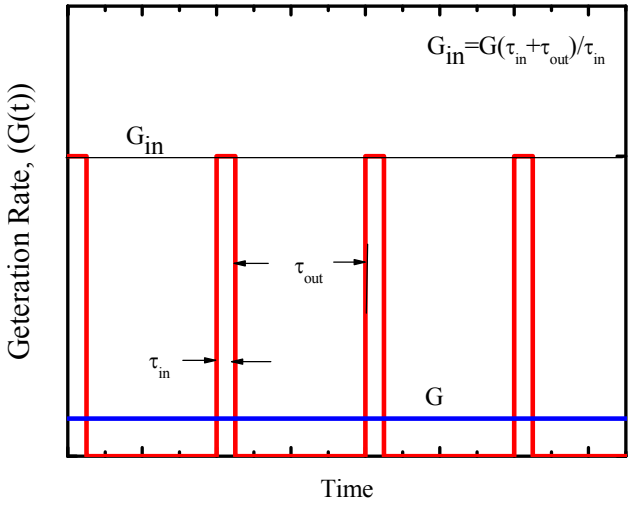

Fig. 1. Pulsed irradiation schematic. τ_{in} and τ_{out} are the duration of a pulse and time between the pulses; G_{in} and G are the rate of point defect generation in the pulse regime and that in the equivalent steady irradiation.

Essential parameters of a pulsed irradiation are the duration of pulses, τ_{in}, and the frequency, ω, which is determined as follows

$$\omega = \left(\frac{1}{\tau_{in} + \tau_{out}} \right)_{|\tau_{out}/\tau_{in} >> 1} \approx \frac{1}{\tau_{out}}. \qquad (11)$$

In this work the calculations have been done for steady irradiation and two pulsed irradiations with τ_{in}=7.5x10^{-4} s and the frequency given in Table 2. Material and irradiation parameters are presented in Table 2.

Table 1. Pulsed Irradiation characterization.

τ_{out}/τ_{in}	ω (Hz)
100	13.20
1000	0.132

Table 2. Material and irradiation parameters used in calculations.

Atomic volume, Ω	1.189×10^{-29} m^3
Recombination coefficient	1.0×10^{21} m^{-2}
Vacancy diffusion coefficient: Preexponent, Migration energy,	 5.0×10^{-5} m^2/s 0.90 eV
SIA diffusion coefficient: Preexponent, Migration energy,	 1.0×10^{-6} m^2/s 0.25 eV
Capture efficiencies of dislocations for vacancies and SIAs	1.0, 1.04
Dislocation density, ρ_d	1×10^{14} m^{-2}
Temperature, T	473 to 673 K
Displacement rate, *G*	1.0×10^{-6} dpa/s
Terminal irradiation dose	0.1 dpa

IV. Results of Calculations

The calculated results for the case of the steady irradiations are shown in Fig. 2 - 4. As can be seen from Figs. 2 swelling obeys a typical behaviour for the case of homogeneous nucleation: the density of voids is very high at low temperature and goes down very fast with temperature increase. Consequently, temperature dependence of swelling (see inset plot in Fig. 2a) shows a maximum at temperature about 623 K and rapidly decreases with temperature increase.

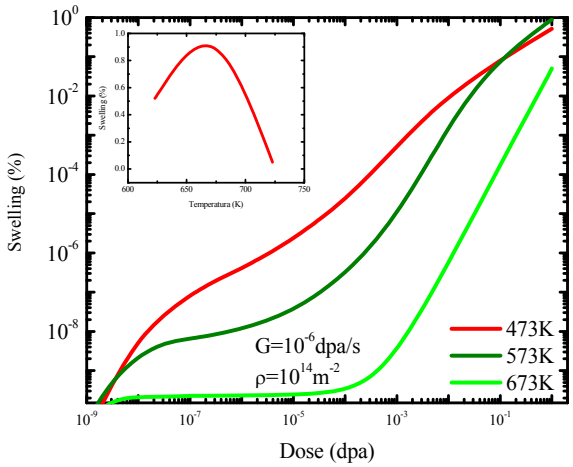

Fig. 2a. Dose dependence of swelling at different temperatures.

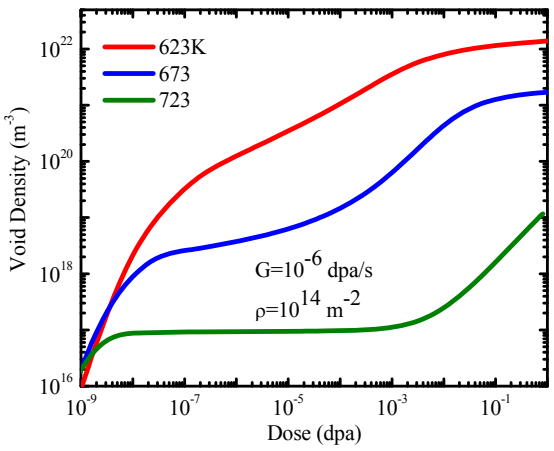

Fig. 2b. Dose dependence of void density at different temperatures.

The dose dependence of the point defect concentrations and mean diameter of voids are presented in Figs. 3. The SDFs of voids at the terminal dose of 0.1 dpa are presented in Fig. 3. As can be seen from Fig. 3a, PD concentrations decrease with dose increases after reaching maximums at temperatures 623 and 673 K. In contrast, they do not practically depend on the irradiation dose at T=723 K because the sink strength of voids at all doses is much smaller that that of dislocations (see Fig. 5). Note that a shape of SDF at this temperature obeys a typical behaviour for a regime when continuous void nucleation takes place at constant nucleation rate (see [6]).

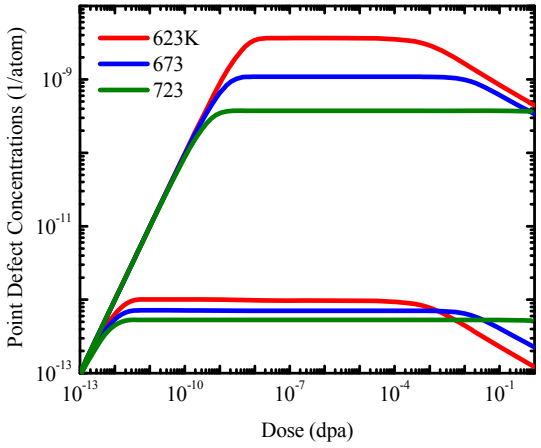

Fig. 3a. Dose dependence of point defect concentrations at different irradiation temperatures.

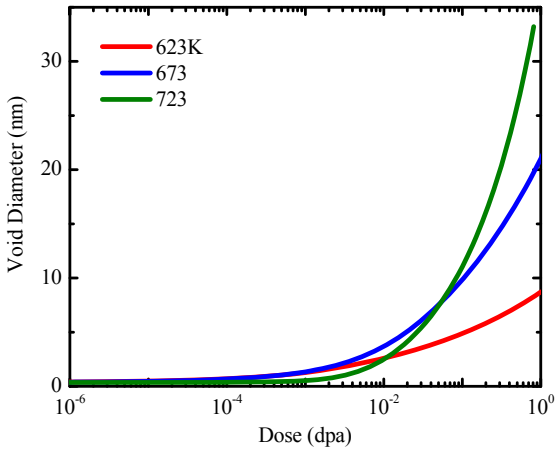

Fig. 3b. Dose dependence of mean diameter of voids at different irradiation temperatures.

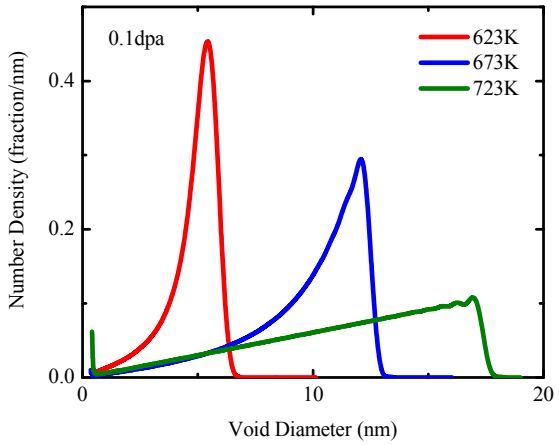

Fig. 4. Size distribution functions at the terminal dose of 0.1 dpa.

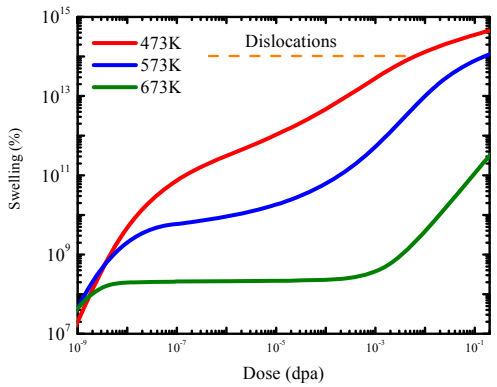

Fig. 5. Dose dependence of sink strengths of voids at different temperatures.

Pulsed irradiation

The calculations in this case are more time consuming in comparison with that of the steady irradiation since the time step for numerical integration, Δt, of the ME has to be extremely small. Indeed, it is quite obvious that the magnitude of Δt has to be smaller than the pulse duration, $\Delta t < \tau_{in}$, otherwise the pulse irradiation structure would be lost. Our calculations show that in fact it has to be much smaller, i.e. smaller by at least one order of magnitude. Moreover it is very sensitive to the shape of a pulse. The pulse shape presented in Fig. 1 requires the time step to be smaller than τ_{in} by about two orders of magnitudes. The time step may be larger in the case when the pulse shape is not so abrupt. In our calculations the pulse shape is taken in the form of a Gaussian

$$G(t) \sim \frac{G_{in}}{\sqrt{2\pi}\tau_{in}} \exp\left(-\left(\frac{t-n\tau_{out}}{\tau_{in}}\right)^2\right), \qquad n\tau_{out} - \alpha\tau_{in} \le t \le n\tau_{out} + \alpha\tau_{in}, \tag{12}$$

where the integer number n is the pulse number; a parameter α is a number equal to 2 to 3 used to make the pulse form smoother. It has been found that for pulse duration of 7.5×10^{-4} second an appropriate time step may be chosen to be equal to 10^{-5} second. Indeed, as can be seen in Fig. 6 further decrease of the time step does not practically affect the void SDF.

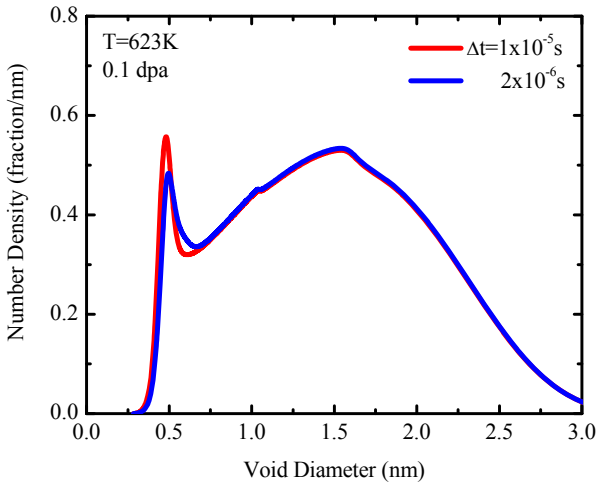

Fig. 6. Terminal size distribution function of voids calculated using two different time steps, 10^{-5} and $2x10^{-6}$ second.

Because the calculations in the case of pulsed irradiation are very time consuming they have been carried out for the case corresponding the maximum in swelling, i.e. for irradiation temperature equal to 673 K, only. The dose dependence of PD concentration calculated for the cases of ω=13.2 and 0.132 Hz are presented on Figs. 7. As can be seen from the plots the variation of PD concentration with the irradiation dose is quite different compared to the steady irradiation.

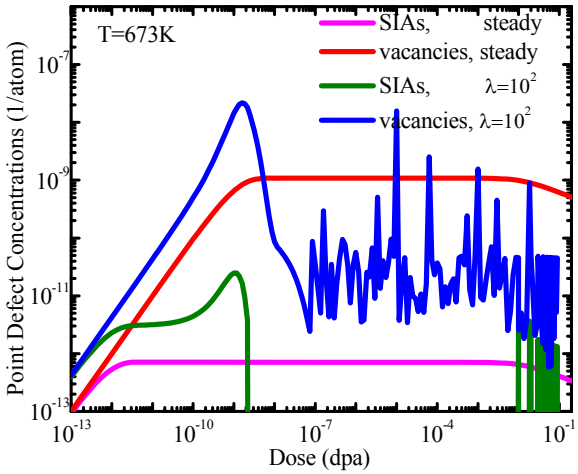

Fig. 7a. Dose dependence of PD concentration calculated for ω=13.2 Hz.

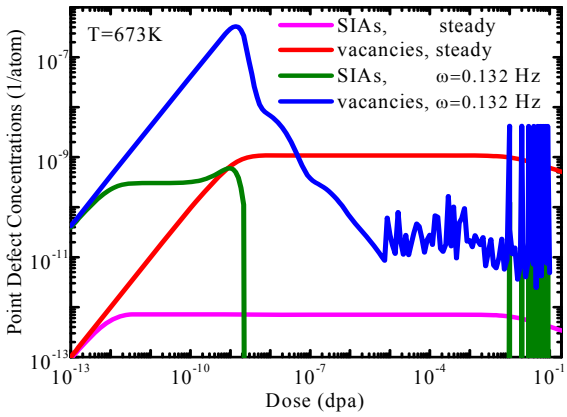

Fig. 7b. Dose dependence of PD concentration calculated for ω=0.132 Hz.

As can be seen the vacancy and SIA concentrations show very large fluctuation with dose and are much higher than those for the corresponding steady irradiation. Note that the SIA concentration is practically zero most the time due to their fast diffusion.

The dose dependence of the void number density and the number of vacancies accumulated in voids are presented in Figs. 8. In accordance with the much higher vacancy concentration in the case of the pulsed irradiation, the void density in this case is much higher as well. It leads to a much higher level swelling at relatively small doses. However this tendency is reversed at higher doses: the rate of swelling

accumulation under pulsed irradiation becomes smaller than that of steady irradiation with the effect much more pronounce in the case the low frequency, ω=0.132 Hz. The reason may be understood from a comparison of the SDFs for those three cases presented in Fig. 9. Indeed as can be seen from Fig. 9a the striking difference between the case of ω=0.132 Hz and other cases is an appearance of an extra peak at small sizes (see more detailed shape of the SDFs in Fig. 9b). It is probably the reason for swelling decrease under pulse irradiation because this group of small voids, which are unstable, competes with the stable ones. Some support for this explanation is given below.

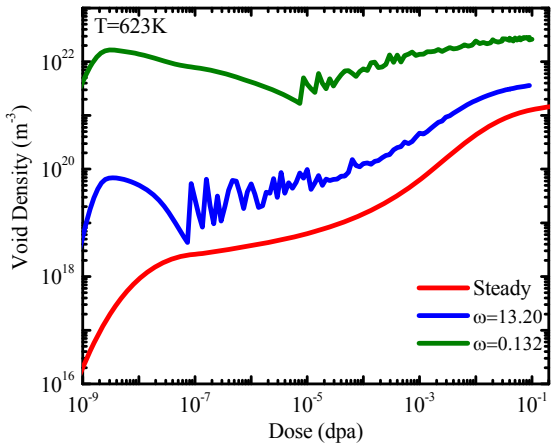

Fig. 8a. Dose dependence of void density calculated for ω=13.2 Hz.

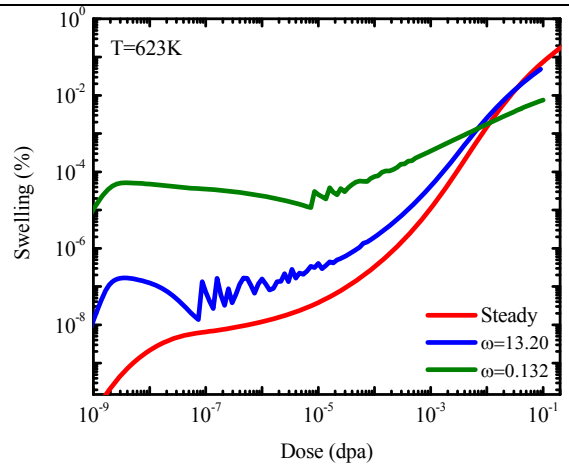

Fig. 8b. Dose dependence of swelling calculated for ω=0.132 Hz.

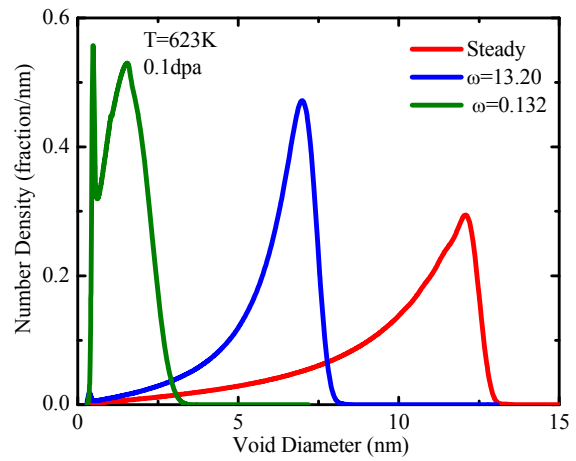

Fig. 9a. Terminal size distribution functions of voids calculated for steady and pulse irradiations.

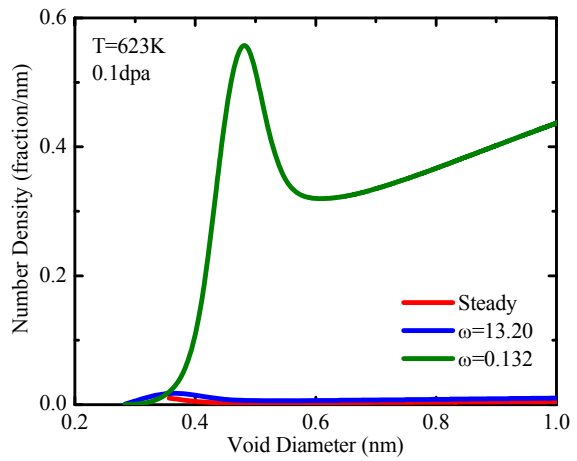

Fig. 9b. The same as Fig.9 in the range of sizes up to 1 nm.

In order to elucidate the point an extra calculation has been done for the case ω=0.132 Hz when the recombination constant is taken to be zero. This case has been considered with an aim to exclude the mutual recombination between vacancies and SIAs that helps to narrow down the number of mechanisms responsible for the effect. The dose dependence of PD concentrations and swelling for the

case together with that when the recombination is taken into account are presented in Figs. 10. As can be seen from Fig. 10a the PD concentrations are higher in the case of "no recombination". The magnitude of swelling at low doses is also higher than that when recombination is taken into account. However the swelling rate at the higher doses is strongly decreased. Comparison of SDFs for those two cases presented in Fig. 11 shows that the fraction of small unstable voids in the case of "no recombination" is higher than that for the case with recombination. Because in the case of "no recombination" the only mechanism involved in the void evolution is a partitioning of point defects between voids and dislocations, one may conclude that the unstable small voids are really responsible for the swelling decrease under the pulsed irradiation.

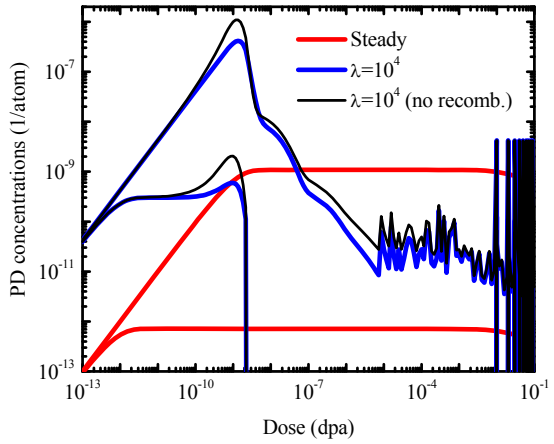

Fig. 10a. Dose dependence of PD concentration calculated with and without recombination for ω=0.132 Hz.

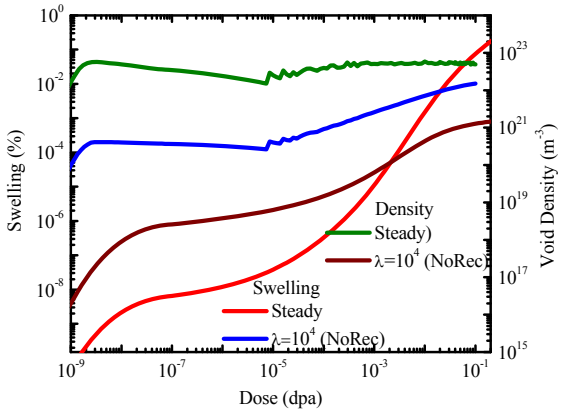

Fig. 10b. Dose dependence of swelling calculated with and without recombination for ω=0.132 Hz.

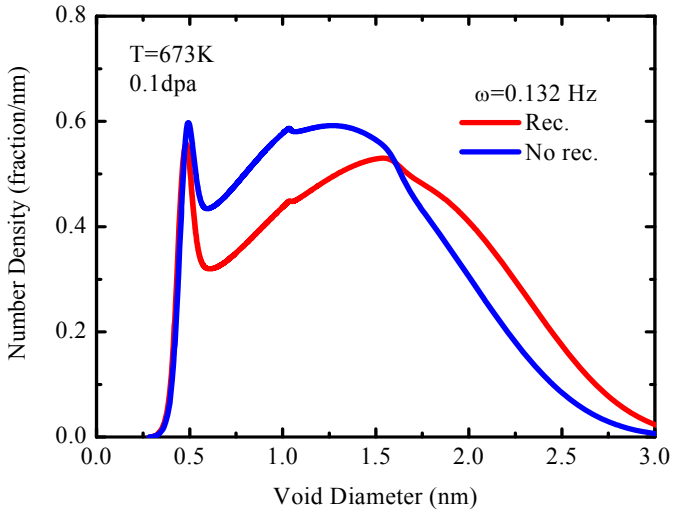

Fig. 11. Terminal size distribution functions of voids calculated for the pulsed irradiation calculated with and without recombination (ω=0.132 Hz).

The same conclusion results from comparing the dose dependence of void swelling calculated in the case of steady irradiation with that which can be calculated analytically for the case of the pulsed irradiation. Indeed it is very well established that in the case without recombination the swelling rate is given by

$$\frac{dS}{d(Gt)} = \frac{Z_i - Z_v}{Z_v} \frac{k_v^2 \rho}{\left(k_v^2 + \rho\right)^2}, \tag{13}$$

where k_v^2 is the sink strength of voids. Since the dose dependence of k_v^2 in the case "no recombination" is calculated, the swelling rate given by Eq. (13) can be compared with those calculated for the cases of steady irradiation and "no recombination". Such a comparison is shown in Fig. 12. As can be seen from the plot Eq. (13) does not provide a correct description of the case under consideration.

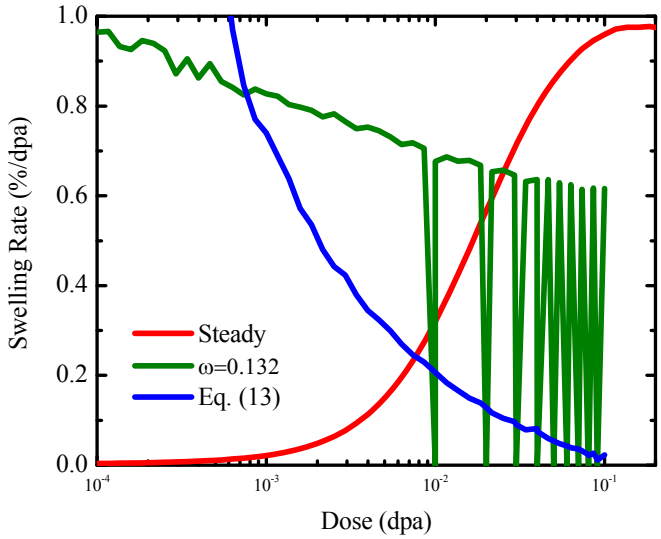

Fig. 12. Dose dependence of swelling rate calculated with and without recombination for ω=0.132 Hz.

V. Conclusions

The calculations presented in this work revealed that the damage accumulation in the form of voids under pulsed irradiation may be qualitatively different compared to that taking place under steady irradiation with the same average rate of PD generation. It is shown that in the case considered here the void density is orders of magnitude higher that that of the steady irradiation and the swelling rate is dramatically decreased at high enough doses. Moreover, it is shown that the damage accumulation cannot be explained by using the ordinary mean size approximation widely used for the case of steady irradiation. In the other words, the numerical integration of ME is the only method which can provide an appropriate description of the damage accumulation under pulsed irradiation.

ACKNOWLEDGEMENTS

The research was sponsored by a research grant from the Office of Fusion Energy Sciences U.S. Department of Energy, under contract DE-AC05-00OR22725 with UT-Battelle, LLC.

References

[1] N.M. Ghoniem and G.L. Kulcinski, J. Nucl. Mater. 69&70 (1978) 816.
[2] N.M. Ghoniem, J. Nucl. Mater. 89 (1980) 359.
[3] N.M. Ghoniem and H. Gurol, Radiation Effects 55 (1981) 209.
[4] E.P. Simonen, N.M. Ghoniem and N.H. Packan, J. Nucl. Mater. 122&123 (1984) 391.
[5] Golubov, S. I., Fiz. Metall. Metalloved., 52 **(**1981) 780 (Engl. transl., *Phys. Metals Metallogr. (USSR),* **52** (1981) 86).
[5] S.I. Golubov, A.M. Ovcharenko, A.V. Barashev, and B.N. Singh, Philos. Mag. A 81 (2001) 643.

ATOMISTIC STUDIES OF PROPERTIES OF HELIUM IN BCC IRON USING THE NEW HE–FE POTENTIAL—David M. Stewart, Stanislav Golubov (Oak Ridge National Laboratory and the University of Tennessee), Yuri Ostesky, Roger E. Stoller, Tatiana Seletskaia, and Paul Kamenski (Oak Ridge National Laboratory)

SUMMARY

In fusion applications, helium caused by transmutation plays an important role in the response of RAFM steels to neutron radiation damage. We have performed atomistic simulations using a new 3-body Fe–He inter-atomic potential combined with the Ackland iron potential. With the ORNL potential, interstitial helium is very mobile and coalesces together to form interstitial clusters. We have investigated the mobility of these clusters. If the He cluster is sufficiently large the cluster can push out an Fe interstitial, creating a Frenkel pair. The resulting helium-vacancy cluster is not mobile. The ejected SIA is mobile, but is weakly trapped by the He–V cluster. If more helium atoms join the He–V cluster, more Fe interstitials can be pushed out, and they combine to form an interstitial dislocation loop. The reverse process is also studied. Multiple helium atoms can be trapped in a single vacancy, and if there are few enough, the vacancy can recombine with an Fe interstitial to create a helium interstitial cluster. These mechanisms are investigated together in larger simulations that examine the nucleation of He defects. Results are compared based on temperature, interatomic potentials used and helium concentration. Helium bubbles of sizes 1-6nm are also studied.

PROGRESS AND STATUS

Introduction

Helium produced in neutron irradiated iron plays an important part in its mechanical properties. The growth, migration and coalescence behavior of helium bubbles is very sensitive to the properties of individual He interstitials and helium-vacancy clusters [1]. A new He–Fe inter-atomic potential has been developed at ORNL, based on extensive fitting to first-principles calculations of point defects and clusters [2–5]. This potential has been used to investigate the properties of helium and helium-vacancy clusters in MD and MS simulations.

Helium diffuses very fast in the matrix, but is easily trapped in vacancies [6]. It is possible for a self-interstitial to recombine with the vacancy, kicking the helium back into an interstitial position. Previous calculations [5] showed that recombination is possible not only for a single substitutional He, but even when the vacancy contains multiple Helium atoms. If the vacancy contains 5 or less atoms, it is found to be energetically favorable for it to recombine with the SIA to form a helium interstitial cluster. For 6–8 atoms there is no clear winner, and for more than 8 it is more favorable for the SIA to be trapped close to a He–V cluster without recombining with it.

A dynamic simulation of a He_8 interstitial cluster at 600K showed that the reverse process (i.e. Frenkel pair formation) can happen—an iron atom is pushed out of its lattice site, creating a He_8V cluster and an SIA. The SIA was trapped beside the cluster.

Simulation Method

The general procedure followed is: Generate perfect BCC lattice. Introduce the defect(s) to be studied. Relax at constant volume using a mixture of conjugate gradient and simulated annealing, and save the atom positions in units of the lattice constant. Start the MD simulation.

The MD simulations used NVE dynamics. The lattice constant and initial velocities were chosen to give close to zero pressure and the desired initial temperature. The boundary conditions are periodic in *X*, *Y* and *Z*, which are ⟨100⟩ directions. The velocity Verlet algorithm with a timestep of 0.3fs is used. As volume and temperature correction are not used, when processes that release energy are simulated the temperature and pressure both rise during the simulation.

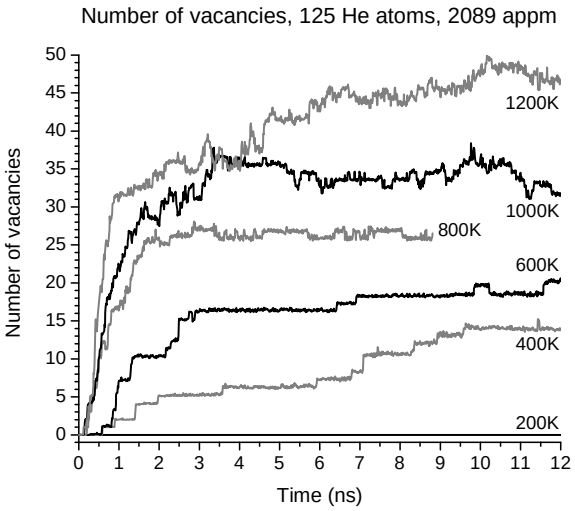

Figure 1. Vacancy production

Coalescence

The dynamic simulations described in the previous semiannual [5] that were run with 125 helium atoms in a 31×31×31 BCC iron matrix (60,000 iron atoms) were continued and the same trends continued. At 200K, the helium slowly and inexorably coalesced until it formed interstitial clusters too big to be mobile, up to a maximum of He_8 with no vacancies or SIAs. At 400K, an SIA is ejected when a cluster reaches 8 or 9 helium atoms, and no SIAs escaped their HeV cluster. At higher temperatures, smaller clusters like He_2 and He_3 were short lived; those that did form grew bigger since the number of available He atoms was fixed. The higher the temperature, the less He atoms were needed to eject an SIA, and the easier the SIAs escape, to be captured by larger clusters with SIAs. The number of vacancies is plotted as a function of time in Fig. 1. This is Fig. 1 in [5] extended with new data.

The simulations run with different potential combinations were also continued, shown in Fig. 2. (Fig. 3 from [5] extended). With Ackland + Wilson, Frenkel pairs formed much faster than with the ORNL potential, because an SIA can be ejected from an interstitial cluster of only 2 or 3 Heliums. The Mendelev + ORNL and Finnis-Sinclair + ORNL, and Mendelev + Juslin–Nordlund [10] combinations were all similar and formed bubbles at a rate and quantity that was between the other two combinations. For Ackland + Juslin–Nordlund [10] showed no clustering so is not plotted. The 976 appm simulations using a box of 40×40×40 were also continued, and the 600K run is shown in Fig. 3 (Fig. 4 from [5] extended). The bubbles took longer to form with the lower concentration, but the number and size distribution was similar.

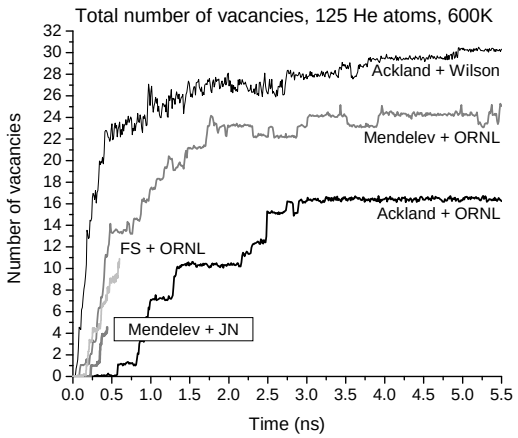

Figure 2. Coalescence for different potentials.

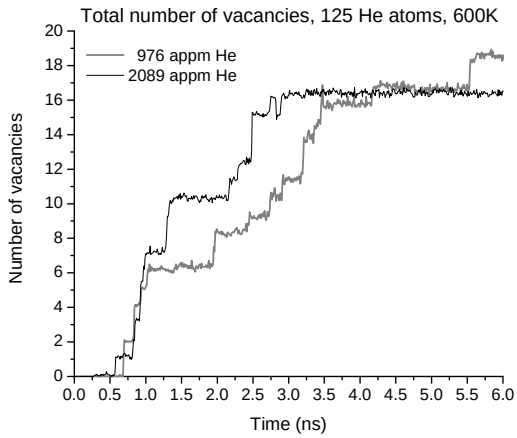

Figure 3. Coalescence for different box sizes.

Cluster Diffusion

The rate of diffusion of helium interstitial clusters was investigated in the previous semiannual [5] for three iron matrix potentials with the ORNL potential and the Wilson potential.

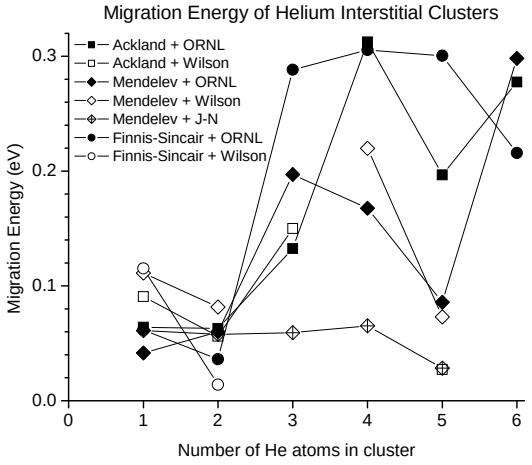

Figure 4. Migration energy results.

Here we add the Mendelev potential in combination with the Juslin-Nordlund potential. The energy barriers calculated from Arrhenius fits are added to the plot of energy barriers (Fig.6 in [5]), in Fig. 4. The Mendelev matrix with the Juslin–Nordlund potential showed consistently low barriers compared to the other combinations. The Juslin–Nordlund He–Fe potential with either of the other two matrix potentials predicts that all clusters will dissociate into individual interstitial Helium atoms, so there are no cluster diffusion rates for them.

Helium bubbles

The He–V defects nucleated in the coalescence simulation are nascent bubbles. We have also simulated larger ones. Bubbles of diameters of 1, 2, 4 and 6 nm were investigated. They consist of Helium atoms in a spherical void containing 59, 339, 2741 or 9577 vacancies respectively. Figure 5 shows a cross-section of a 4nm (2741 vacancy) bubble with a helium to vacancy ratio of one half.

The simulations used the Ackland Iron, the ORNL He–Fe, and the Aziz helium potentials. It was discovered that the helium stays a distance inside the bubble, leading to empty space between the He and the surface iron atoms. The gap was large enough that in these simulations our Fe–He potential is effectively a pair potential. The He atoms rarely come close enough to an iron atom to invoke the 3-body component of our potential, which has a range of 2.2Å.

Figure 6 shows the radial density function of a 2nm bubble with a He/V ratio of 0.49. The squares show the Iron atoms that make up the surface of the bubble. The circles represent the density of helium atoms in the space. The helium density oscillates enough to suggest a shell structure to the arrangement of atoms, but not enough to suggest solid helium. The dotted line in the figure, an approximation to a uniform distribution, shows that the actual helium density (1.04) is just over double the nominal density (0.49). The helium occupies a sphere of radius 7.7Å (just under half the volume of the void), and the gap is approximately 2.2Å.

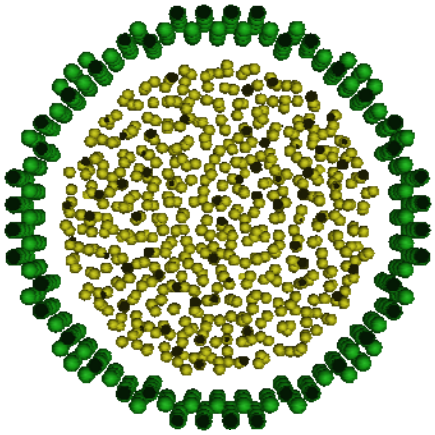

Figure 5. 4nm 0.5He/V bubble at 100K.

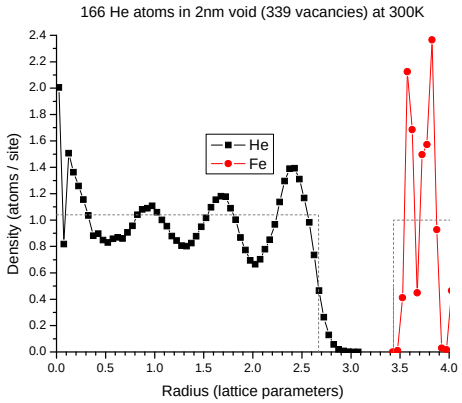

Figure 6. RDF of 2nm equilibrium bubble at 300K.

In a void, the surface matrix atoms move inwards slightly, reducing the volume of the void. At higher temperatures, they move in more. Adding helium to the void pushes the atoms outwards, increasing the volume slightly. The more helium added, the further the bubble expands. There is a point where this balances and the bubble is neither expanded nor contracted; the surface atoms are at the same place as they would be in a perfect lattice. We use this point as our condition for equilibrium. The equilibrium He/V ratio is temperature and size dependant. In general, the equilibrium He/V ratio is lower for higher temperatures and larger bubbles.

Figure 7 shows the dilation of a 2nm diameter bubble as a function of He/V ratio for different temperatures. The equilibrium ratio for each temperature can be determined by where it crosses the horizontal zero line. At 2nm, the curves for the different temperatures are close together; for larger bubbles, the curves spread out more (not shown).

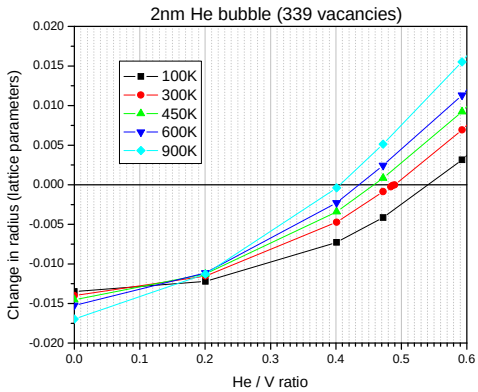

Figure 7. Dilation of 2nm bubbles with T.

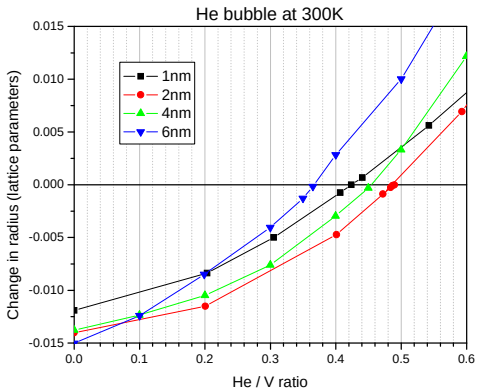

Figure 8. Dilation of different bubbles at 300K.

Increasing the temperature causes a void to shrink, but a bubble to grow. The higher the helium density the bigger this effect is. There is a crossover point where the bubble is relatively independent of temperature. This happens at lower densities than equilibrium, so the bubble is smaller than at equilibrium. The bigger the bubble the lower the He density this occurs at. In Figure 7, this can be seen where the lines almost come together at about 0.15He/V.

Figure 8 shows the dilation of different sized bubbles as a function of He/V ratio at 300K. They show equilibrium at smaller ratios as size increases, except for the 1nm bubble.

The bubble volume is defined by the position of the surface atoms. The volume actually occupied by helium is defined by the He atom positions, and is substantially smaller. Thus there are 2 ways to define helium density and helium pressure, depending on which volume is used. These are plotted in Figures 9 and 10 respectively. The squares show quantities calculated using the former definition; the circles the latter definition. As the smallest bubbles cram the helium into a tiny fraction of the space, the choice of which volume to use makes a huge difference. Note in Figure 11 that the helium density in non-monotonic if the entire bubble volume is used (as it was in the calculations in Figure 8).

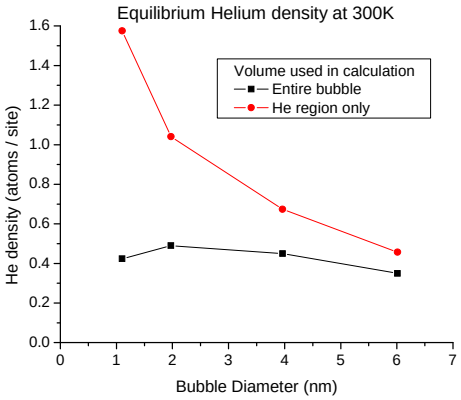

Figure 9. Eq. He Density of bubbles at 300K.

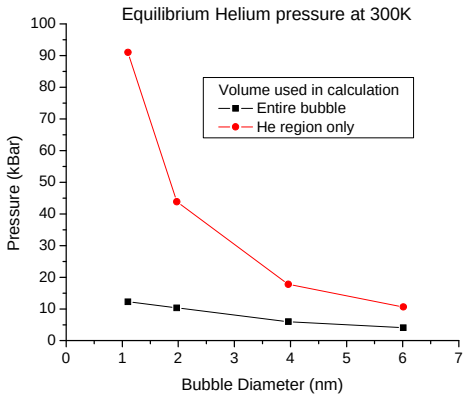

Figure 10. Eq. He Pressure of bubbles at 300K.

Effect of facets

Different crystallographic orientations have different surface energies, which is likely to affect the relationship between temperature, pressure and He/V ratio. In order to determine the effect of different crystallographic surfaces, simulations are being run with three different shaped Helium bubbles (in addition to the spherical ones).

Each void has a volume similar to the 339-vacancy 2nm spherical void. The volumes are different because each shape can only have an integer number of 'shells' of vacancies. The 1.5nm cubical void, which consists of only {100} surfaces, has 341 vacancies. The 2.5nm rhombic dodecahedral void (only {110} surfaces) has 369 vacancies. The 2.9nm octahedral void (only {111} surfaces) has 391 vacancies. Cross-sections of them are pictured in Figure 11.

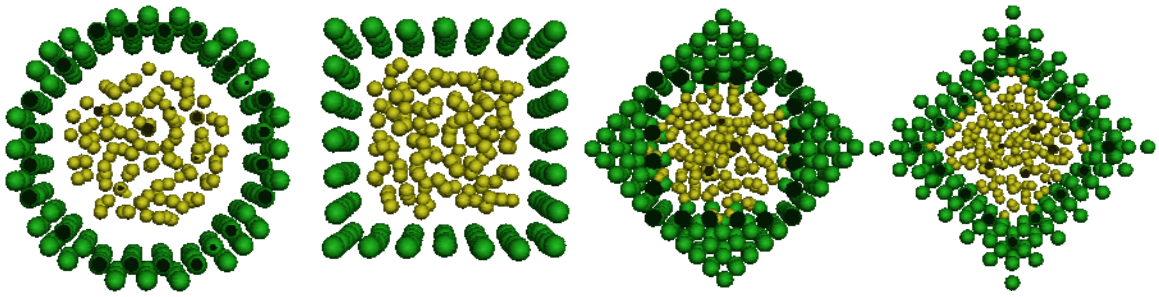

Sphere
All surfaces

Cube
{100} surfaces

Rhombic dodecahedron
{110} surfaces

Octahedron
{111} surfaces

Figure 11. The four different shapes of void being simulated. All 0.4He/V at 300K.

References

[1] S.I. Golubov, R.E. Stoller, S.J. Zinkle, and A.M. Ovcharenko, Kinetics of coarsening of helium bubbles during implantation and post-implantation annealing, Journal of Nuclear Materials 361 (2007), pp. 149–159.

[2] T. Seletskaia, Y.N. Osetsky, R.E. Stoller, and G.M. Stocks, Magnetic Interactions Influence the Properties of Helium Defects in Iron, Physical Review Letters 94 (2005), pp. 046403.

[3] T. Seletskaia, Y.N. Osetsky, R.E. Stoller, and G.M. Stocks, Calculation of helium defect clustering properties in iron using a multi-scale approach, Journal of Nuclear Materials 351 (2006), pp. 109–118.

[4] T. Seletskaia, Y.N. Osetsky, R.E. Stoller, and G.M. Stocks, Development of a Fe He interatomic potential based on electronic structure calculations, Journal of Nuclear Materials 367 (2007), pp. 355–360.

[5] D.M. Stewart, last semiannual report

[6] H. Trinkaus and B. Singh, Helium accumulation in metals during irradiation–where do we stand? Journal of Nuclear Materials 323 (2003), pp. 229–242.

[7] G.J. Ackland, D.J. Bacon, A.F. Calder, and T. Harry, Computer simulation of point defect properties in dilute Fe-Cu alloy using a many-body interatomic potential, Philosophical Magazine A-Physics of Condensed Matter Structure Defects and Mechanical Properties 75 (1997), pp. 713–732.

[8] M.I. Mendelev, S. Han, D.J. Srolovitz, G.J. Ackland, D.Y. Sun, and M. Asta, Development of new interatomic potentials appropriate for crystalline and liquid iron, Philosophical Magazine 83 (2003), pp. 3977–3994.

[9] W. Wilson and R. Johnson, Rare Gases in Metals, Interatomic Potentials and Simulation of Lattice Defects, Battelle Institute Materials Science Colloquia, 1972, 375-390 (1972).

[10] K. Nordlund and S. Dudarev, Interatomic potentials for simulating radiation damage effects in metals, Comptes rendus-Physique (2008).

[11] M.W. Finnis and J.E. Sinclair, A simple empirical N-body potential for transition metals, Phil. Mag. A 50 (1984), pp. 45–55.

HARDENING DUE TO HE-FILLED BUBBLES IN IRON – Yu. N. Osetskiy, R. E. Stoller and D. Stewart (Oak Ridge National Laboratory)

OBJECTIVE

This work has as an objective to understand the state of He-filled bubbles in Fe and their effect on the mechanical properties of irradiated Fe.

SUMMARY

Gas-filled bubble strengthening is an important radiation effect observed in structural materials subjected to high dose irradiation at moderate temperature. The usual treatment of this effect is based on the continuum approach to estimate the equilibrium state of gas bubbles and simplified estimation of their strengthening on the basis of line tension models. We suggest employing multi-scale computer modeling to investigate such effects. This includes low level Density Functional Theory (DFT) calculations to construct an empirical potential for interatomic interactions in Metal-Gas system. Such calculations need up to a few hundred atoms and their free electrons. Next level includes Molecular Dynamics (MD) technique to investigate the equilibrium state of gas filled bubbles as a function of their size and ambient temperature. The scale covered at this level includes bubble of size up to 10nm in matrix crystals of up to 2-4x10^6 atoms. Finally, MD modeling of interactions between moving dislocations and gas-filled bubbles is the largest scale in this approach considering up to 10^8 atoms modeled over a few nanosecond simulated time. This cutting edge research has started at ORNL and will demand significant computational and intellectual resources over the next few next years. We present here the first few results of a multi-scale study of He-bubbles in Fe obtained during FY 2009.

PROGRESS AND STATUS

Atomic-scale model

To study Fe-He system at atomic scale a set of three interatomic potentials (IAPs) is necessary to describe interactions between matrix atoms (Fe-Fe), between He atoms inside bubbles (He-He) and also Fe-He interactions. The Fe-He potential recently developed at ORNL within the Fusion Materials Program was employed here [1, 2]. This potential describes three-body interactions between Fe and He atoms and was fitted to DFT data on forces and energies of different defect including He-vacancy clusters. In the present research IAPs for He-He and Fe-Fe are taken from refs. [3] and [4] respectively.

The above IAPs are used in molecular dynamics (MD) and statics (MS) modeling of He-filled bubbles in Fe. Surface energy of voids was estimated by modeling voids at zero temperature by MS. Crystals of up to 2x10^6 atoms were relaxed by a combination of conjugant gradients + quasi-dynamics. Equilibrium state of bubbles at different temperatures was studied by MD modeling at constant temperature over the range from 100 to 900 K over time of 300 ps. Interactions between moving edge dislocation ½<111>{110} and 2 nm bubbles at different temperature and He was simulated using a modification of the model described in [5]. Dislocations were moved under applied strain with rate 10^7 s^{-1}. Such simulations allow obtaining stress-strain information, maximum stress necessary to overcome an obstacle and dislocation line shape at any applied stress.

Surface energy.

Surface energy γ is necessary to estimate a pressure P inside a bubble of radius R using the capillarity model : $P=2\gamma/R$, used so far in theoretical predictions. We have estimated surface energy through void formation energy E_V as : $E_V = 3/4\pi R^2\gamma$.

In Fig.1 we present the dependence of the void formation energy and the corresponding surface energy estimated for voids of radius up to 10 nm. It can seen that void surface energy depends on radius for small voids but saturates at a value ~1.82 J/m^2 for voids larger than $R \approx 5$ nm.

Values of void surface energy obtained in static modeling were used for estimation of pressure inside bubbles in terms of the capillarity model and the results are presented in Fig.2.

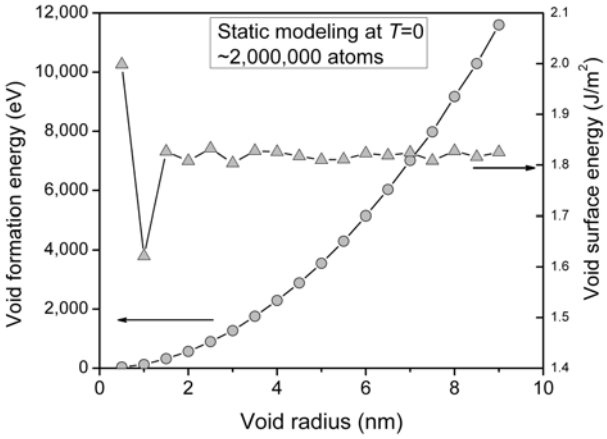

Fig.1 Void formation energy (circles) and the corresponding void surface energy (triangles) estimated for voids of different size.

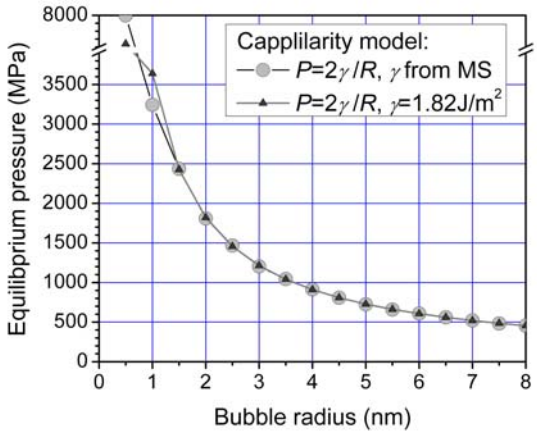

Fig.2 Equilibrium pressure for bubbles of different size using capillarity model and data from static modeling of voids.

The capillarity model usually used for such estimations have a number of deficiencies such as neglect of the bubble temperature and properties of matrix material. We therefore have applied MD to estimate equilibrium pressure as function of the ambient temperature and bubble radius. The criterion of equilibrium adopted here is a zero total dilatation of the bubble at different conditions. In practice we simulated bubble at the desired temperature and varied the number of He atoms inside until the total pressure in the simulated system is zero after annealing for 300 ps. The results are presented in Fig.3 and are compared with the values estimated above using capillarity model.

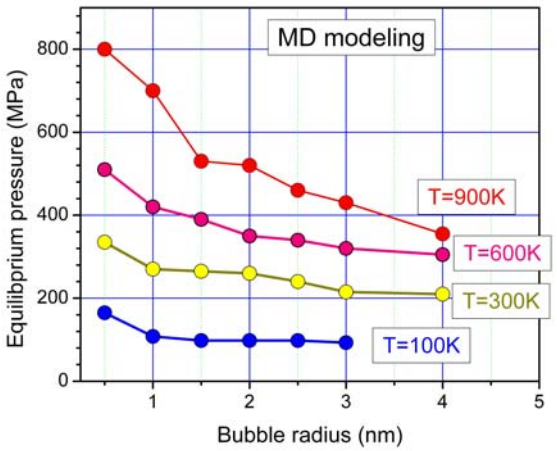

Fig.3 Equilibrium pressure of He inside bubbles of different size at different temperatures.

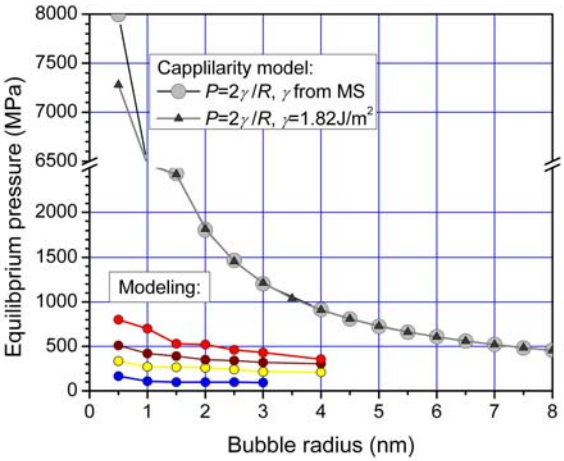

Fig.4 Comparison of bubble pressure estimated within capillarity model (grey circles and triangles) and equilibrium pressure of He estimated in MD modeling.

A comparison shows that the value of pressure estimated in MD modeling is significantly lower than that from capillarity model and the difference increases for small bubbles and low temperature.

This difference will be evaluated in future studies.

Bubble hardening.

Hardening effects due to bubbles was investigated by MD for the example of interaction with edge dislocation with ½<111> Burgers vector gliding on {110} plane. A bubble of 2 nm radius with its equator on the dislocation slip plane was placed 10 nm from the core in the direction of its motion. In this report we present first results with a relatively fast dislocation moving at 28 m/s under applied strain rate 10^7 s^{-1}. Lower applied strain rates are in progress as well as bubbles of radii 1 and 4 nm.

Maximum stress at which dislocations bypass the bubble at different temperatures and He/Vacancy content is presented in Fig.5. The results are compared with void of the same size simulated earlier.

Several qualitatively new results are obtained in this initial research. Thus, bubble with He/Vac = 0.5, that corresponds to close to equilibrium pressure in the above MD study, demonstrate the maximum hardening effect. Slightly under- and over- pressurized bubbles with He/Vac = 0.25 and 0.75 are softer than the equilibrium bubble, however, they are compatible or stronger than a void. The mechanism for the dislocation bypass of bubbles with He/Vac ≤ 1 is the same as for voids – the dislocation cuts and shears bubbles in the same way as void. However, at He/Vac = 2 we have observed that a relatively large glissile dislocation loops is emitted from the bubble when the dislocation approaches it. This loop then is absorbed by the dislocation as a superjog. In this mechanism the dislocation does not cut the bubble and the bubble size is increased after interaction. Temperature dependence of this interaction is opposite to that for lower He/Vac content.

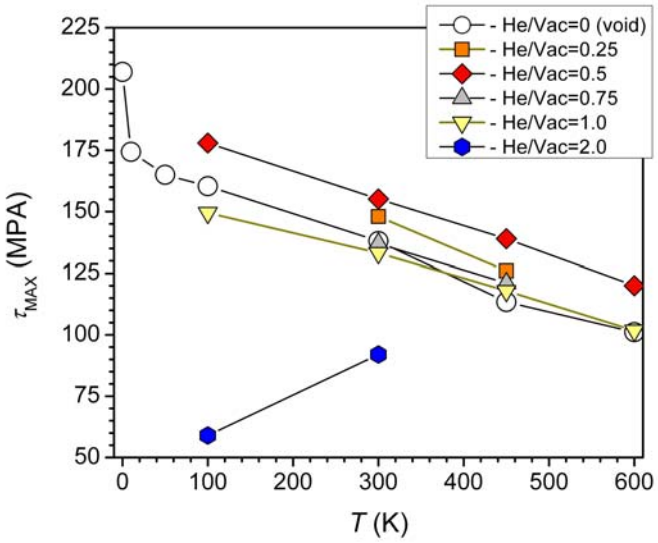

Fig.5 Critical resolved shear stress for edge dislocation ½<111>{110} to overcome a row of 2nm bubbles with different He content (He/Vac ratio) at different ambient temperature.

FUTURE STUDIES

1. Investigation of the equation of state for He-filled bubbles as function of bubble size, matrix properties and ambient temperature.
2. Understanding of the interaction mechanism, especially for equilibrium bubbles.
3. Simulation of bubbles of other sizes with another equilibrium He/Vac ratios.
4. Screw and mixed dislocations will be simulated.
5. Strain rate (dislocation velocity) effect will be investigated.

References

1. T. Seletskaia, Yu.N. Osetsky, R.E. Stoller, and G.M. Stocks, J. Nucl. Mater. **351** (2006) p. 109.
2. T. Seletskaia, Yu.N. Osetsky, R.E. Stoller, and G.M. Stocks, J. Nucl. Mater. **367-370** (2007) p. 355.
3. R.A. Aziz, A.R. Janzen, and M.R. Moldovan, Phys. Rev. Let. **74** (1995) p. 1586.
4. G.J. Ackland, D.J. Bacon, A.F. Calder, and T. Harry, Philos. Mag. A **75** (1997) p. 713.
5. Yu.N.Osetsky and D.J.Bacon, *Modelling and Simul. Mat. Sci. Eng.,***11**, 427 (2003).

VALIDATION OF EQUIBIAXIAL FLEXURAL TEST FOR MINIATURIZED CERAMIC SPECIMENS

— S. Kondo, Y. Katoh, J.W. Kim, L.L. Snead (Oak Ridge National Laboratory)

OBJECTIVE

The objective of this work is to develop a mechanical test technique which can utilize very small volume specimens of ceramic materials, is free from a strong effect of edge flaw, and can be applied to elevated temperature testing in addition to room temperature testing.

SUMMARY

For the purpose of evaluating fracture strength of irradiated ceramic specimens, a miniature disc equibiaxial flexural test technique was developed. It was applied to graphite specimens in a variety of combination of sample thickness and loading ring diameter to investigate the influences on the stress uniformity within the loading ring. Although similar and relatively high Weibull modulus were observed for all conditions ($m \approx 20$), the significant stress concentration associated with the large deflection was observed at the loading location for thinner specimens ($t<0.2$mm). However, the true local fracture stress was successfully estimated from the measured fracture load using finite element analysis. The method for estimating true local fracture stress appear reasonable for evaluating the fracture strength of dense poly-crystalline graphite, and can be used for determination of the statistical parameters for fracture stress of various ceramics.

PROGRESS AND STATUS

Introduction

For determination of fracture strength of neutron-irradiated monolithic ceramics and graphite materials, four-point flexural test is most commonly employed. Uni-axial flexural tests such as those in four-point and three-point configurations are simple and readily applicable to elevated temperature tests. However, these tests require specimens with substantial volumes, typically several cubic centimeters per specimen, for standard dimensions defined in various test standards. On the other hand, due to the statistical nature of ceramic strength, a set of data usually requires sample population of typically 30, making the total volume of samples required to produce statistically significant data difficult using the standard specimens. In order to avoid this difficulty, miniaturized flexural specimen geometries and dimensions are often employed in neutron irradiation studies.[1] However, such experiments frequently suffer from modification to the statistical strength due to edge flaws which have been introduced during specimen handling in hot cells and are very difficult to evaluate in a quantitative manner.

Among the alternative methods to the miniaturized uni-axial flexural tests, the equibiaxial flexural testing is a promising technique capable of 1) testing a specimen even smaller than the miniaturized flexural specimens, 2) applying a surface equibiaxial tensile loading onto a sample, 3) testing in a simple and robust manner, making post-irradiation evaluation fairly easy, 4) producing statistically significant data from a small volume neutron irradiation experiment, and 5) readily applicable to elevated temperature testing. Furthermore, the measurement of the strength of brittle materials under bi-axial flexure conditions rather than uniaxial flexure is often considered more reliable, because the maximum tensile stresses occur within the central loading area and spurious edge failures are eliminated. The objective of this work is to develop such an equibiaxial disc flexural test for strength determination of ceramic and graphite materials. In a previous report, [2] authors demonstrated that such a test technique developed is effective to determine the apparent flexural strength of thin specimen of pyrocarbon. However, the correction factor for estimating true local stress at the location of fracture origin, where the stress concentration is anticipated, from the apparent stress may be essential. The present work is intended to determine the influences of the sample thickness and loading ring diameter on the flexural strength using dummy graphite samples in an attempt to estimate the true local fracture stress at the location of fracture origin.

Experimental Procedure

The equibiaxial flexural test in a “ring-on-ring” configuration, where a disc specimen of ceramics is placed on a support ring and loaded with a smaller diameter coaxial loading ring, was adopted as a method of strength

evaluation at ambient temperature. This test method is often utilized for equibiaxial strength of brittle ceramics and the test procedure is standardized in ASTM C1499-05. [3]

A typical disc equibiaxial flexural test utilizes ceramic specimens of diameter of the order of one inch. However, because the evaluation of miniature samples requires testing using much smaller dimensions, a dedicated fixture was designed and fabricated. The section view of the test setup is shown in Fig. 1 and in a set of photographs in Fig. 2. The physical parameters of the test configuration and the condition of testing are summarized in Table 1.

Dummy specimens used were near-isotropic poly-crystalline nuclear graphite (AXF-5Q produced by Poco-Graphite Inc., TX, USA). Dimensions of the disc specimens were 6.0 mm (diameter) × 0.10, 0.15, and 0.20 mm (thickness). Whereas, only the tension side was polished by 6 mm diamond plate for most DL251T150 (see the notation in Table 1) using Minimet 1000 (Buehler Ltd., IL, USA), both surfaces of discs for DL116T100, DL116T150, DL116T350, DL251T100, L251T200, and L251T350 were polished in the same manner.

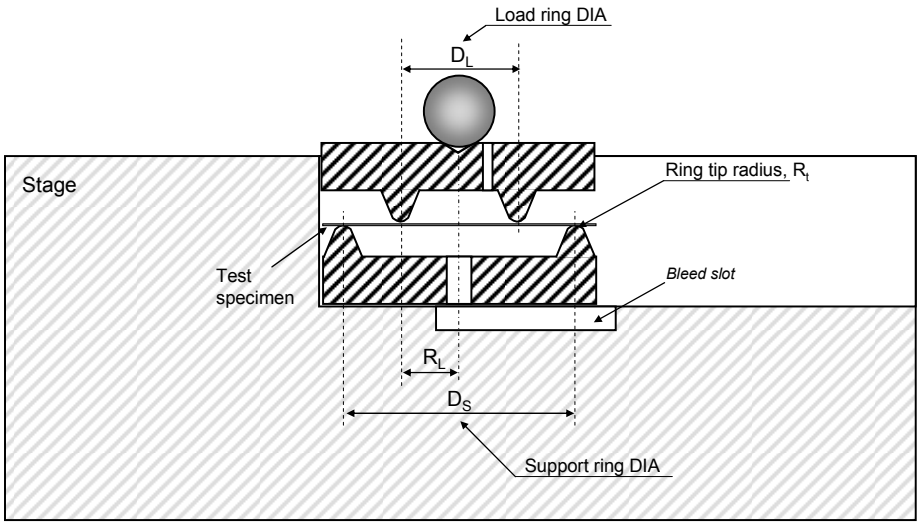

Fig. 1: Section view of the equibiaxial flexural test configuration.

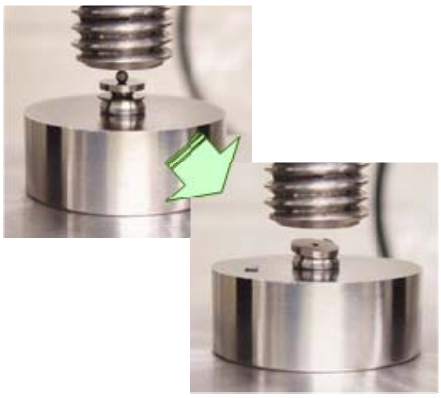

Fig. 2: Photographs of test specimen and fixture before (top-left) and after (bottom-right) testing.

Table 1: Physical parameters and condition of the tests.

Sample IDs	Loading Ring DIA. D_L [mm]	Avg. Sample Thickness t [mm]	Std. Dev. for t [mm]	Number of Specimens Tested [pcs.]
DL116T100	1.16	0.101	0.003	28
DL116T150	1.16	0.150	0.002	28
DL116T350	1.16	0.350	0.002	30
DL251T100	2.51	0.101	0.003	28
DL251T150	2.51	0.152	0.004	29
DL251T200	2.51	0.200	0.003	28
DL251T350	2.51	0.349	0.003	30

Estimation of true local stress

Results of the ring-on-ring tests for graphite thin discs (t≤0.2 mm) are summarized in Table 2. The load-displacement curves show large deflection (see displacement to thickness ratios in Table 2; d/t = 1.3-2.5) and non-linear load-displacement relationship as presented in Fig. 3. Such deviation from linear elastic theory have been previously observed in ring-on-ring testing for glass plate [4], and are associated with the reinforcing effect of outer overhang ($r > D_S$) which can not move freely toward the center. The displacements seem to depend on the loading ring diameter rather than the sample thickness. The failure patterns clearly indicate the stress magnification at the loading location as shown in Fig. 4. In the case of using the loading ring of smaller diameter (D_L = 1.16 mm), some fracture origins are likely located in the area just inside the loading ring. In order to quantitatively evaluate the location of fracture origin, the ratios of r_f to R_L were evaluated in this work, where the r_f is the radial distance between the likely crack origin and the disc center, the R_L is the loading ring radius. The mean r_f to R_L ratios were estimated to be 0.90 for t = 0.1 mm discs and 0.88 for t = 0.15 mm discs, indicating the fracture origin just inside the inner ring. For the tests with larger load ring (D_L = 2.51 mm), the r_f/R_L ratios show higher values (r_f/R_L = 0.92-0.95) compared to smaller load ring case, indicating much significant localized stress near the loading location.

Table 2: Summary of results of ring-on-ring test for thin graphite discs.

Sample IDs	Avg. Displacement d [mm]	Avg. Fracture Load F [N]	Mean Fracture Origin r_f/R_L	Weibull Mean Local Stress[1)] $\sigma_{p,max}$ [MPa]	Std. Dev. for $\sigma_{p,max}$ [MPa]	Weibull Modulus m
DL116T100	0.252	3.13	0.90	134	9.16	18.1
DL116T150	0.259	5.23	0.88	143	9.42	18.8
DL251T100	0.239	5.62	0.95	127	8.61	18.3
DL251T150	0.229	8.79	0.92	126	10.4	14.8
DL251T200	0.226	13.6	0.94	133	8.49	19.5

1) Local flexural stresses were estimated from fracture load by finite element method.

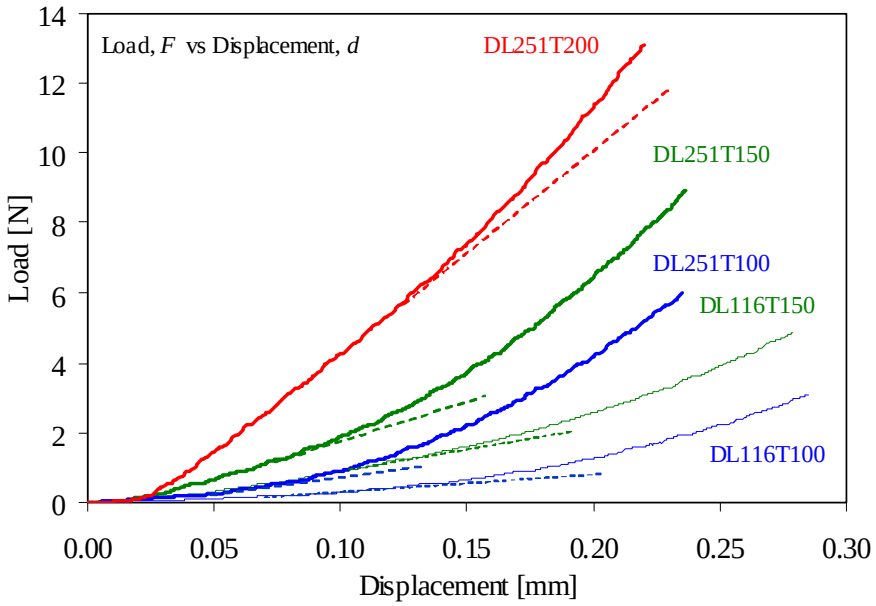

Fig. 3: Typical load-displacement curve for thin disc samples.

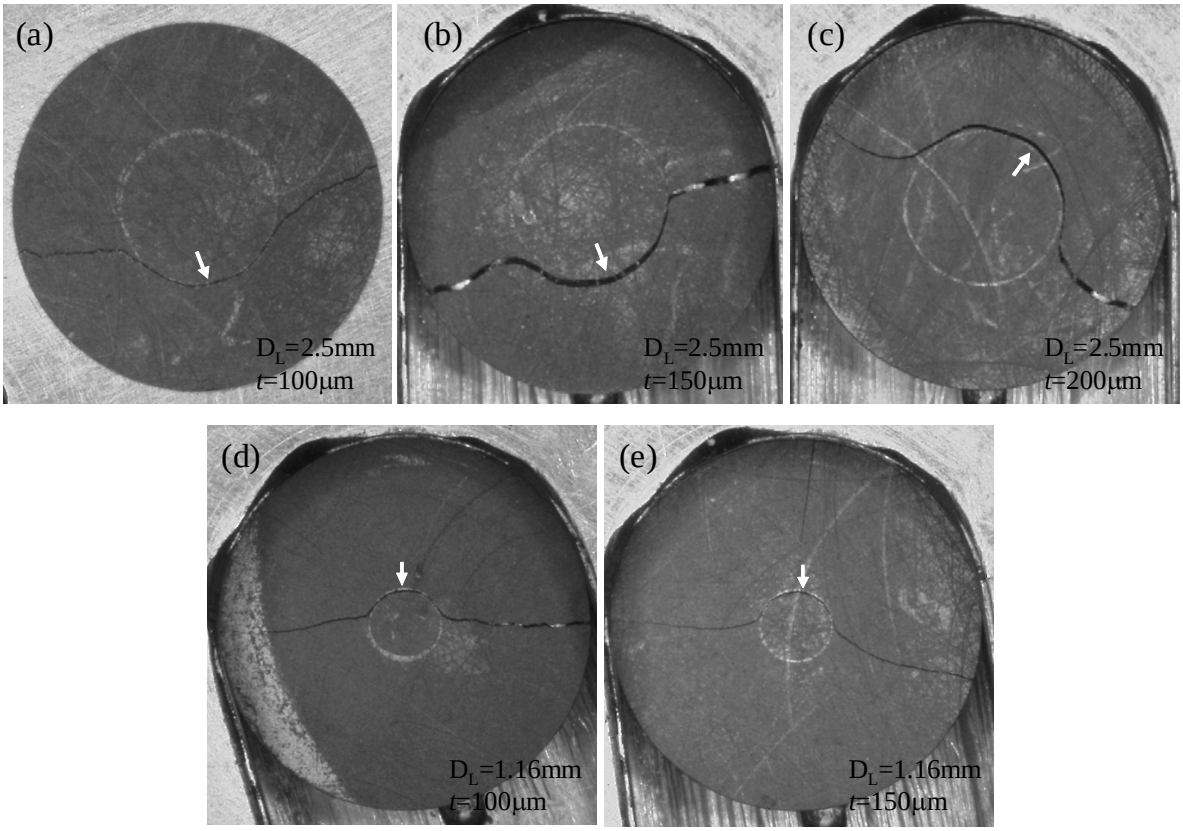

Fig. 4: Failure patterns of graphite discs tested by loading ring with D_L=2.51 for t=;(a)100, (b)150, (c)200μm, or D_L=1.16mm for t=; (d)100, (e)150μm. Likely fracture origins are indicated by arrows (viewed from compression sides for clear vision of loading ring trace).

Kao et al. reported that stress magnification at the loading point is significant when the plate deflection exceeds one-half the specimen thickness [5]. In that case, the equibiaxial stress calculation following ASTM 1499-05 may not be utilized to relate the flexural strength to the flexural load. The local stress at the loading location in a ring-on-ring configuration has been empirically and analytically approximated considering the ratio of deflection to specimen thickness in an attempt to solve the nonlinear plate equations [5,6]. However, these valuable solutions have no application to thin graphite samples because of the significant deviation from Hooke's law or elastic-plastic fracture behavior. Therefore, finite element analysis was employed in this study to estimate the true local stress from the applied load. Figure 5 shows the radial stress distribution in the ring-on-ring loading for the same material and experimental conditions as Table 1. The stress magnifications beneath (or near) the loading point are computationally well demonstrated by the finite element analysis. The local stress at the loading point is estimated to be twice as large as that at disc center for the t= 100 μm, D_L= 2.51 mm case. For smaller loading ring case (t= 100 μm, D_L= 1.16 mm), somewhat more uniform stress distribution is observed, where the maximum stress is about 1.3 times larger than the center stress. Therefore, one can conclude that the fracture load is governed primarily by the local stress associated with the significant curvature at the loading point in all cases tested.

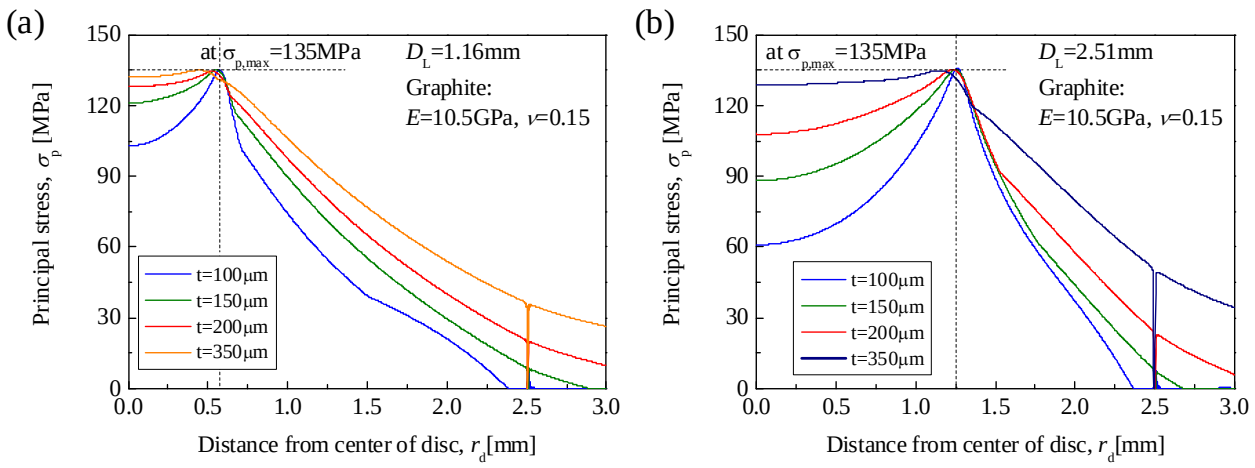

Fig. 5: Radial stress distribution at an approximate flexure stress at the loading location (~135MPa) analyzed by finite element method.

Figure 6 shows the Weibull statistical plots of the flexural strength of graphite discs, where the true local stress at the loading point was estimated from the fracture load using finite element calculation. The Weibull mean strengths are summarized in Table 2. Although strength were not widely scattered for each case, slight higher strength for using D_L=1.16 mm case (σ_f=134, 143 MPa) than the D_L=2.51 mm case (σ_f=127-133 MPa) was observed. All the measured fracture strength are higher than the commercially reported flexural strength of 86 MPa (standard four-point flexural test [7]) and the typical reported value of 113 MPa for small size bend specimens (2.3 × 6 × 30 mm [8]). For most ceramics, strength depends on the effective stressed area or volume because of the statistical distribution of strength-controlling flaws such as machining flaws [9]. The limited effective-stressed area might modify the results of the present work, though no consistent relationship between bi-axial and uni-axial flexural strength data has been established [10,11]. It is worth noting that the similar and relatively high Weibull modulus (m= 18.1-19.5) for each test set except for DL251T150 (m= 14.8) were observed. The slight smaller Weibull modulus for DL251T150 is possibly due to the variety of the roughness for the as machined compressive surface and/or the presence of the residual stress at there.

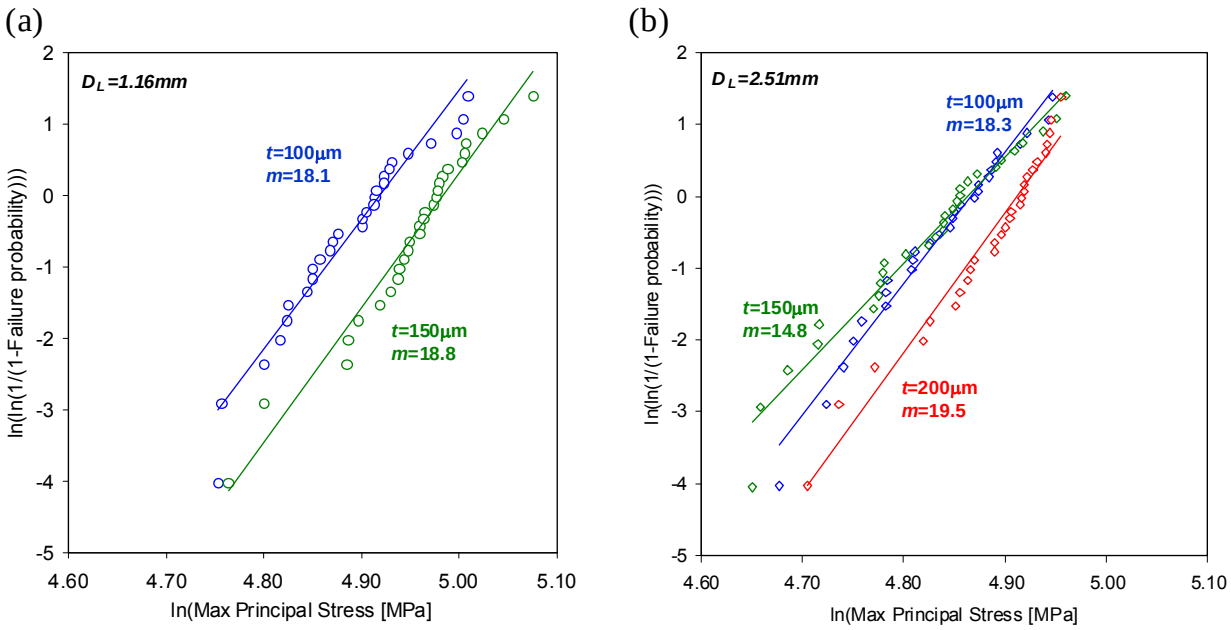

Fig. 6: Weibull distribution of flexural strength of graphite specimens with different thickness tested by loading ring with diameter of ; (a) D_L =1.16mm, (b) D_L =2.51mm.

Comparison with result from thicker samples

Results of the ring-on-ring tests for thick graphite discs (t=0.35 mm) are summarized in Table 3. The load-displacement curve shows relatively small displacement to thickness ratio (d/t=0.55-0.64) and non-linear load-displacement relationship at d>~0.1 mm as presented in Fig. 7. The direction of deviation from the linear load-displacement is opposite of the thinner disc cases. It is well known that strain-stress curve of graphite both in uni-axis static tensile and compressive condition show a non-linear curve due to the decrease in Young's modulus [12]. Therefore, the reinforcing effect of the overhang is insignificant to such an extent that the deviation hide behind the intrinsic degradation of Young's modulus for the cases of thick samples. Figure 8 shows the typical failure patterns of the thicker discs for using the load ring with D_L =1.16 mm and D_L =2.51 mm, respectively. Although, the likely fracture origins, which are indicated by arrows in Fig. 8, are located within inner ring contact lines for both loading ring cases, the flaw characteristics are significantly different. The crack was frequently deflected along the inner side of the load ring for D_L =2.51 mm case, whereas the approximately-straight cracks are seen in the D_L =1.16 mm case. As listed in Table 3, the mean r_f/R_L ratio for the case of using larger load-ring is three times larger than the smaller load-ring case. The much larger r_f/R_L ratio of 0.6 for DL251T350 may be attributed to the stress magnification that is still remaining inside the inner ring. Because the indirect crack growth normally increases the fracture energy, relatively higher strength might be observed for the D_L =2.51 mm case. Indeed, the strength of DL251T350 was clearly higher than that of the others in spite of the anticipated larger effective stressed area. The very limited reinforcing effects and near uniform stress distributions in a smaller loading ring configuration also observed in our FE analysis for thicker samples. From the both experimental and FE analysis results, the equibiaxial strength is confidently determined to be 129 ± 7.8 MPa for graphite with the identical surface condition.

Table 3: Summary of results of ring-on-ring test for thick graphite discs.

Sample	Avg. Displacement d [mm]	Avg. Flexure Load F [N]	Mean Fracture Origin r_f/R_L	Weibull Mean Flexural Stress σ_f [MPa]	Std. Dev. for σ_f [MPa]	Weibull Modulus m
DL116T350	0.191	16.8	0.22	129	7.80	20.7
DL251T350	0.224	35.5	0.76	143	6.60	27.3

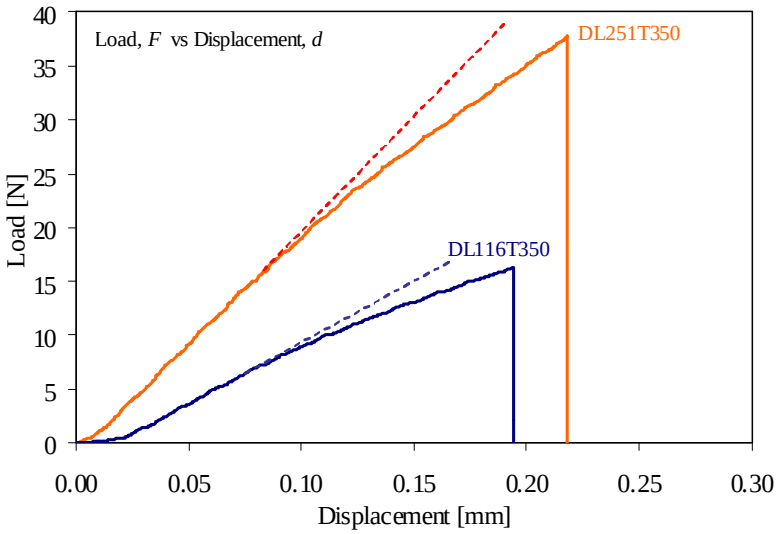

Fig. 7: Typical load-displacement curve for thin disc samples.

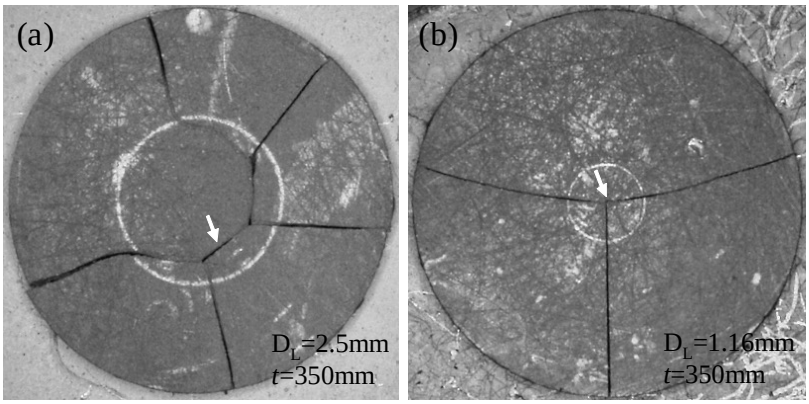

Fig. 8: Failure patterns of graphite discs tested by loading ring in the condition of; (a) D_L=2.51 mm t=350 μm, (b) D_L=1.16mm, 350μm. Likely fracture origins are indicated by arrows (viewed from compression sides for clear vision of loading ring trace).

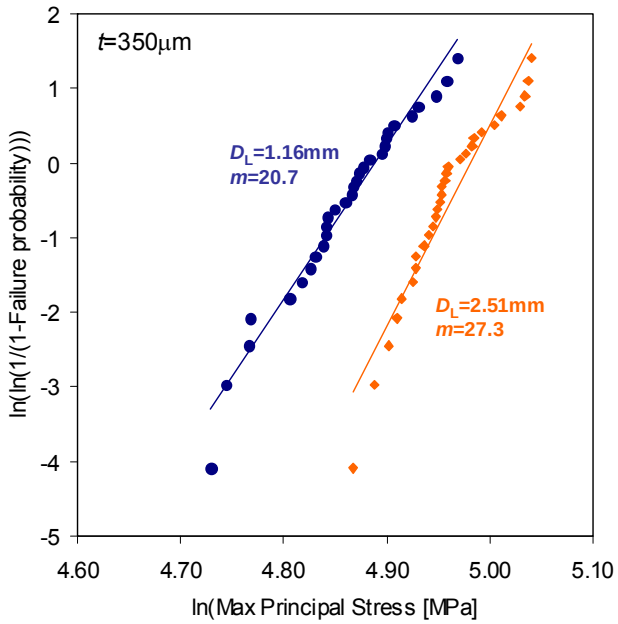

Fig. 9: Weibull distribution of equibiaxial strength of graphite specimens.

Figure 9 shows the Weibull statistical plots of the equibiaxial strength of graphite discs, where assuming principal stresses are uniform within the inner ring and estimated following eq. (7) in ASTM 1499-05 [2]. Although the reason for the slight smaller magnitude of Weibull modulus for DL116T350 (m = 20.7) is not clear, it is similar to the average m value for the test series of thinner discs. This is indicative that a single flaw type is responsible for the failure primarily due to the successful elimination of the edge failure. In this case, a simple methodology is used to convert the strength obtained with one test geometry to strength representing another test geometry: [13],

$$\frac{\sigma_1}{\sigma_2} = \left(\frac{S_1^{\text{eff}}}{S_2^{\text{eff}}} \right)^{-\frac{1}{m}} \tag{1}$$

where the subscripts 1 and 2 denote two deferent geometries of test specimens or configuration, S^{eff} is the effective surface area, m is the surface flaw controlling Weibull modulus. Particularly with small size specimen, the effect of stressed surface or volume on failure probability must be considered in order to extrapolate the measured strength to the strength of full size components. Figure 10 shows the flexural strength as a function of effective surface area for all test sets. The effective surface area were estimated based on the results of r_f/R_L ratio evaluation, where the uniform stress were assumed to be ranging from the loading point to lower limit of the standard deviation of r_f/R_L ratio. The slope of the linear-regression fitted line (loading length regressed on strength in this instance) is -1/m, which leads to an additional estimate of the Weibull modulus as 23.1. The additional Weibull modulus is slight larger than the m values obtained from results of each test sets, but it is still comparable to those results, which implies that the total area of stress magnified region may modify the apparent strength due to the size effect. Furthermore, the successfully scaled m value implies that Weibull material parameters such as characteristic strength and scale parameter can be certainly estimated from the ring-on-ring test results for high E/σ materials like PyC.

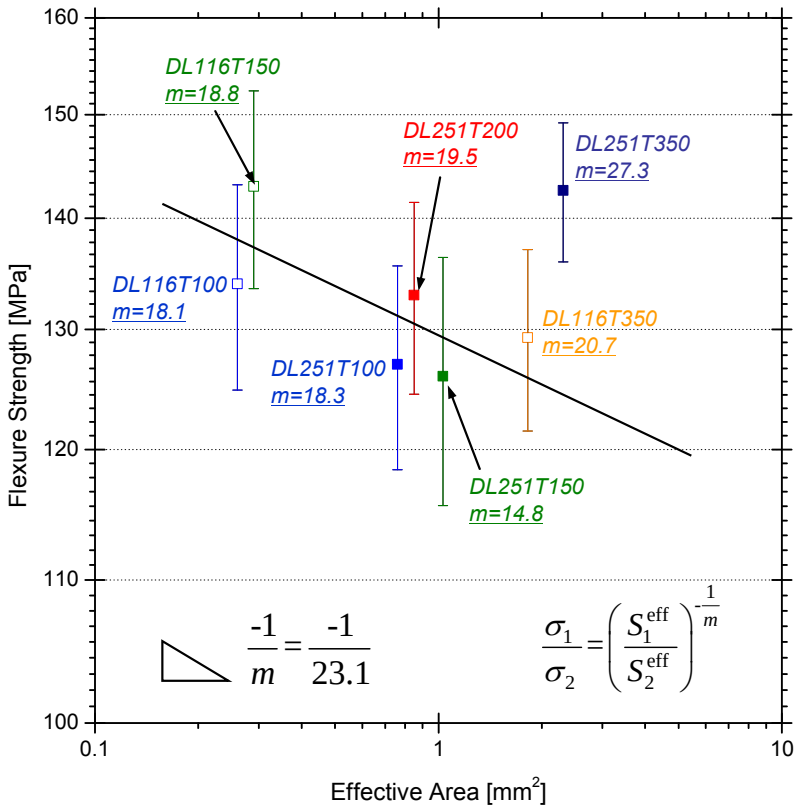

Fig. 10: Flexural strength versus effective surface area for specimens with different thickness.

References

[1] L.L. Snead, T. Hinoki, Y. Katoh, “Strength of neutron irradiated silicon carbide and silicon carbide composite,” Fusion Materials, ORNL/TM-2008/164, 49 (2002).

[2] ASTM Standard C1499-05, “Standard Test Method for Monotonic Equibiaxial Flexural Strength of Advanced Ceramics at Ambient Temperature,” ASTM International, West Conshohocken, PA.

[3] R. Kao, N. Perrone, and W. Capps, “Large-Deflection Solution of the Coaxial-Ring-Circular-Glass-Plate Flexure Problem,” J. Am. Ceram. Soc., 54,566-571 (1971).

[4] J.B. Wacgtman Jr., W. Capps, J. Mandel, Biaxial Flexure Tests of Ceramic Substrates, J. Mater. 7, 188-194 (1972).

[5] J. Malzbender, R.W. Steinbrech, “Fracture test of thin sheet electrolytes for solid oxide fuel cells,” J. Euro. Ceram. Soc. 27, 2597-2603 (2007).

[6] POCO Graphite, Inc., Decatur, TX. http://www.poco.com/

[7] L.L. Snead, T.D. Burchell, A.L. Qualls, Strength of Neutron-Irradiated High-Quality 3D carbon fiber composite, J. Nucl. Mater 321, 165-169 (2003).

[8] J. Lamon, A.G. Evans, Statistical Analysis of Bending Strengths for Brittle Solids: A Multiaxial Fracture Problem, J. Am. Ceram. Soc. 66, 177-182 (1990).

[9] M.N. Giovan, G. Sines, “Biaxial and Uniaxial Data for Statistical Comparison of a Ceramics’s Strength,” J. Am. Ceram. Soc., 52, 510-515 (1979).

[10] D.K. Shetty, A.R. Rosenfield, W.H. Duckworth, P.R. Held, “A Biaxial-Flexure Test for Evaluating Ceramics Strength,” J. Am. Ceram. Soc., 66, 36-42 (1983).

[11] S. Yoda, M. Eto, T. Oku, Change in dynamic young's modulus of nuclear-grade isotropic graphite during tensile and compressive stressing, J. Nucl. Mater., 119, 278-283 (1983).

[12] ASTM Standard C1683-08, “Standard Practice for Size Scaling of Tensile Strength Using Weibull Statistics for Advanced Ceramics,” ASTM International, West Conshohocken, PA.

HFIR Irradiation Experiments – F. W. Wiffen, Oak Ridge National Laboratory

The current status of Fusion Materials Program irradiation experiments in the HFIR reactor is tabulated.

Table - Summary of Recent, Current and Planned Fusion Materials Program Experiments in the High Flux Isotope Reactor (HFIR)

Experiment Designation	Primary Materials	Specimen Types*	Irradiation Temperature (°C)	Max Exposure (dpa)	Number of Reactor Cycles	Irradiation Period (month/year)
Beryllium reflector (RB) irradiation positions						
RB-15J	F82H	T, F, FT	300, 400	6	10	6/08 – 12/09
Target zone capsules						
JP-25	F82H	T, FT	300, 500	20	10	2/99 - 1/10
JP-26	F82H	T, FT	300,400,500	9	50	
JP-27	F82H	T, FT	300, 400	21	13	12/03 - 1/08
JP-28	F82H	T, FT	300,400,500	80-?	50	1/05 – 6/13
JP-29	F82H	T, FT	300,400,500	80	50	1/05 - 6/13
Target zone rabbit capsules						
F8A-1	F82H	T, FT	300	50	28	2/09 – 6/13
F8A-2	“	“	“	“	“	“
F8B-1	“	“	“	“	“	“
F8B-2	“	“	“	“	“	“
Target zone rabbit capsules						
JCR-1	SiC/SiC	Bend bars	800	30	15	10/04 – 1/09
JCR-2	“	“	“	“	“	“
JCR-3	“	“	“	“	“	“
JCR-4	“	“	“	“	“	“
JCR-5	“	“	“	>50	>25	10/04 - ??
JCR-6	“	“	“	“	“	“
JCR-7	“	“	“	“	“	“
JCR-8	“	“	“	“	“	“
JCR-9	“	“	500	30	15	10/04 – 1/09
JCR-10	“	“	“	“	“	“
JCR-11	“	“	“	“	“	“
JCR-12	“	“	“	“	“	“

*T = Tensile, F = Fatigue, FT = Fracture Toughness. Most experiments also contain TEM disks and other specimens and monitors occupying a small portion of the available volume.

ASSEMBLY OF THE US-JAPAN MFE-RB-15J EXPERIMENT FOR IRRADIATION IN THE HFIR

– T. Hirose, M. Ando, H. Tanigawa, N. Okubo (Japan Atomic Energy Agency), J. L. McDuffee, D. W. Heatherly, R. G. Sitterson, R. E. Stoller (Oak Ridge National Laboratory) and T. Yamamoto (University of California, Santa Barbara)

OBJECTIVE

This work is being carried out under the Collaboration on Fusion Materials between the U.S. DOE and the Japan Atomic Energy Agency. The MFE-RB-15J capsule is a part of the Phase-V experimental program with the goal of elucidating the effects of helium generation in fusion structural candidate engineering alloys, and verifying the irradiation response of alloy F82H base metal and welds for ITER-TBM (Test Blanket Module) application. The target dose of this capsule is 6 dpa at the peak and it will introduce 300 appm of transmutation helium in F82H doped with boron-10.

SUMMARY

Assembly of the MFE-RB-15J capsule was completed in April, 2008 and installed in HFIR location RB-1A inside a europia thermal neutron shield.. Irradiation began with cycle 415, starting June 3, 2008. A detailed specimen loading list for the capsule is provided in this report.

PROGRESS AND STATUS

Introduction

This experiment is being carried out within the framework of the US DOE-JAEA Collaboration on Fusion Materials, which is in its fifth phase. The goals of the experiment include the investigation of the effects of helium on fracture properties, and the development of engineering data on the fusion candidate alloy F82H and joints made by welding (TIG and EB) and HIP. The data is needed for ITER-TBM design and alloy qualification. A more detailed description of the experiment will be provided in a subsequent report. This report provides a summary of the specimen preparation for the MFE-RB-15J experiment.

Design Description

The design of the MFE-RB-15J is very similar to that of MFE-RB-17J [1]. The main differences between these two are irradiation temperature and the structural material. The MFE-RB-15J is optimized for irradiation at 300 and 400^{o}C, and the structural material of the capsule is stainless steel, (instead of the molybdenum used in -17J specimen holders.) In the MFE-RB-15J experiment three axially stacked specimen holders are located within a common inner containment housing (top, middle and bottom), which is itself contained in an outer housing. The top and bottom holders are irradiated at 300°C and the middle one at 400°C. The 300°C holder is partitioned into three regions and the 400°C holder into five regions to distribute and locate the specimens. The specimen holders are filled with lithium, to reduce thermal gradients during irradiation. The experiment placed in an annular europium oxide shield and loaded into the RB-1A position. The purpose of the shield is to reduce helium production from ^{10}B transmutation in the initial part of the irradiation [2,3]. The shield used in this experiment had been used previously for several cycles with experiments, MFE-RB-10J and MFE-RB-14J.

Specimen Loading

The specimen materials in this experiment are summarized in Table 1. The specimen types include six types of toughness specimens (0.18”DCT, 0.14”DCT, half-1/3CVN, half-1/3PCCVN, Multi5-PCCVN, DFMB), sheet tensile specimens (SS-J3), pressurized creep tubes (PT), hourglass fatigue specimens (SF-1), atom probe specimens (APFIM), and miniature multipurpose coupons (MMPC). The fatigue specimen, SF-1 is newly employed for this experiment, and is described elsewhere [4]. The overall layout of MFE-RB-15J experiment is summarized in Table 2.

Table 1 Materials list for MFE-RB-15J experiment

ID	Description
F82H IEA [5]	8Cr-2W RAF/Ms, F82H IEA heat (F82H-mod.)
F82H TIG WM [6]	TIG weld metal of F82H joint
F82H TIG FG HAZ [7]	Fine grained HAZ from TIG weld joint, heated above A_{C1}transformation temperature
F82H TIG OT HAZ [7]	Over tempered HAZ from TIG weld joint, heated below A_{C1} Transformation temperature
F82H HIP [8]	HIP joint of F82H processed at 1100°C followed by heat treatment at 960°C and 750°C
F82H+10BN [9]	F82H with additional 60 wppm Boron-10
F82H+11BN [9]	F82H with additional 60 wppm Boron-11
F82H EB WM [10]	Weld metal of F82H Electron Beam weld joint
F82H EB HAZ [10]	HAZ from F82H Electron Beam weld joint
F82H mod3 [11]	F82H with 0.1% of Tantalum
Eurofer97 [12]	9Cr-1W RAF/Ms
U14YWT1000 [13]	ODS steel consolidated at 1000°C
U14YWT1150 [13]	ODS steel consolidated at 1150°C
US MA957	Commercial ODS steel

Table 2 Layout of the MFE-RB-15J experiment

Region	Specimen Type	Design Temp. (^{o}C)	Distance above HMP* (mm)		
			Top	Middle	Bottom
Top-C	APFIM, 0.14"DCT, MMPC, SJ3	300	180	168	155
Top-B	PT, SF1	300	155	142	129
Top-A	hf-1/3CVN, SJ3, M5PCCVN**	300	129	116	103
Middle-E	0.18"DCT, DFMB, SJ3	400	57.4	48.6	39.8
Middle-D	PT, hf-1/3CVN, hf-1/3PCCVN, SF1,SJ3	400	39.4	26.5	13.7
Middle-C	hf-1/3CVN, SF1,SJ3	400	13.3	0.4	-12.5
Middle-B	PT, hf-1/3CVN, SF1	400	-12.9	-25.8	-38.7
Middle-A	0.18"DCT, M5PCCVN**	400	-39.1	-48.0	-57.0
Bottom-C	0.14"DCT, hf-1/3CVN, SJ3	300	-103	-115	-128
Bottom-B	PT, hf-1/3CVN, SJ3	300	-129	-142	-155
Bottom-A	SF1, SJ3, M5PCCVN**	300	-155	-167	-180

* HMP - Horizontal mid-plane of the HFIR

** M5PCCVNs located over A, B and C regions.

Figure 1 shows the arrangement of the specimen holders. The regions are separated by stainless steel spacers, which are approximately 25 mm in length. As shown in this figure, the M5PCCVN specimens (54 mm in length) span three regions. The total length of the specimen-containing zone is 360 mm, and the fluence fraction, Pf, at the ends of this zone is approximately 0.7 of the mid-plane value.

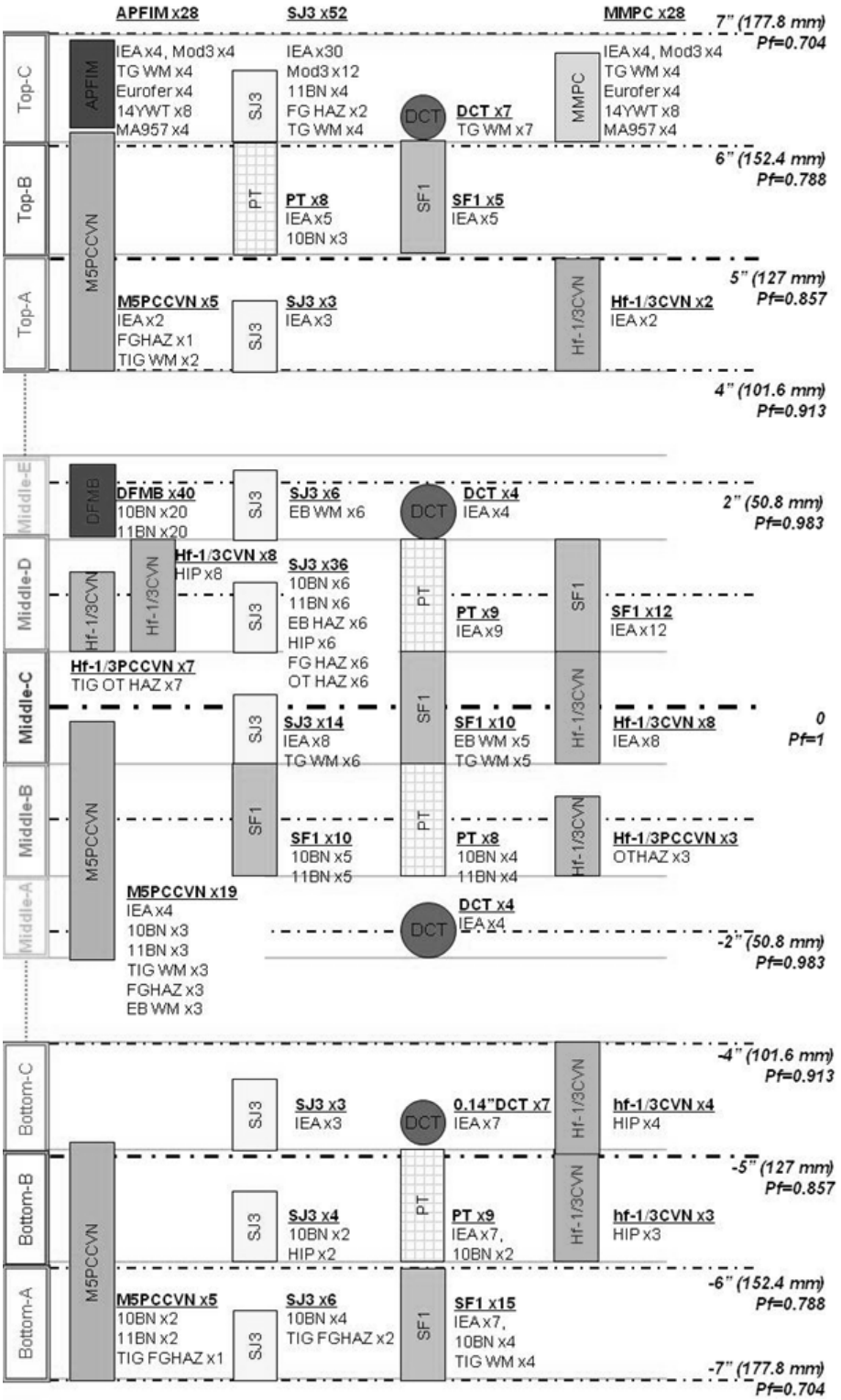

Figure 1 Schematic view of the MFE-RB-15J experiment, showing specimen holders and loading.

The detailed specimen loading is given in Table 3.

Future Work
The MFE-RB-15J capsule will be irradiated to a peak fluence of 6 dpa and 4.2 dpa at ends of the specimen zone, which will take approximately ten HFIR cycles. This will introduce 300 appm of transmutation helium in F82H+10BN. The irradiation will be completed with cycle 424.

Table 3. MFE-RB-15J Loading List, Identifying each specimen by specimen number, type, material, and location in the experiment.

MFE-RB-15J, 300°C top-C region (~ 155 ~ 180 mm above reactor mid plane)

-APFIM (28 pieces)

EUROFER 97:	RA, RB, RC, RD
F82H IEA:	1A, 1B, 1C, 1D
F82H mod3:	HA, HB, HC, HD
F82H TIG WM:	2A, 2B, 2C, 2D
U14YWT1000:	ZUA, ZUB, ZUC, ZUD
U14YWT1150:	ZTA, ZTB, ZTC, ZTD
US MA957:	ZSA, ZSB, ZSC, ZSD

-0.14”DCT (7 pieces)

F82H IEA:	1VXA, 1VXB, 1VXC, 1VXD, 1VXE, 1VXF, 1VXG

-MMPC (28 pieces)

EUROFER 97:	RA, RB, RC, RD
F82H IEA:	1A, 1B, 1C, 1D
F82H mod3:	HA, HB, HC, HD
F82H TIG WM:	2A, 2B, 2C, 2D
U14YWT1000:	ZUA, ZUB, ZUC, ZUD
U14YWT1150:	ZTA, ZTB, ZTC, ZTD
US MA957:	ZSA, ZSB, ZSC, ZSD

-SSJ3 tensile (52 pieces)

F82H+11BN:	EX0, EX1, EX2, EX3
F82H TIG FG	HAZ:21V0, 21V1
F82H TIG WM:	1V0, 1V1, 1V2, 1V3
F82H mod3:	HX0, HX1, HX2, HX3, HX4, HX5, HY0, HY1, HY2, HY3, HY4, HY5
F82H IEA:	0VAa, 0VAb, 0VAc, 0VAd, 0VAe, 0VAf, 0VAg, 0Vah, 0VAj, 0VAk, 0VAm, 0VAn, 0VAp, 0VAq, 0VAr, 0VAs, 0VAt, 0VAu, 0VAv, 0VAw, 0WAa,0WAb, 0WAc, 0WAd, 0WAe, 0WAf, 0Wag, 0WAh,0WAj, 0WAk

MFE-RB-15J, 300°C top -B region (~ 129 ~ 155 mm above reactor mid plane

-Pressurized creep tube (8 pieces)

F82H+10BN:	DXP0, DXP1, DZP2
F82H IEA:	0XP0, 0XP3, 0XP5, 0XP9, 0ZP4

-SF-1 fatigue (5 pieces)

F82H IEA:	0X6, 0X7, 0X8, 0X9, 0XA

MFE-RB-15J, 300°C top-A region (~ 103 ~ 129 mm above reactor mid plane)

-hf-1/3CVN (2 pieces)

F82H IEA:	0XS, 0XT

-SS-J3 tensile (3 pieces)

F82H IEA:	0X0, 0X1, 0X2

MFE-RB-15J, 300°C spanning top-A, B and C regions (~ 103 ~ 157 mm above mid plane)

-M5PCCVN (5 pieces)

F82H IEA: 0VB, 0VC
F82H TIG FG HAZ: 21V4
F82H TIG WM: 1V4, 1V5

MFE-RB-15J, 400°C middle holder, E-zone (~ 39.8 ~ 57.4 mm above reactor mid plane)

-0.18”DCT (4 pieces)

F82H IEA: 0WEa, 0WEb, 0WEc, 0WEd

-DFMB (40 pieces)

F82H+10BN: DXHa, DXHb, DXHc, DXHd, DXHe, DXHf, DXHg, DXHh, DXHi, DXHk, DYHa, DYHb, DYHc, DYHd, DYHe, DYHf, DYHg, DYHh, DYHi, DYHk
F82H+11BN: EXHa, EXHb, EXHc, EXHd, EXHe, EXHf, EXHg, EXHh, EXHi, EXHk, EYHa, EYHb, EYHc, EYHd, EYHe, EYHf, EYHg, EYHh, EYHi, EYHk

-SSJ3 tensile (6 pieces)

F82H EB WM: 27W0, 27W1, 27W2, 27W3, 27W4, 27W5

MFE-RB-15J, 400°C middle holder, D-zone (~ 13.7 ~ 19.4 mm above reactor mid plane)

-hf-1/3CVN (8 pieces)

F82H HIP: BAY6, BAY7, BAY8, BAY9, BAYA, BAYC, BAYE, BAYH

-hf-1/3PCCVN (7pcs)

F82H TIG OT HAZ: 22W7, 22W8, 22W9, 22WA, 22WB, 22WC, 22WD

-Pressurized creep tube (9 pieces)

F82H IEA: 0XPA, 0YPA, 0YPB, 0YP7, 0YP9, 0XP8, 0YP5, 0YP3, 0ZP2

-SF-1 fatigue (12 pieces)

F82H IEA: 0XJ, 0Y6, 0Y7, 0Y8, 0Y9, 0YA, 0YB, 0YC, 0YD, 0YE, 0YF, 0YG

-SSJ3 tensile (36 pieces)

F82H+10BN: DY0, DY1, DY2, DY3, DY4, DY5
F82H+11BN: EY0, EY1, EY2, EY3, EY4, EY5
F82H EB HAZ: 28W0, 28W1, 28W2, 28W3, 28W4, 28W5
F82H HIP: BAY0, BAY1, BAY2, BAY3, BAY4, BAY5
F82H TIG FG HAZ: 21W0, 21W1, 21W2, 21W3, 21W4, 21W5
F82H TIG OT HAZ: 22W0, 22W1, 22W2, 22W3, 22W4, 22W5

MFE-RB-15J, 400°C middle-C region (~12.5 ~ 13.3 mm above reactor mid plane)

-hf-1/3CVN (8 pieces)

F82H IEA: 0YS, 0YT, 0YV, 0YW, 0WG, 0WH, 0WJ, 0WK

-SF-1 fatigue (10 pieces)

F82H EB WM: 27W9, 27WA, 27WC, 27WE, 27WH
F82H TIG WM: 1W8, 1W9, 1WA, 1WB, 1WC

-SSJ3 tensile (14 pieces)

F82H IEA: 0Y0, 0Y1, 0Y2, 0Y3, 0Y4, 0Y5, 0YM, 0YN
F82H TIG WM: 1W0, 1W1, 1W2, 1W3, 1W4, 1W5

MFE-RB-15J, 400°C middle-B region (~ 12.9 ~ 38.7 mm below reactor mid plane)

-hf-1/3PCCVN (3 pieces)

F82H TIG OT HAZ: 22WE, 22WF, 22W6

-Pressurized creep tube (8 pieces)

F82H+10BN: DYP9, DYP8, DYP7, DYP6
F82H+11BN: EXP0, EZP0, EYP9, EYP8

-SF-1 fatigue (10 pieces)

F82H+10BN: DYJ, DYK, DYM, DYN, DYP
F82H+11BN: EYJ, EYK, EYM, EYN, EYP

MFE-RB-15J, 400°C middle-A region (~ 39.1 ~ 57 mm below reactor mid plane)

-0.18" DCT (4 pieces)

F82H IEA: 0WEe, 0WEf, 0WEg, 0WEh

MFE-RB-15J, 400°C spanning middle-A, B and C regions (~ 3 ~ 57 mm below mid plane)

-M5PCCVN (19 pieces)

F82H+10BN: DY6, DY7, DY8
F82H+11BN: EY6, EY7, EY8
F82H EB WM: 27W6, 27W7, 27W8
F82H IEA: 0YK, 0WB, 0WC, 0WD
F82H TIG FG HAZ: 21W6, 21W7, 21W8
F82H TIG WM: 1W6, 1W7, 1WC

MFE-RB-15J, 300°C bottom-c region (~ 103 ~ 128 mm below reactor mid plane)

-0.14"DCT (7 pieces)

F82H IEA: 0VXA, 0VXB, 0VXC, 0VXD, 0VXE, 0VXF, 0VXG

-hf-1/3CVN (4 pieces)

F82H HIP: BAX6, BAX7, BAX8, BAX9

-SSJ3 tensile (3 pieces)

F82H IEA: 0X3, 0X4, 0X5

MFE-RB-15J, 300°C bottom-B region (~ 129 ~ 155 mm below mid plane)

-hf-1/3CVN (3 pieces)

F82H HIP: BAXA, BAXC, BAXE

-Pressurized creep tube (9 pieces)

F82H+10BN: DXP2, DXP3
F82H IEA: 0VP1, 0WP1, 0XP2, 0XP6, 0XP7, 0ZP0, 0ZP1

-SSJ3 tensile (4 pieces)

F82H+10BN: DX4, DX5
F82H HIP: BAX0, BAX1

MFE-RB-15J, 300°C bottom-A (~ 155 ~ 180 below reactor mid plane)

-SF-1 fatigue (15 pieces)

F82H+10BN: DXJ, DXK, DXM, DXN
F82H IEA: 0XB, 0XC, 0XD, 0XE, 0XF, 0XG, 0XH
F82H TIG WM: 1V6, 1V7, 1V8, 1V9

-SSJ3 tensile (6 pieces)

F82H+10BN: DX0, DX1, DX2, DX3
F82H TIG FG HAZ: 21V2, 21V3

MFE-RB-15J, 300°C spanning bottom-A, B and C regions (~ 155 ~ 180 mm below mid plane)

-M5PCCVN (5 pieces)

F82H+10BN: DX6, DX7
F82H+11BN: EX6, EX7
F82H TIG FG HAZ: 21V5

References

[1] A. L. Qualls, K. R. Thoms, D. W. Heatherly, and R. G. Sitterson, "Assembly of the MFE-RB-17J Experiment," Fusion Materials Semi-annual Progress Report DOE/ER/0313/35, (December 2003) 242.

[2] J. P. Robertson, K. E.Lenox, M. L. Grossbeck, A. F. Rowcliffe, S. Jitsukawa, and K. Shiba, Fusion Materials Semi-annual Progress Report DOE/ER/0313/23, (December 1997) 345.

[3] A. L. Qualls, Fusion Materials Semi-annual Progress Report DOE/ER/0313/28, (June 2000) 266.

[4] T. Hirose, H. Tanigawa, M. Ando, A. Kohyama, Y. Katoh and M. Narui, "SF-1 Radiation effects on low cycle fatigue properties of reduced activation ferritic/martensitic steels, " Journal of Nuclear Materials, 307-311 (2002) 304.

[5] K. Shiba, A. Hishinuma, A. Tohyama and K. Masamura, "Properties of Low Activation Ferritic Steel F82H IEA Heat -Interim Report of IEA Round-robin Tests (1)-," JAERI-Tech 97-038 (1997).

[6] T. Sawai, K. Shiba and A. Hishinuma, “Microstructure of welded and thermal-aged low activation steel F82H IEA heat,” Journal of Nuclear Materials, 283-287 (2000) 657.

[7] H. Tanigawa, T. Hirose, K. Shiba, R. Kasada, E.Wakai, H. Serizawa, Y. Kawahito, S. Jitsukawa, A. Kimura, Y. Kohno, A. Kohyama, S. Katayama, H. Mori, K. Nishimoto, R.L. Klueh, M.A. Sokolov, R.E. Stoller, S.J. Zinkle, " Technical issues of reduced activation ferritic/martensitic steels for fabrication of ITER test blanket modules," Fusion Engineering and Design 83 (2008) 1471.

[8] H. Ogiwara, H. Tanigawa, T. Hirose, M. Enoeda and M. Akiba, "Impact Properties of Reduced Activation Ferritic/Martensitic Steel, F82H Jointed by Hot Isostatic Pressing," to be published in Journal of Nuclear Materials.

[9] E. Wakai, M. Sato, T. Sawai, K. Shiba and S. Jitsukawa, “Mechanical properties and microstructure of F82H steel doped with boron or boron and nitrogen as a function of heat treatment,” Materials Transactions. Vol. 45, no. 2, (2004) 407.

[10] T. Sawai, K. Shiba and A. Hishinuma "Microstructure of welded and thermal-aged low activation steel, F82H IEA heat," Journal of Nuclear Materials, 283-287 (2000) 657.

[11] K. Shiba, M. Enoeda and S. Jitsukawa, "Reduced activation martensitic steels as a structural material for ITER test blanket," Journal of Nuclear Materials, 329-333 (2004) 243.

[12] B. van der Schaaf, D.S. Gelles, S. Jitsukawa, A. Kimura, R.L. Klueh, A. Möslang, G.R. Odette, "Progress and critical issues of reduced activation ferritic/martensitic steel development," Journal of Nuclear Materials 283-287 (2000) 52.

[13] P. Miao, G.R. Odette, T. Yamamoto, M. Alinger, D. Hoelzer and D. Gragg, "Effects of consolidation temperature, strength and microstructure on fracture toughness of nanostructure ferritic alloys," Journal of Nuclear Materials, 367–370 (2007) 208.

Summary of the USCB Advanced Test Reactor National Scientific Users Facility Irradiation Experiment – G. R. Odette, T. Yamamoto, B. Sams, D. Klingensmith N. Cunningham (Department of Mechanical Engineering, University of California Santa Barbara) G. Waches, J. I. Cole, P. E. Murrey (Idaho National Laboratory)

OBJECTIVES

The primary objective of this study is to create a large library of irradiated alloys, for a variety of specimen geometries, to address the scientific questions that include the following.

1. The effect of low dose (nominally 6 dpa peak) irradiations at 8 temperatures (nominally 288, 350, 400, 450, 500, 550, 650, and 750°C) on the basic microstructures and constitutive properties in disc multi-purpose coupons (DMC), cross comparing various alloys as well as examining model alloys.
2. The evolution of interface and bulk microstructure, microchemistry and micro-nanohardness in diffusion multiples (DM) specimens.
3. The effects on fracture toughness of radiation hardening at lower temperatures and microstructural and phase instabilities at higher temperatures for a subset materials and irradiation conditions.
4. The stability of the nanoscale Y-Ti-O features (NF) and nanostructured ferritic alloys (NFA) microstructures under high temperature irradiation.
5. Others mechanisms studies, including He transport and fate in-situ injection samples, including at high temperatures.

SUMMARY

We have designed and prepared a comprehensive Advanced Test Reactor (ATR) irradiation experiment as part of a successful ATR National Scientific Users Facility (NSUF) proposal entitled *Characterization of the Microstructures and Mechanical Properties of Advanced Structural Alloys for Radiation Service: A Comprehensive Library of ATR Irradiated Alloys and Specimen.* A total of about 1400 specimens were fabricated and loaded at UCSB in 33 packets. Each packet has a unique outer profile and insulator design to minimize axial variations set by the Ar-He gas mixture and gap dimension. The packets were assembled at UCSB and subsequently loaded into 11 approximately 11 mm diameter capsule tubes at the Idaho National Laboratory (INL) in July, 2009. The experimental objective is to develop an integrated hardening/softening database from 288 to 750 ºC on 44 steels and model alloys irradiated up to 6 dpa. The experiment will also characterize the irradiation embrittlement of 6 alloys and support the development of small specimen fracture test methods including for interface fracture. The specimens will also support extensive microstructural and mechanism studies, including helium injection and diffusion multiple experiments. The irradiated specimens will form a “lending library” and sustain a number of future collaborations. The irradiation will be initiated in August of 2009 and completed in April of 2010.

PROGRESS AND STATUS

Scientific Objectives

The products of the ATR experiment will include the following items:

a. An unprecedented database on irradiation hardening (and softening) between 288 and 750°C from about 1.5 to 6 dpa for 6 TMS, 10 NFA and 1 austenitic alloys. The irradiation hardening will be primarily characterized by microhardness measurements, supplemented by tensile tests on a subset of materials. This will provide a database for refined fits of semi-empirical hardening models that we have developed. Since many alloys will be irradiated side-by-side, the database will also provide a unique opportunity to develop models for the effects of metallurgical variables on irradiation hardening. Combinations of special microhardness techniques that we have developed will be combined with the other deformation dominated fracture tests for a subset of alloys, such as tensile and shear punch measurements, and used to develop micromechanical models of constitutive, flow instability and failure ductility properties of the

irradiated alloys over a wide range of temperatures. Irradiations of TMS alloys at higher temperatures will provide a database for examining microstructural instabilities that can lead to softening (as well as non-hardening embrittlement - see below). Such instabilities are manifested as coarsening of precipitates and subgrains, recovery of dislocation and lath structures and precipitation of brittle phases, generally on the grain boundaries. There is growing evidence that irradiation and thermal instabilities interact synergistically. Thus the ATR mechanical property and microstructural data will be combined with thermal aging studies to provide the first systematic investigation of irradiation-thermal instability synergisms at higher temperatures.

b. Fracture mechanics studies using compact tension (CT) specimens in the framework of the Master Curve Method will be carried out on a subset of alloys to measure shifts in the 100 MPa$\sqrt{m}$ reference temperatures, ΔT_o. These tests will be supplemented by mini bend bar tests on other alloys. The irradiation will be used to further develop a new wedge loading chevron notch specimen, primarily intended to characterize the strength and toughness of interfaces. These small specimen methods can be used to evaluate test specific transition temperature shifts ΔT that can be adjusted to ΔT_o using calibrated micromechanical models.

c. Microstructural characterization on the irradiation-conditioned materials studies using a large suite of state of the art tools (SANS, TEM, APT, PAS and various X-ray based techniques). We will seek to establish a large international network of university and laboratory collaborators to assist in these studies. This could be enabled, for example, by providing small FIBed specimens that minimize limitations normally imposed by handling highly radioactive materials. In this sense, the ATR experiment will provide a "lending library" of specimens that can be examined by a large number of scientists using a variety of techniques. In addition to carrying out some of these studies ourselves, UCSB's role would be to encourage and help coordinate the collaborative research, to pool the information into a useful database and to combine it with mechanical property data to develop advanced microstructurally-based physical models of the deformation and fracture of irradiated alloys.

d. Model alloys and systems of various sorts are also included in the experiment. For example, a series of simple model alloys will be included to assess the effects of 0 to 18% Cr in simple Fe-Cr binary alloys over a wide range of irradiation temperatures. The experiment will probe the effect of Cr on both defect accumulation and α' precipitation including the effects of radiation enhanced diffusion (RED) and possible irradiation-induced non-equilibrium modifications of α-α' phase boundaries. Other model materials include a set of pressure vessel steels, simple two to five constituent ferritic alloys, some maraging steels and model nanolayered metallic composites with engineered boundaries.

e. A very exciting and absolutely novel aspect of the ATR experiment will be the inclusion of so-called diffusion multiples (DM) that provide a "lab on a chip-combinatorial" type opportunity to characterize thermo-kinetic parameters of multiconstituent-multiphase alloys including mapping the phase diagrams and interdiffusion rates. DM are bonded assemblies of typically 3 elements, akin to more familiar and simpler binary diffusion couples. In the case of a diffusion couple made of primary elements, thermal aging provides information of equilibrium phase boundaries and interdiffusion rates along a binary tie line at a specified temperature. In the case of the diffusion multiple, this information is extended to ternary, quaternary and even higher order systems by creating corresponding multi-element inter-diffusion zones. These zones can be probed by a number of microstructural-microanalytical techniques as well as methods to probe physical and mechanical properties (e.g., using nanohardness). The large database produced by diffusion multiples will be analyzed to derive the thermodynamic and kinetic parameters used in computational materials codes like *Thermocalc* and *Dictra* and advanced models (e.g., phase field) of microstructural-microchemical evolutions. While the DM method is not new, it has never been applied to evaluation of alloy thermo-kinetics under irradiation, so the ATR irradiation present a unique new opportunity. Annealing diffusion multiple specimens will also help separate non-equilibrium effects of irradiation from radiation enhanced diffusion accelerated near equilibrium processes. Radiation enhanced diffusion will permit explorations of lower temperature thermodynamic regimes that are otherwise kinetically inaccessible due to slow thermal diffusion rates. Note that such databases are absolutely

essential for computational materials by design approaches to developing advanced high performance, radiation tolerant alloys.

f. In situ He generation experiments will also be carried out in the ATR irradiation. The thermal to fast neutron flux ratio is lower in ATR compared to HFIR and the peak dpa in the experiment is also lower. Thus the maximum He content in this case will be limited to about 150 appm. However this amount is sufficient to address issues of He transport and fate and will permit us to include newer and more advanced NFA than in the previous and ongoing HFIR irradiations over a wider range of temperatures. The ATR experiments will use thick Ni implantation foils to inject α-particles into wedge shaped specimens from both sides to producing uniform He concentrations up to a thicknesses of ≈ 8 μm. The use of wedge specimens will also facilitate PIE since their end will be partially pre-thinned to near electron transparency.

Test Matrix

The irradiation contains ≈ 1400 specimens of different types, composed of a wide variety of materials, which will provide a large body of microstructural and mechanical property data to address many key irradiation service questions. The irradiations will be carried out in the A10 position at ATR up to a maximum dose of ≈ 6 dpa. The specimens are loaded into 11 capsules, 10 out of which are irradiated at a time, to obtain the temperatures and doses specified in Table 1 for each of the experimental capsules. Baseline irradiation temperatures are 288, 550 and 750°C; smaller capsules will also be irradiated at 350, 400, 450 and 500°C.

Most specimens are simple DMC (0.2 mm thick and ≈ 10 mm in diameter) of more than 60 materials that are to be used for microstructural studies (TEM, SANS,…), measuring constitutive properties by advanced hardness techniques, shear punch tests (also making TEM discs), post irradiation annealing studies and disc bend (DB) fracture tests. The tentative alloy matrix consists of 6 tempered martensitic steels (TMS), 10 NFAs, 1 stainless steel (SS) and 28 model alloys (MA), 3 DM. Selected alloys are included in the form of sub-sized SS-J tensile specimens, disc tensile specimen (DTS), disc compact tension (DCT) fracture specimens, and deformation and fracture mini-beams (DFMB). The DM specimens, made of 3 joined elements (or different alloys), are used to study *radiation modified* inter-diffusion and phase formation processes, encompassing the entire phase diagram at the specified temperature. An advanced sub-sized dual chevron notched cantilevered beam specimen that is under development to provide higher constraint than standard fracture specimens of corresponding sizes, is included as well.

More detailed description and purposes of the materials and specimen types as well as irradiation conditions are give in the later sections.

Materials of interest

In this study, six different classes of alloys and processing conditions are being investigated as summarized in Table 2 along with nominal compositions of the alloys. The study will focus on Fe-based alloys being considered for next generation reactor applications as both cladding and structural materials, and range from simple model alloys to complex commercially fabricated alloys. The following sections will highlight briefly the significance of each of these classes of samples.

Table 1 UCSB ATR Experiment Capsule Summary

Capsule ID	Materials	Target Temp.	Nominal Target Dose
UCSB-1	Mostly Fe-Based Metals	288 ºC	1.7 dpa
UCSB-2		550 - 750 ºC	2.3 to 4.2 dpa
UCSB-3		350 - 550 ºC	4.5 – 5.2 dpa
UCSB-4		650 - 750 ºC	5.6 – 5.9 dpa
UCSB-5		350 - 500 ºC	6.1 – 6.2 dpa
UCSB-6A*		288 ºC	1.7 dpa
UCSB-6B*		288 ºC	4.6 dpa
UCSB-7		288 ºC	6.0 – 6.1 dpa
UCSB-8		288 ºC	5.5 dpa
UCSB-9		288 ºC	4.0 – 5.0 dpa
UCSB-10		350 – 500 ºC	2.3 – 3.5 dpa

* 6A runs for the first cycle only and is replaced with 6B that runs through the end of the project.

Tempered Martensitic Steels (TMS): These alloys, frequently referred to as ferritic-martensitic steels (F-M), include T91, HT9, NF616, F82H-IEA, F82H mod.3, and Eurofer 97. All but HT9 (≈12wt% Cr) have Cr content on the order of 8 to 9 wt%, and undergo a martensitic transformation following a austenitizing-normalizing tempering thermal treatments result a high strength and toughness. HT9 is the current primary cladding and duct candidate for liquid metal cooled burner reactors.. T91 and NF616 are two F-M alloys currently in use in fossil and other non-nuclear industries, and F82H and Eurofer 97 are alloys developed for fusion applications that have reduced long-term radioactivity permitting a more economical shallow surface burial waste disposal path. All of the alloys have BCC crystal structures generally manifest low swelling rate. Radiation induced shift of the ductile-to-brittle transition temperature (DBTT) is a major issue in using these F-M alloys in a irradiation environment and understanding embrittlement will be substantial focus of these studies.

Nanostructured Ferritic Alloys (NFA): The second set of materials are a series of primarily developmental alloys, all of which are Fe-based, that contain high densities of nanometer-scale dispersion strengthening features (NF). NFA have outstanding high temperature creep strength compared to conventional F-M alloys. There is considerable evidence that NFA are very radiation tolerant because NF act as sinks for radiation produced point defects and trap He in fins-scale harmless bubbles.

Stainless Steels (SS): One cast austenitic stainless steel alloy was included in the experiment.

Model Alloys (MA): Simple model alloys were included for fundamental and developmental. These alloys range from pure iron to binary and ternary alloys, to complex model reactor pressure vessel steels. Information from these studies will help verification and validation of computer models being developed to predict irradiation effects in more complex systems.

Diffusion Multiples (DM): DM were included to permit the study thermo-kinetics in multi-element systems under irradiation over a range of temperature. They consisted of up to three diffusion bonded elements or alloys to promote subsequent interdiffusion and phase formation. The triple junction is a DM, while interfaces bonds represent diffusion couples (DC). Note Table 2a lists the primary DM combinations. However, W top and bottom caps were used in all cases, that also resulted in other DM and DC regions.

Table 2a Nominal Chemistry of Target Materials

Material Category	Material ID	Cr	W	Mo	Ni	C	Ti	Y	V	Si	Fe	Other
Tempered Martensitic Steels (TMS)	T91	8.4	-	0.5	-	0.1	-	-	-	-	bal.	
	HT-9	12.0	0.5	0.9	0.5	0.2	-	-	0.3	0.2	bal.	
	NF616	8.8	1.9	0.5	0.2	0.1	-	-	0.2	0.2	bal.	
	F82H IEA	7.7	2.0	-	-	0.1	-	-	0.2	0.2	bal.	
	F82H mod.3	7.7	2.0	-	-	0.1	-	-	0.2	0.2	bal.	
	Eurofer 97	9.0	1.1	-	-	0.1	-	-	0.2	0.2	bal.	
Nano-structured Ferritic Alloys (NFA)	MA956	20	-	-	-	0.04	0.4	0.5	-	-	bal.	Al 4.5
	MA957	14	-	0.3	0.1	0.1	1.0	0.25	-	-	bal.	Al 0.1
	PM2000	20	-	-	-	0.1	0.5	0.5	-	-	bal.	Al 5.5
	14CrYWT-1150	14	3	-	-	-	0.4	0.25	-	-	bal.	
	14CrYWT-1000	14	3	-	-	-	0.4	0.25	-	-	bal.	
	9Cr-2WYT	9.2	2.0	-	-	0.03	0.3	0.3	-	0.04	bal.	
	16Cr-2WYT	16	1.8	-	-	0.03	0.3	0.3	-	0.04	bal.	Al 4.6
	14CrYWT(H-milled)	13	1.0	-	-	-	0.3	0.3	-	-	bal.	
	14CrYWT(Ar-milled)	13	1.0	-	-	-	0.3	0.3	-	-	bal.	
	14CrYWT ORNL	14	3	-	-	-	0.4	0.25	-	-	bal.	
Stainless Steels (SS)	Cast SS	17	13	2.5							bal.	Mn 3; N 0.3
Diffusion Multiple (DM)	Fe-Cr/W/Ti	10	10	-	-	-	10	10	-	-	bal.	
	Fe-Cr/W/Ni	10	10	10	-	-	-	-	-	-	bal.	
	Fe/Cu/Ni/W	14	-	-	21	-	-	-	-	10	bal.	

Table 2b Nominal Chemistry of Target Materials (Model alloys)

Material ID	Cr	W	Mo	Cu	Mn	Ni	C	P	Nb	V	Si	Fe	Other
JRQ	0.12	-	0.50	0.14	1.4	0.82	0.1	0.01	-	-	0.2	bal.	
LA	-	-	0.55	0.40	1.3	0.00	0.1	0.00	-	-	0.2	bal.	
LB	-	-	0.55	0.40	1.3	0.18	0.1	0.00	-	-	0.2	bal.	
LC	-	-	0.55	0.41	1.4	0.86	0.1	0.00	-	-	0.2	bal.	
LD	-	-	0.55	0.38	1.3	1.25	0.1	0.00	-	-	0.2	bal.	
LG	-	-	0.55	0.00	1.3	0.74	0.1	0.00	-	-	0.2	bal.	
LH	-	-	0.55	0.11	1.3	0.74	0.1	0.00	-	-	0.2	bal.	
LI	-	-	0.55	0.20	1.3	0.74	0.1	0.00	-	-	0.2	bal.	
OV1	-	-	-	-	1.6	-	-	-	-	-		bal.	
OV2	-	-	-	-	1.6	0.80	-	-	-	-		bal.	
OV3	-	-	-	-	1.6	1.60	-	-	-	-		bal.	
OV4	0.05	-	-	-	1.6	0.80	-	-	-	-		bal.	
OV5	0.05	-	-	-	1.6	1.60	-	-	-	-		bal.	
OV6	0.10	-	-	-	1.6	0.80	-	-	-	-		bal.	
OV7	0.10	-	-	-	1.6	1.60	-	-	-	-		bal.	
CM6	-	-	0.54	0.02	1.5	1.68	0.1	0.00	-	0.1		bal.	
F82H-1.4Ni	7.7	2.	-	-	-	1.4	0.1	-	-	0.2	0.2	bal.	
Fe-3Cr	3.0	-	-	-	-	-	-	-	-	-	-	bal.	
Fe-6Cr	6.0	-	-	-	-	-	-	-	-	-	-	bal.	
Fe-9Cr	9.0	-	-	-	-	-	-	-	-	-	-	bal.	
Fe-12Cr	12.0	-	-	-	-	-	-	-	-	-	-	bal.	
Fe-15Cr	15.0	-	-	-	-	-	-	-	-	-	-	bal.	
Fe-18Cr	18.0	-	-	-	-	-	-	-	-	-	-	bal.	
SiC	-	-	-	-	-	-	30	-	-	-	70	-	
Maraging	12		1.4		0.3	9.2		0.03			0.3	bal.	Al 1.6
Ni/CuNb-1				1.0		bal.			1.0				
Ni/CuNb-2				2.0		bal.			2.0				
Ni/CuNb-3				3.0		bal.			3.0				

Specimen Types and Designs

Nine unique geometries were included in the irradiation experiment, including:

- Disc multi-purpose coupons (DMC) that constitute the majority of the specimens. The DMC are nominally 8 mm (5/16 in) in diameter with both nominally 0.25 mm and 0.50 mm thickness dimensions. Smaller samples will be punched from the discs following irradiation.

- Diffusion Multiple (DM) 8 mm diameter discs with thickness dimensions from 2.25 to 2.75 mm as shown in Figure 1a.

- He implanter discs are DMC with a sharp ground and polished wedge over part of their circumference, producing a significant area thinner than 9 μm. The discs with wedges are placed between Ni foils as schematically illustrated in Figure 1b. He generated as α-particles in Ni overlay foils under neutron irradiation are uniformly injected in the thin area.

- Subsize tensile specimens (SS-J2) shown in Figure 2a are 4 mm wide x 16 mm long and 0.5 mm thick. The gauge length is 5 mm. Special deformation tensile specimens with center-hole or dual offset gauge section notches shown in Figures 2b and 2c were also included.

- Disc compact tension (DCT) specimens shown in Figure 3, that will be used for fracture toughness testing, are 10 mm in diameter and 3.7 mm thick.

- Deformation and fracture mini-beam (DFMB) (not shown), that will also be used for studying fracture behaviour, are 1.67 mm square and 9.2 mm long and are pre-cracked to a crack length to width ratio of about 0.4.

- The chevron notch wedge (chevron) specimen, shown in Figure 4, are 5 mm high, 4 mm wide and 8 mm long. They will be used to investigate the effects of crack front lengths and constraint on fracture monolithic toughness in this experiment.

- Cylindrical compression (CC) specimens have a 2.0 mm diameter and 2.4 mm height.

The majority of the specimens are DMC.

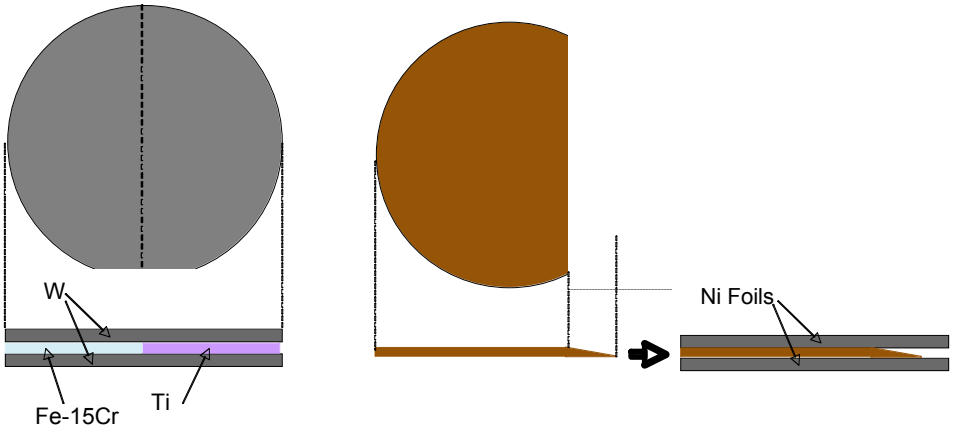

Figure 1 Schematic drawings of: (a) diffusion multiple; and (b) He implanter discs.

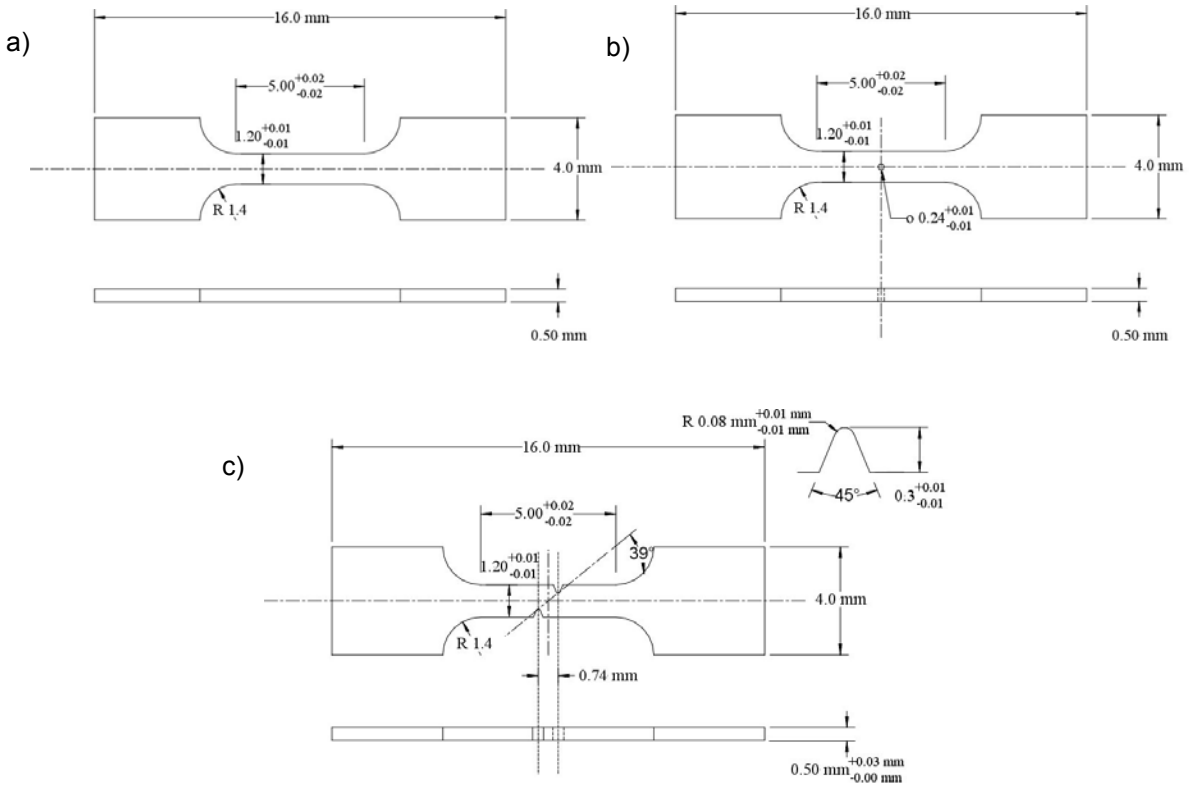

Figure 2 Drawings of three types of SSJ2 tensile coupon dog-bone specimens: a) plain, b) center-holed, and c) dual offset notched.

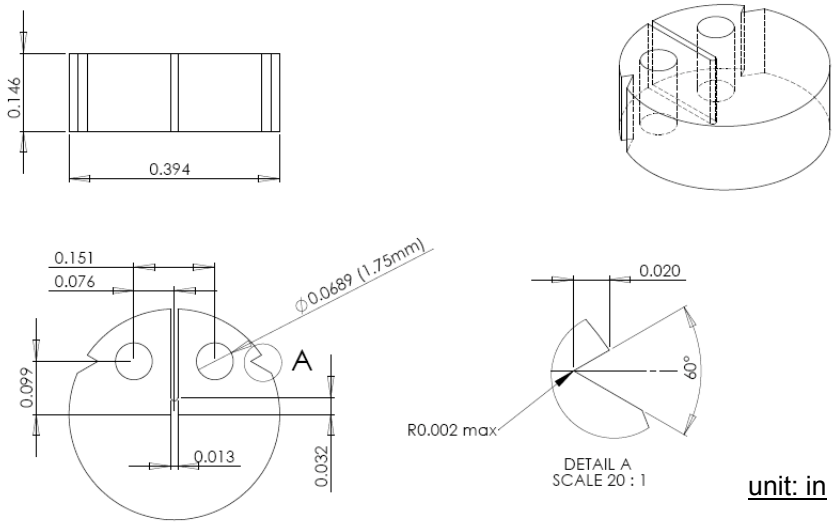

Figure 3 Drawing of the DCT specimen.

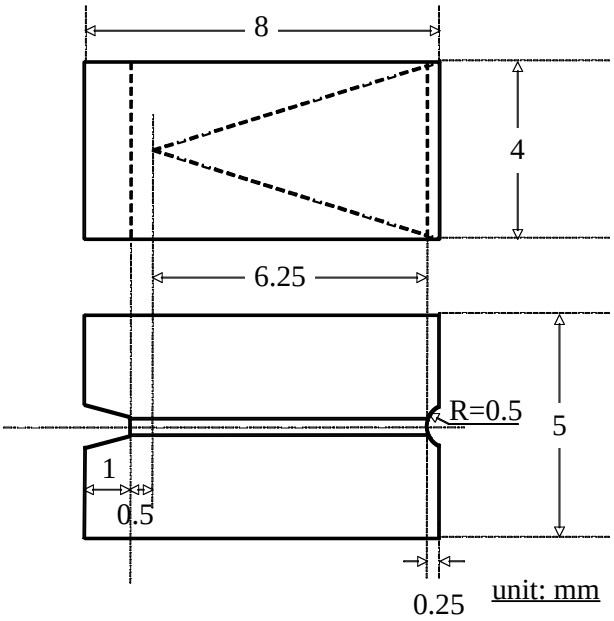

Figure 4 Schematics of a chevron notched wedge specimen.

Irradiation Conditions

Specimens were grouped into a total of 33 packets that were exposed at a target temperature over a narrow range of neutron fluence. Each packet was designed to minimize the axial temperature variations. An example of packet is shown in Figure 5a for the DMC specimens. The design features: 1) a “pill box” tube that contains a press-fit stack of DMC specimens; 2) a profiled outer shape to minimize temperature variations near the target temperature established by a precise gap and He-Ar gas mixture; 3) thick end plugs with thin stand-off pins that minimize axial heat flow. The packet and gap design was optimized by iterative finite element analysis (COMSL). Figure 5b illustrates the placement of a packet in a capsule; and Figure 5c shows an example of an optimized temperature distribution (± 6.5 ºC) for a 288ºC packet. Packets at each nominal temperature were placed in various positions inside the capsules and the capsule stack-ups so that they normally receive 3 (in 3 cases 2) peak peak fluences. Figure 6a shows the overall packet stack-up as a function of the power factor (PF). Figure 6b shows the corresponding flux versus fluence for the packets at each nominal irradiation temperature. The difference between the predicted and nominal temperatures for all the packets, ranging from 5 to 10 ºC, is shown in Figure 7. As shown in Table 1 and Figure 6b, capsule 6A is replaced by 6B after the first of four cycles. Capsule 6a receives 1.7 dpa at the near peak flux. Capsule 1, in the low flux region, receives the same dpa in 4 cycles, providing a basis to assess any dose rate effects over this flux range. Table 3 summarizes just types and the numbers of specimens for the irradiation conditions.

Irradiation schedule and post-irradiation examination (PIE)

The ATR irradiation will begin in August 2009 and will be completed in April 2010. The PIE will primarily be carried out in hot cell facilities of our national laboratory collaborator team. UCSB will lead the planning and execution of the PIE and subsequent analysis and evaluation of the resulting database. More detailed spreadsheet describing the materials, types and numbers of specimens and corresponding irradiation conditions, as well as a complete loading list, are available upon request.

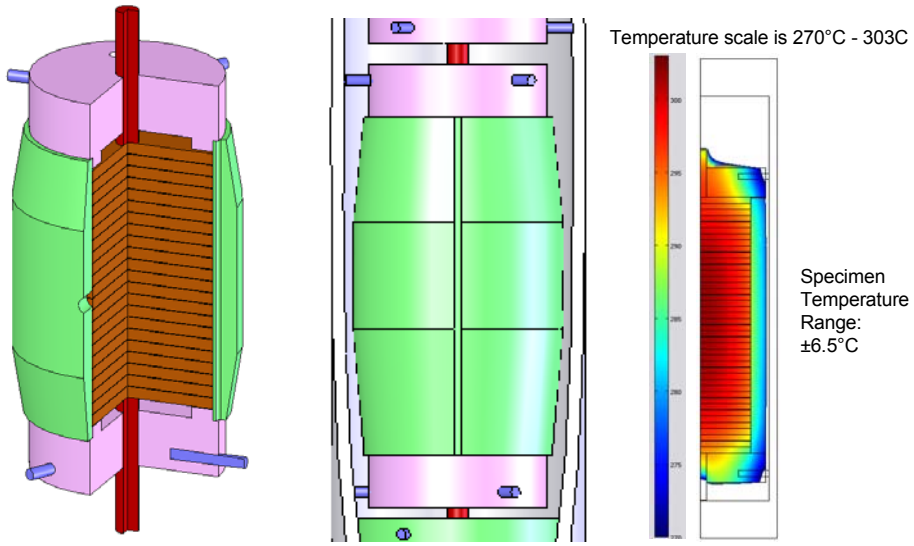

Figure 5 Illustration of (a) innovative “pill-box”-type packet to hold DMC (disc multipurpose coupon) specimens, (b) a special profiled “pill-box” shape to control gas gap heat conduction, and (c) the uniform thermal profile estimated for a 300 ºC capsule at high flux.

Table 3 Specimen types and numbers for the specified irradiation conditions

Temperature (ºC)	Irr. Code	dpa	DMC-thin	DMC-thick	He-Imp	DM	B&C	SSJ	DTS	DCT	DFMB	CHW	Total
288	H	5.6	36	113	-	3	-	36	9	25	48	6	276
	M	4.2	-	49	-	-	-	18	-	-	-	-	67
	M@high-f	4.6	-	-	-	-	-	-	-	8	-	-	8
	L	1.7	10	38	-	-	-	-	-	-	-	-	48
	L@high-f	4.6	8	53	-	-	-	-	-	-	-	-	61
350	H	6.1	22	52	-	-	-	-	-	-	-	-	74
	M	4.5	-	21	-	-	-	-	-	-	-	-	21
	L	3.5	10	36	-	-	-	-	-	-	-	-	46
400	H	6.2	18	52	14	-	-	-	-	-	-	-	84
	L	3.1	6	38	-	-	-	-	-	-	-	-	44
	L												0
450	H	6.2	20	46	-	-	-	-	-	-	-	-	66
	L	2.7	10	26	-	-	-	-	-	-	-	-	36
	L												0
500	H	6.2	9	52	14	-	-	-	-	-	-	-	75
	L	2.3	10	24	-	-	-	-	-	-	-	-	34
	L												0
550	H	4.9	29	63	12	3	-	18	-	-	16	-	141
	M	4.0	-	27	-	-	-	18	-	-	-	-	45
	L	3.0	10	26	-	-	-	-	-	-	-	-	36
650	H	5.6	5	45	12	3	-	18	-	-	-	-	83
	M	3.3	4	15	-	-	-	-	-	-	-	-	19
	L	2.4	4	17	-	-	-	-	-	-	-	-	21
750	H	5.9	13	40	12	3	-	-	-	-	-	-	68
	M	3.6	2	16	-	-	-	-	-	-	-	-	18
	L	2.7	2	17	-	-	-	-	-	-	-	-	19
Total			228	866	64	12	0	108	9	33	64	6	1390

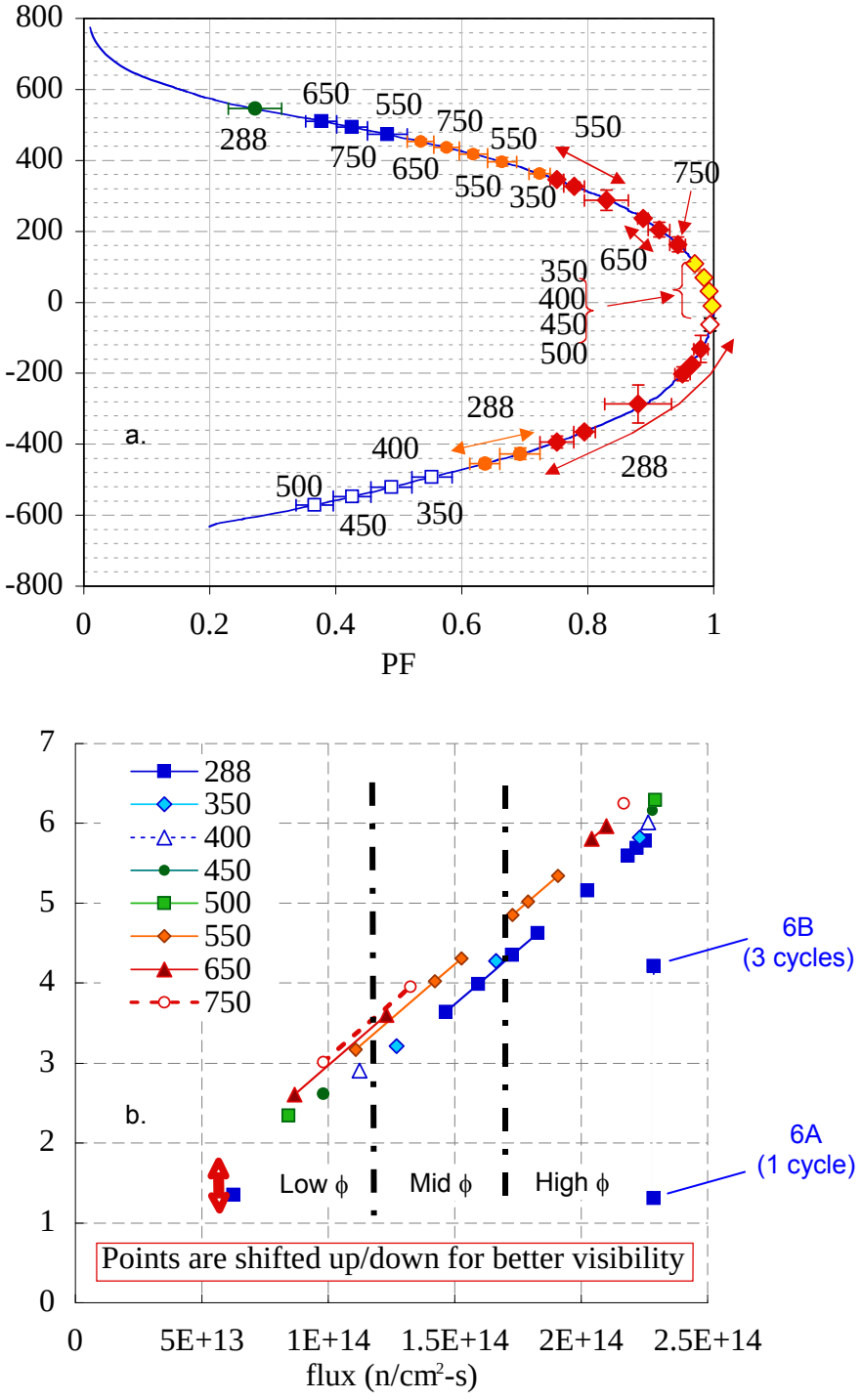

Figure 6 (a) Packet temperature assignment and power factors (PF) as a function of the packet location, (b) fluence – flux estimation of packets.

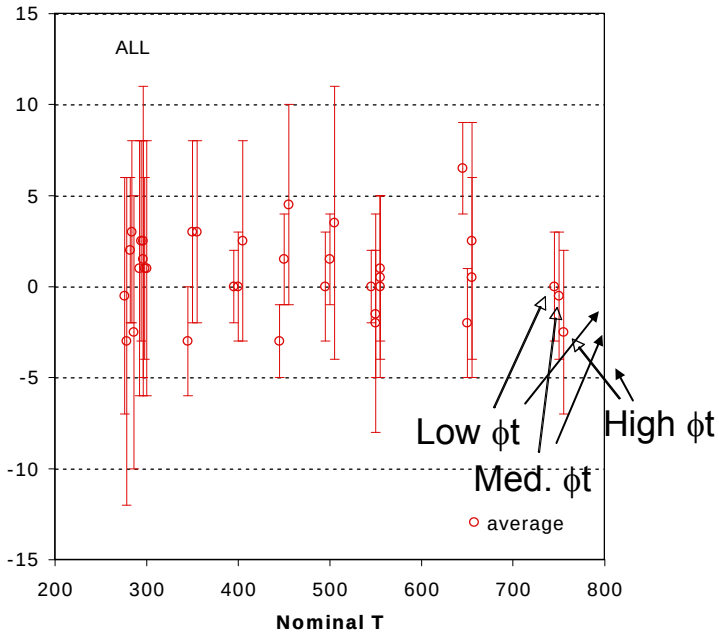

Nominal T (ºC)

Figure 7 Average and the range of difference between predicted and nominal temperatures for all the packets.

Acknowledgement

The authors are grateful to ATR NSUF program for all the technical support in designing and fabricating specimens and capsule parts. This research was also supported, in part, by the U. S. Department of Energy, Office of Fusion Energy Sciences, under contract DE-FG03-94ER54275, and by the U. S. Department of Energy, Office of Nuclear Energy, under contracts DE-FC07-05ID14663 and DE-FC07-07ID14825.